Fakultät für Physik der Technischen Universität München
Physik Department E12

Neutron Transfer Reactions in the fp-shell Region

Mahmoud Mahgoub

Vollständiger Abdruck der von der Fakultät für Physik der
Technischen Universität München zur Erlangung des akademischen Grades eines

Doktors der Naturwissenschaften (Dr. rer. nat.)

genehmigten Dissertation.

Vorsitzender: Univ.-Prof. Dr. M. Ratz

Prüfer der Dissertation:

1. Univ.-Prof. Dr. R. Krücken
2. Univ.-Prof. Dr. F. von Feilitzsch

Die Dissertation wurde am 27.05.2008 bei der Technischen Universität München
eingereicht und durch die Fakultät für Physik am 26.06.2008 angenommen.

Abstract

Neutron transfer reactions were used to study the stability of the magic number N = 28 near ^{56}Ni. On one hand the one-neutron pickup (d,p) reaction was used for precision spectroscopy of single-particle levels in ^{55}Fe. On the other hand we investigated the two-neutron transfer mechanism into ^{56}Ni using the pickup reaction $^{58}\mathrm{Ni}(\vec{\mathrm{p}},\mathrm{t})^{56}\mathrm{Ni}$. In addition the reliability of inverse kinematics reactions at low energy to study exotic nuclei was tested by the neutron transfer reactions $\mathrm{t}(^{40}\mathrm{Ar},\mathrm{p})^{42}\mathrm{Ar}$ and $\mathrm{d}(^{54}\mathrm{Fe},\mathrm{p})^{55}\mathrm{Fe}$ using tritium and deuterium targets, respectively, and by comparing the results with those of the normal kinematics reactions.

The experimental data, differential cross-section and analyzing powers, are compared to DWBA and coupled channel calculations utilizing the code CHUCK3. By performing the single-neutron stripping reaction $(\vec{\mathrm{d}},\mathrm{p})$ on ^{54}Fe the $1f_{7/2}$ shell in the ground state configuration was found to be partly broken. The instability of the $1f_{7/2}$ shell and the magic number N = 28 was confirmed once by observing a number of levels with $J^{\pi} = 7/2^{-}$ at low excitation energies, which should not be populated if ^{54}Fe has a closed $1f_{7/2}$ shell, and also by comparing our high precision experimental data with a large scale shell model calculation using the ANTOINE code [5]. Calculations including a partly broken $1f_{7/2}$ shell show better agreement with the experiment. The instability of the $1f_{7/2}$ shell was confirmed also by performing the two-neutron pick-up reaction $(\vec{\mathrm{p}},\mathrm{t})$ on ^{58}Ni to study ^{56}Ni, where a considerable improvement in the DWBA calculation was observed after considering $1f_{7/2}$ as a broken shell.

To prove the reliability of inverse kinematics transfer reactions at low energies (~ 2 AMeV), the aforementioned single-neutron transfer reaction (d,p) was repeated using a beam of ^{54}Fe ions and a deuteron target. From this inverse kinematics experiment we were able to reproduce the absolute cross-section and angular distributions for a number of ^{55}Fe levels, using spectroscopic factors similar to those obtained in normal kinematics. Also in the inverse kinematics two-neutron transfer reaction $\mathrm{t}(^{40}\mathrm{Ar},\mathrm{p})^{42}\mathrm{Ar}$, it was possible to reproduce the angular distribution and to deduce the transferred angular momentum for levels in ^{42}Ar.

The results are used to discuss possibilities and limitations for future inverse kinematics transfer reactions using beams of short-lived radioactive nuclei.

Zusammenfassung

Neutron Transfer Reaktionen wurden eingesetzt zur Untersuchung der Stabilität der magischen Zahl $\mathrm{N} = 28$ in der Nähe von ^{56}Ni. Auf der einen Seite wurde die Ein-Neutron Pickupreaktion (d,p) für Präzisionsspektroskopie von Ein-Teilchen Zuständen in ^{55}Fe verwendet. Die Instabilität der $1f_{7/2}$ Schale und der magischen Zahl $\mathrm{N} = 28$ wurde bestätigt. Auf der anderen Seite wurde der Zwei-Neutronen Transfermechanismus zum ^{56}Ni mit der Pickupreaktion $^{58}\mathrm{Ni}(\vec{\mathrm{p}},\mathrm{t})^{56}\mathrm{Ni}$ untersucht.

Zum Nachweis der Anwendbarkeit von Transferreaktionen in inverser Kinematik für zukünftige Experimente mit radioaktiven Strahlen, wurde die Reaktion (d,p) wiederholt mit einem Strahl von ^{54}Fe Ionen und einem Deuteron Target. Ebenso wurde die Zwei-Neutronen Transferreaktion $\mathrm{t}(^{40}\mathrm{Ar},\mathrm{p})^{42}\mathrm{Ar}$ untersucht. Es war möglich, die gemessenen Winkelverteilungen mit DWBA Rechnungen zu reproduzieren und den übertragenen Drehimpuls bei der Population von Zuständen in ^{55}Fe und ^{42}Ar zu ermitteln.

Contents

Chapter 1

Introduction

Magic numbers and shell closures are the cornerstone for our nuclear structure knowledge. The stability of known shell closures as well as the modification of shell structure in nuclei far away from stability are at the center of modern nuclear structure research.

For example in the *fp*-shell region, ${}^{40}_{20}\mathrm{Ca}_{20}$ and ${}^{48}_{20}\mathrm{Ca}_{28}$ are good doubly magic nuclei due to the well known shell closures at Z = 20 and N = 20, 28. However, the shell closures are not always as simple as one may think. For example, the nucleus ${}^{56}_{28}\mathrm{Ni}_{28}$ should also be doubly magic (Z = N = 28). It is supposed to have a closed $f_{7/2}$ shell for both neutrons and protons. The top part of Figure 1.1 shows energies of the first 2^+ states for Ca and Ni isotopes. One observes that the $\mathrm{E}(2^+_1)$ in ^{56}Ni is much lower than the $\mathrm{E}(2^+_1)$ in ^{40,48}Ca. In the bottom figure, showing the reduced electric quadrupole transition rate $B(\mathrm{E2}: 0^+_1 \rightarrow 2^+_1)$ from the ground state 0^+ to 2^+_1 state, the B(E2) for ^{56}Ni is much higher than those for ^{40,48}Ca. Energy and B(E2) value clearly indicate that the magic shell is at least partly broken. On the theoretical side, recent large scale shell model calculations with a new residual interaction (GXPF1) by M. Honma & T. Otsuka *et al.* [17] show that the ^{56}Ni core is rather soft compared to the ^{40,48}Ca cores. According to the calculations the closed $(f_{7/2})^{16}$ shell configuration accounts for only 60% of the ^{56}Ni ground state wave function, while for ^{40,48}Ca the doubly magic configuration makes up 95% of their respective ground state, Figure 1.2. In this work an experimental test of the shell stability in the *fp*-shell region is presented. In particular, a high resolution study of the reaction ${}^{54}\mathrm{Fe}(\vec{\mathrm{d}},\mathrm{p})^{55}\mathrm{Fe}$ at the Garching Q3D spectrograph was performed to test the stability of the N = 28 shell closure just below ^{56}Ni. Results of this experiment are presented in Chapter 3.

In order to study single-particle structure in nuclei far away from stability, which are only available as radioactive ion beams, it is essential to test the reliability of the results of such reactions in inverse kinematics to results obtained in normal kinematics using stable beams and targets. Therefore, we have performed the reaction $\mathrm{d}({}^{54}\mathrm{Fe},\mathrm{p})^{55}\mathrm{Fe}$ in inverse kinematics and compared the results to those obtained for the normal kinematics.

In addition the ^{56}Ni shell closure was tested by means of the reaction ${}^{58}\mathrm{Ni}(\vec{\mathrm{p}},\mathrm{t})^{56}\mathrm{Ni}$ through the comparison of the relative strength of simultaneous and sequential two-neutron transfer, which is sensitive to two-particle two-hole excitations of the ^{56}Ni core as well as pairing correlations. This study is presented in Chapter 4.

As a pioneering study, we report in Chapter 4 also on results of the two-neutron

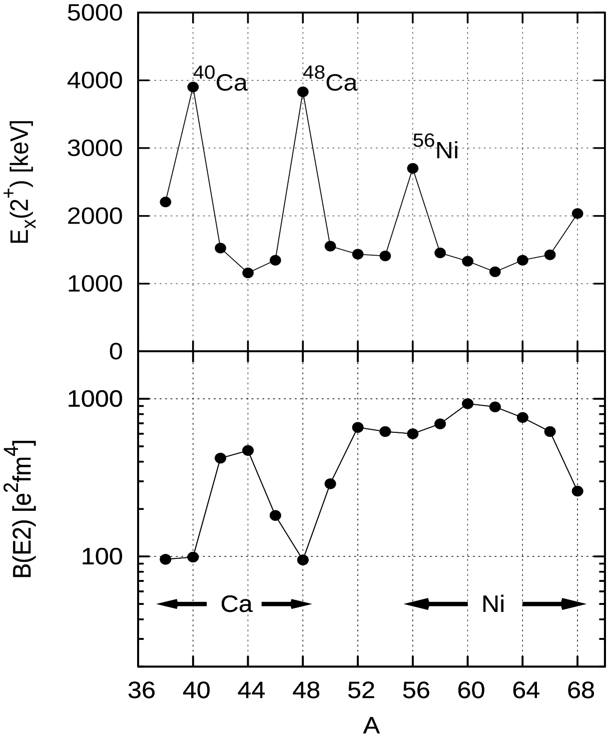

Figure 1.1.: Experimental energies (top) and the B(E2) -values for the $0^+ \rightarrow 2^+$ transitions (bottom) for the first 2^+ in Ca, Ti, Cr, Fe and Ni isotopes. The solid lines are to guide the eye only.

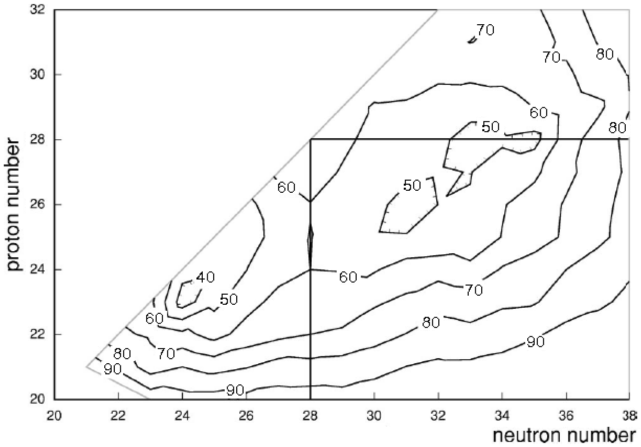

Figure 1.2.: The probability of closed-shell configurations in the calculated ground state wave functions around ^{56}Ni with the new residual interaction (GXPF1) by M. Honma & T. Otsuka *et al.* [17]. The ^{56}Ni core is rather soft compared to the ^{40,48}Ca cores. According to the calculations, the probability of the $(f_{7/2})^{16}$ configuration in the ground state wave function accounts for only 60% in ^{56}Ni in comparsion to around 95% in ^{40,48}Ca. From M. Honma & T. Otsuka *et al.* [17].

transfer inverse kinematic reaction $t(^{40}Ar, p)^{42}Ar$ using a tritium target, which is a prototype for future two-neutron transfer studies using radioactive beams, e.g. at REX-ISOLDE, CERN.

It should be mentioned that previous studies of the reaction $^{54}Fe(d, p)^{55}Fe$ was performed before by T. Taylor and J. A. Cameron [41], and for the reaction $^{58}Ni(\vec{p}, t)^{56}Ni$ J. H. Polane *et al.* [34]. However, in this thesis ^{54}Fe and ^{56}Ni nuclei were tested using more precise and higher resolution tools which were able to detect more levels and to deduce their spectroscopic factors.

1.1. Types of Reactions

1.1.1. Elastic Scattering

Elastic scattering does not produce intrinsic excitation. It is a collision in which the colliding particles only change their direction of motion and maybe the spin orientation. The projectile and the target remain in their ground state after the collision, therefore the Q- value for the reaction is zero. An example of the elastic scattering is

$$^{16}O + n \rightarrow {}^{16}O + n$$

1.1.2. Inelastic scattering

In inelastic scattering both the projectile and the target keep their identities but one or both will be excited to a higher energy, where a part of the kinetic energy of the relative motion goes into this excitation. An example for such scattering is

$$^{16}O + n \rightarrow {}^{16}O^{*} + n$$

1.1.3. Compound Nucleus Reactions

In this reaction the incident particle incorporates and loses (distributes) all its energy to all the target nucleons forming a new excited nucleus, called the compound nucleus, which has excitation energy equal to the kinetic energy of the incident particle plus the binding energy the incident particle has in the new excited nucleus.

The formation stage is fast and takes a period of time $\sim 10^{-21}$ s, which is approximately equal to the time the particle needs to travel across the diameter of the target nucleus. The compound nucleus can live a relatively longer time (from $10^{-19} - 10^{-15}$ s) enough time to forget the way in which it was formed, then it starts to disintegrate, regardless of the primary stage of the reaction, usually into an ejected small particle and a product nucleus or more particles or fission. The mechanisms of the formation of the compound nucleus depends on the collision energy, angular momentum, parity of the quantum state of the compound nucleus and regards the conversation lows. As the formation depends on the collision energy, certain reactions can only happen within a certain energy range. A good example for the compound reaction is

$$\begin{tikzcd}
\mathrm{p} + {}^{63}\mathrm{Cu} \arrow[dr] & & {}^{63}\mathrm{Zn} + \mathrm{n} \\
& {}^{64}\mathrm{Zn}^{*} \arrow[ur] \arrow[r] \arrow[dr] & {}^{62}\mathrm{Cu} + \mathrm{n} + \mathrm{p} \\
\alpha + {}^{60}\mathrm{Ni} \arrow[ur] & & {}^{62}\mathrm{Zn} + 2\mathrm{n}
\end{tikzcd}$$

1.1.4. Direct Reactions

Direct reactions become more probable as the projectile energy increases. Since the associated wavelength of the projectile decreases ($\lambda = h/P$). Direct reactions happen during a time of order of 10^{-22} s, if the formation evaporation decay is considered compound reactions could be six order of magnitude slower. There are two characteristic types of direct reactions. In the first type, through inelastic scattering a part of the transferred energy is used to excite a collective mode of the nucleus populating rotational and vibrational modes. In the second type, which is important for this work, a modification of the incident particle and of the nucleus contents occurs. Transfer reactions, such as pick-up reactions, where the projectile captures a nucleon from the target and, stripping reactions, where the projectile loses a nucleon in the target nucleus, are examples of that.

Direct reactions allow us to extract information about the reaction mechanism by employing simple models. For example, in the widely used stripping reaction (d,n) the angular distribution of the out going neutron presents a forward prominent peak and smaller peaks at larger angels.

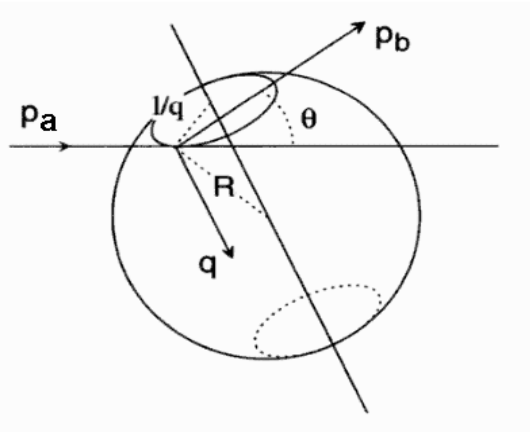

Figure 1.3.: Representation of a direct reaction (d,n), where a deuteron with momentum P_a hits a nucleus , transferring a proton with momentum q and releasing a neutron with momentum P_b. From Introduction to Nuclear Reactions By C. A. Bertulani and P. Danielewicz [3].

To understand this behavior, let us take the representation in Figure 1.3 from ref: [3]. A deuteron with momentum P_a hits the surface of the nucleus, where the deuteron loses a proton to the interior of the nucleus and the residual neutron leaves the nucleus with momentum P_b under angle θ with respect to the incident direction. The transferred proton is incorporated into the nucleus with momentum q, transferring to it an angular momentum $l = R \times q$ and populating a certain energy level of the product nucleus by transfer of specific l units of angular momentum. The energy of the emitted neutron and the vector q are determined for a given observation angle θ. This reduces the region of the nuclear surface where the reaction happened to a circle of radius l/q, Figure 1.3. The fact that the radii of the circles cannot be larger than the radius of the nucleus imposes a minimum value for θ, which increases as l increases. Under this approach, the particles leave the nucleus with considerable momentum at forward angles and one expects a decrease in the cross-section as the angles increase. With this restriction on the angular distribution the valid region for the observation of the neutron is located above the limiting angle θ_l. The value of θ_l can be calculated from the conservation of linear momentum

$$q^2 = P_a^2 + P_b^2 - 2P_aP_b\cos\theta, \tag{1.1}$$

where P_a and P_b are obtained from the initial and final energy of the particles. Finally, we should expect the angular distribution to be a function with maxima and minima, resulting from the interference between events that happen in the upper and lower circles represented in Figure 1.3.

Figure 1.4 shows the experimental cross-section angular distribution for the reaction $^{58}\mathrm{Ni}(\vec{\mathrm{p}},\mathrm{t})^{56}\mathrm{Ni}$ compared to theoretical calculation. We see that the behavior of the cross-sections agree with the theoretical predictions, and that θ_l for the first peak increases with l. As we will see later one can identify the transferred momentum value from the value of θ_l.

1.2. Stripping and Pick-up Reactions as a probe of the shell model

Neutron transfer reactions, like the stripping (d,p) and the pick-up reactions (p,d), are good examples for direct reactions. The importance of such reactions result from the ability to use them for the study of low-lying single-particle states. Such state can be selected from the energy of the outgoing particle. The transferred value of l and the parity of the states can be deduced directly from the angular distribution, Figure 1.4, and the shell-model structure of the residual nucleus can be determined. In stripping reaction this concerns the l-value of the nucleon captured by the target, and for pick-up reactions the l-value of the nucleon removed from the target.

The transferred angular momentum l in the direct reactions generally modifies the total angular momentum of the target nucleus J_i to the product nucleus angular momentum J_f within the values

$$||J_i - l| - \frac{1}{2} \leq J_f \leq J_i + l + \frac{1}{2}. \tag{1.2}$$

This relation together with the parity relation $\pi_i\pi_f = (-1)^l$, the knowledge of the target nucleus and the transferred angular momentum, allows us to determine the parity and the spin of the product states. Knowledge of the transferred angular momentum

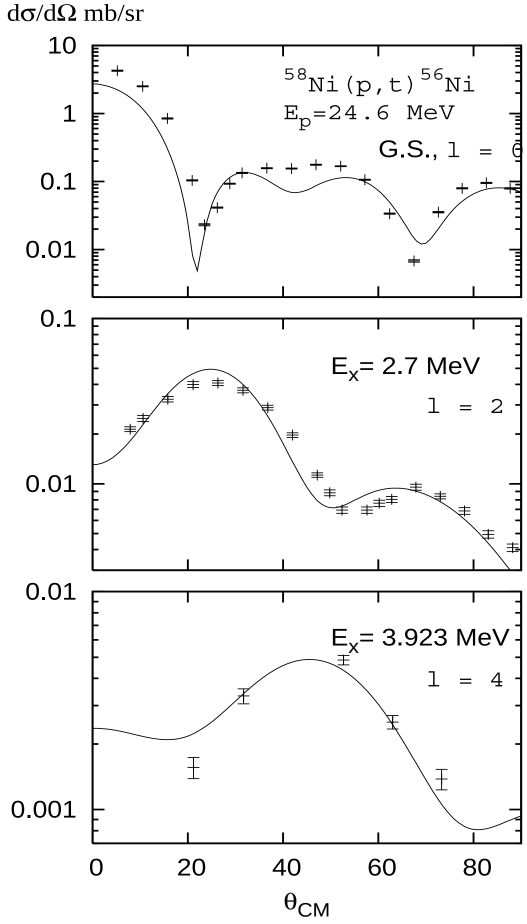

Figure 1.4.: The cross-section angular distributions for three states in ^{56}Ni from ^{58}Ni($\vec{\mathrm{p}}$, t)^{56}Ni reaction performed in this thesis frame work. The identification of the transferred angular momentum l from the shape of the angular distribution, where θ_l increases with l. The curve represents DWBA calculations.

allows us to test the predictions of the shell model for the structure of the low lying states of the nuclei. For example, one can compare Figure 1.5, which shows the single particle levels of the nuclear shell model, with the results of the stripping reaction ^{54}Fe($\vec{\mathrm{d}}$, p)^{55}Fe performed in this thesis frame work, which will be presented in more details later. The ground state of $^{54}_{26}$Fe$_{28}$ has, with the full $1f_{7/2}$ neutron shell, total angular momentum of $J_i^\pi = 0^+$. If one adds one more neutron, one would expect it to be in the $2p_{3/2}$ orbital, leading to $J_f^\pi = 3/2^-$ ground state in ^{55}Fe. This can be confirmed by observing an $l = 1$ angular distribution in the ($\vec{\mathrm{d}}$, p) stripping reaction for the ^{55}Fe ground state. However, sometimes the real situation is more complicated, due to the residual interaction, configuration mixing, particle-hole configurations, etc. The consequence is that a single-particle state will not always generate a single final state. Rather it can mix with other configurations with the same angular momentum

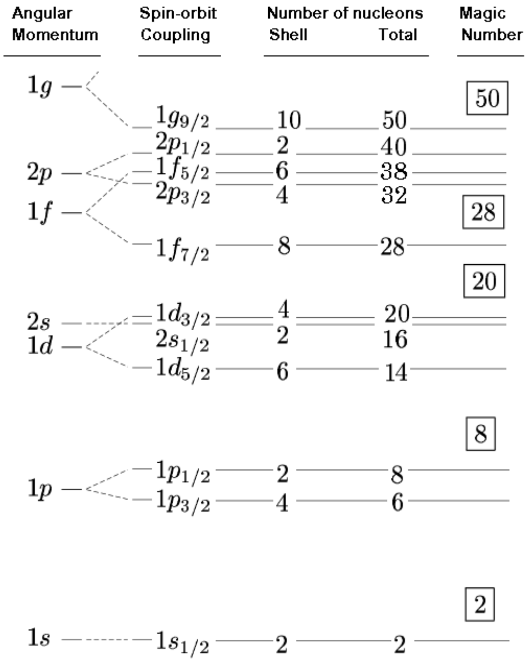

Figure 1.5.: The single particle levels of the nuclear shell model.

and parity to generate a series of states with the same angular momentum. Each one of them spending just some of their time in the single particle configuration. As a results, the cross-section for the formation of a state i of the product nucleus is related to the one calculated with the DWBA (as explained in Section 1.4) for the formation from a single-particle state by

$$\left(\frac{d\sigma}{d\Omega}\right)_{\text{exp}} = \frac{2J_f+1}{2J_i+1} S_{ij} \left(\frac{d\sigma}{d\Omega}\right)_{\text{DWBA}} \tag{1.3}$$

where the spectroscopic factor S_{ij} measures the weight of the configuration j used in the DWBA calculation, in the final state i measured experimentally, with the sum of the contributions limited to

$$\sum_i S_{ij} = n_j. \tag{1.4}$$

The sum includes all the states i of the product nucleus that contain a given configuration j, with total number of nucleons equal to n_j. The value S', which is

$$S' = \frac{2J_f+1}{2J_i+1} S_{ij} \tag{1.5}$$

is extracted by adjusting the calculated angular distribution curves to the experimental ones.

Therefore the single-nucleon transfer reactions, like the stripping (d,p) and the pick-up reactions (p,d), provide us with information about the single particle structure. The two-nucleon transfer reactions, like the stripping (t,p) and the pick-up (p,t) reactions, are very sensitive to pair correlations in the nucleus. However, some care should be taken here since the angular momentum is carried by a pair of nucleons, so that it does not directly reflect the angular momentum of the single particle states into which the nucleons are transferred. The angular momentum of the pair can be shared in different ways to form the final angular momentum and nothing in the transferred angular momentum distinguishes between those ways. Therefore, all those possibilities must contribute coherently to the reaction. The coherence can produce large cross-sections in states for which it is constructive and very small cross-sections in states when it is destructive. The two-nucleon transfer reactions provide a means of testing the nuclear wave function in details not accessible by the single-nucleon transfer reactions.

1.3. The Optical Potential

In the so called optical model the nucleus is considered as a cloudy crystal ball. When struck by a beam of particles, it scatters a part of the beam and absorbs a part, analogous to the cloudy crystal ball behavior with light. In this model the interaction between the nuclei is described by the potential $U(r)$, where r is the distance between the center of mass of the two nuclei. The absorption part is included by using a complex potential. The real part represents the elastic scattering and describes the ordinary nuclear interaction between the target and the projectile. Therefore, it is similar to the shell-model potential. The imaginary part represents the absorption of the particles or, in another meaning, the disappearance of particles from the elastic channel. A commonly used form for the optical model is

$$U(r) = U_R(r) + U_I(r) + U_D(r) + U_S(r) + U_C(r) \tag{1.6}$$

which contains parameters that vary with energy and masses of nuclei. Therefore, the parameters should be chosen by adjustment to the experimental data.

The first term

$$U_R(r) = -V \cdot f(r, R, a) \tag{1.7}$$

is the real potential representing a nuclear well with depth V and multiplied by a Woods-Saxon form factor

$$f(r, R, a) = \frac{1}{1 + e^{\frac{r-R}{a}}} \tag{1.8}$$

where R is the radius of the nucleus and a is the diffuseness of the potential, Figure 1.6.

The absorption part is taken into account by including the two imaginary parts, $U_I(r)$ which is responsible for the absorption in the whole volume of the nucleus and $U_D(r)$ which acts specifically in the region close to the nuclear surface, Figure 1.6.

$$U_I(r) = -iW \cdot f(r, R_I, a_I) \tag{1.9}$$

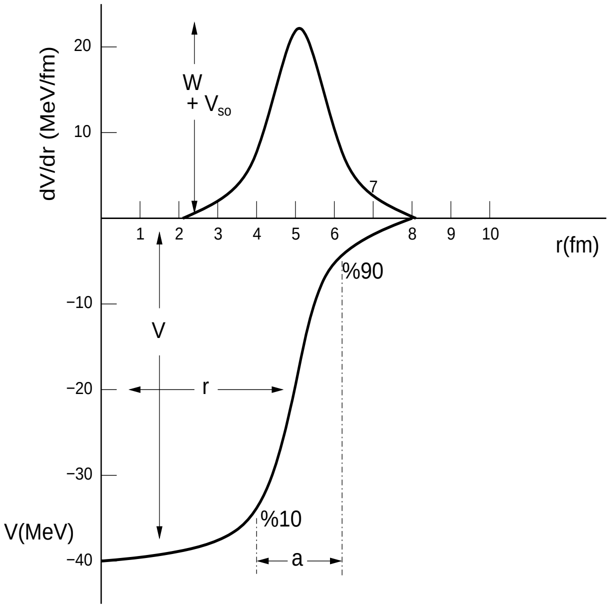

Figure 1.6.: The optical model functions for the real potential V and the surface imaginary potential $W = dV/dr$.

and

$$U_D(r) = 4ia_I W_D \frac{d}{dr} f(r, R_I, a_I). \tag{1.10}$$

At low energies, where no possibility for interaction with deep inner nucleons exists and the interactions are essentially concentrated at the surface of the nucleus, only $U_D(r)$ is important and $U_I(r)$ can be ignored. In contrast, at high energies, where the incident projectile has larger penetration and interacts strongly with the whole nucleons, $U_I(r)$ is important.

As in the shell-model potential, a considerable improvement was obtained by including a spin-orbit term to the optical potential. The spin-orbit term is usually written as

$$U_S(r) = s \cdot l \, \Big(\frac{\hbar}{m_\pi c^2}\Big)^2 \, V_s \frac{1}{r} \frac{d}{dr} f(r, R_s, a_s) \tag{1.11}$$

where m_π is the pion mass, s is the spin and l the angular momentum operator. The $U_S(r)$ part is also only important at the surface of the nucleus, since the nuclear spin depends strongly on the nucleons on the surface. V_s, R_s and a_s must be adjusted by comparing to experimental data.

The last term $U_C(r)$ corresponds to the Coulomb potential. It has the form

$$U_C(r) = \begin{cases} \frac{zZe^2}{2R_c}\left(3 - \frac{r^2}{R_c^2}\right) & r \leq R_c \\ \frac{zZe^2}{r} & r > R_c \end{cases}$$

where the nucleus is assumed to be a uniformly charged sphere of the Coulomb barrier radius $R_c = r_c A^{1/3}$. Here, z is the projectile charge, Z is the target nucleus charge. The *'standard form'* for the optical potential given by C. M. Perey and F. G. Perey [32] and widely used in this thesis, is presented in the appendix: A.

1.4. DWBA Calculations

As previously presented, the distinction between direct and compound nuclear reactions can be obtained by the reaction time. Direct reactions require a time in the same order of magnitude of the time the projectile needs to traverse the nucleus. Because of this short time and the fact that the reactions happen in a single-step process, the memory of the direction of motion of the projectile will not be lost during the reaction. In other words, from the angular distribution it is possible to estimate the direction of motion for the incident projectile. This property of the direct reaction has led to the single-step description of the process referred to as the Distorted Wave Approximation (DWA). The plane wave theory was soon replaced by the DWA that included refractive and absorptive effects, and the Born approximation was extended to the Distorted Wave Born Approximation (DWBA).

The concept of DWBA calculations is common for all direct reactions. Information from the elastic scattering for the initial and final reaction channel at or near the energy of the reaction under consideration are used to obtain the optical-model parameters. The distorted wave describes the relative motion between the reacting particles. The form of the nuclear overlap function depends on the particular reaction under consideration and takes the form

$$(\Phi_\beta | V_\beta - U_\beta | \Phi_\alpha)$$

where α and β denote the two-body partitions for the input and the output channels, respectively, Φ_α and Φ_β are the nuclear wave functions in the reaction input channel α and in the reaction output channel β. The interaction V_β is the real potential which binds the transferred valance particle to the core, U_β is the optical potential for channel β. If we consider the (d,p) stripping reaction

$$\mathrm{d} + A \longrightarrow \mathrm{p} + B \qquad (B = A + \mathrm{n}) \tag{1.12}$$

with $\alpha = \mathrm{d} + A,\ \beta = \mathrm{p} + B$, the general form of the transition amplitude is

$$T_{\alpha\beta} = W \left\langle \chi_\beta^{(-)} \Phi_\beta | V_\beta - U_\beta | \Phi_\alpha \chi_\alpha^{(+)} \right\rangle \tag{1.13}$$

where W is the statistical weight of the direct terms and $\chi_\alpha^{(+)}$, $\chi_\beta^{(-)}$ are the distorted waves for the incoming and outgoing particles, respectively.

The interaction will be written as

$$V_\beta = V_{\mathrm{pn}} + \sum_{\mathrm{i}=1}^{A} V_{\mathrm{pi}} \equiv V_{\mathrm{pn}} + V_{\mathrm{pA}} \tag{1.14}$$

V_{pA} should have the general effect that is described by the one-body optical potential U_{p} and that the difference

$$\langle V_{\mathrm{pA}} - U_{\mathrm{p}} \rangle \simeq 0 \tag{1.15}$$

Φ_α and Φ_β take the particular form

$$\Phi_\alpha = \Phi_{J_A}^{M_A}(\mathbf{A})\phi_{\mathrm{d}}(r)X_1^{\mu_{\mathrm{d}}}(\sigma_{\mathrm{n}}, \sigma_{\mathrm{p}}) \tag{1.16}$$

$$\Phi_\beta = \Phi_{J_B}^{M_B}(\mathbf{A}, \mathbf{r}_{\mathrm{n}})X_{1/2}^{\mu_{\mathrm{p}}}(\sigma_{\mathrm{p}}) \tag{1.17}$$

where A refers to the nucleon coordinates and spins, X denotes spin wave functions, σ_{n} and σ_{p} denote neutron and proton spin coordinates and ϕ_{d} denotes the deuteron radial function. With approximation (1.15), we recognize that the remaining interaction does not depend on the A coordinates, so that in (1.13) we can consider separately the integral

$$\int \Phi_{J_B}^{M_B^*}(\mathbf{A}, \mathbf{r}_{\mathrm{n}})\Phi_{J_A}^{M_A}(\mathbf{A})d\mathbf{A}. \tag{1.18}$$

It is customary to introduce a fractional parentage expansion of the nuclear wave function, which for the present purpose would be a single particle parentage, namely, (see M. H. Macfarlane and J. B. French [29] and N. K. Glendenning [11])

$$\Phi_{J_B}^{M_B}(\mathbf{A}, \mathbf{r}_{\mathrm{n}}) = \sum_{A'jl} \beta_{jl}(\mathrm{B}, \mathrm{A}')\mathcal{A}[\Phi_{J_{A'}}(\mathbf{A})\phi_{nlj}(\mathbf{r}_{\mathrm{n}})]_{J_B}^{M_B} \tag{1.19}$$

where $\mathcal{A}$ is an antisymmetrization operator (see N. K. Glendenning [12]). The β are generalized coefficient of fractional parentage of the nuclear wave function. In principle there would be a sum over the radial quantum number n in 1.19. However, the shell model tells us which radial state is in question. As a particularly trivial example, suppose B is a closed-shell nucleus plus one neutron. In that case,

$$\Phi_{J_B}^{M_B}(\mathbf{A}, \mathbf{r}_{\mathrm{n}}) = \mathcal{A}\{\Phi_0^0(\mathbf{A})\phi_{nlj}^m(\mathbf{r}_{\mathrm{n}})\}\delta_{jJ_B}\delta_{mM_B} \tag{1.20}$$

In 1.19 the square bracket denotes vector coupling:

$$[\Phi_{J'}\phi_j]_J^M = \sum_{M'm} C_{M'mM}^{J'\,j\,J}\Phi_{J'}^{M'}\phi_j^m \tag{1.21}$$

and ϕ_{nlj} denotes a spin and orbital wave function for a shell model state

$$\phi_{nlj}^m(\mathbf{r}_{\mathrm{n}}, \sigma_{\mathrm{n}}) = [\phi_{nl}(\mathbf{r}_{\mathrm{n}})X_{1/2}(\sigma_{\mathrm{n}})]_j^m \tag{1.22}$$

$$\phi_{nl}^{m_l}(\mathbf{r}_{\mathrm{n}}) = u_{nl}(\mathbf{r}_{\mathrm{n}})Y_l^{m_l}(\hat{\mathbf{r}}_{\mathrm{n}}), \tag{1.23}$$

where u_{nl} is the radial wave function. From 1.18, 1.19 and the antisymmetrization definition (see N. K. Glendenning [12]) it follows, and $Y_l^{m_l}$ is the spherical harmonics.

$$\begin{pmatrix} A+1 \\ 1 \end{pmatrix}^{1/2} \int \Phi_{J_B}^{M_B^*}(\mathbf{A}, \mathbf{r}_{\mathrm{n}})\Phi_{J_A}^{M_A}(\mathbf{A})d\mathbf{A} \tag{1.24}$$

$$= \sum_{jl} \beta_{lj}(\mathrm{B}, \mathrm{A})C_{M_A m_j M_B}^{J_A\,j\,J_B}\phi_{nlj}^{m^*j}(\mathbf{r}_{\mathrm{n}}, \sigma_{\mathrm{n}}).$$

where the matrix describes the number of ways of selecting the one neutron from (A + 1) neutrons. The square of the amplitude β is often called the spectroscopic factor (see M. H. Macfarlane and J. B. French [29] and N. K. Glendenning [11])

$$S_{lj}^{1/2} = \beta_{lj} = \int d\mathbf{A} d\mathbf{r}_{\rm n} \Phi_{J_B}^{M_B^*}(\mathbf{A+1}) \mathcal{A}[\Phi_{J_A}(\mathbf{A})\phi_{nlj}(\mathbf{r}_{\rm n})]_{J_B}^{M_B}. \tag{1.25}$$

$$= \begin{pmatrix} A+1 \\ 1 \end{pmatrix}^{1/2} \int d\mathbf{A} d\mathbf{r}_{\rm n} \Phi_{J_B}^{M_B^*}(\mathbf{A+1}) [\Phi_{J_A}(\mathbf{A})\phi_{nlj}(\mathbf{r}_{\rm n})]_{J_B}^{M_B}$$

If the neutrons and protons are distinguished, as in this example, then

$$\begin{pmatrix} A+x \\ x \end{pmatrix} \leftarrow \begin{pmatrix} N+\nu \\ \nu \end{pmatrix} \begin{pmatrix} Z+\pi \\ \pi \end{pmatrix}, \tag{1.26}$$

where ν and π are the number of neutrons and protons transferred. Combining those results with 1.13 leads to

$$T_{\rm pd}(J_A M_A \mu_{\rm d} \rightarrow J_B M_B \mu_{\rm p}) = \sum_{lj} C_{M_A m_j M_B}^{J_A\ j\ J_B} C_{\mu_{\rm p}\ \ \mu_{\rm n}\ \ \mu_{\rm d}}^{(1/2)(1/2)(1)} C_{m_l\ \mu_{\rm n}\ m_j}^{l\ (1/2)\ j} \tag{1.27}$$

$$\times \quad i^l (2l+1)^{1/2} \mathrm{B}_l^{m_l} S_{lj}^{1/2}$$

where

$$\mathrm{B}_l^{m_l}(\mathbf{k_p}, \mathbf{k_d}) = i^{-l}(2l+1)^{-1/2} \int \chi_{\rm p}^{(-)^*}(\mathbf{k_p}, \mathbf{r_p}) \phi_{nl}^{m_l^*}(\mathbf{r_n}) V_{np}(r) \chi_{\rm d}^{(+)}(\mathbf{k_d}, \mathbf{r_d}) \phi_{\rm d}(r) d\mathbf{r_n} d\mathbf{r_p} \tag{1.28}$$

$\mathrm{k_p}$ and $\mathrm{k_d}$ denote the relative momenta. Now let us discuss the differential cross-section of particles scattered in the direction θ, which is defined as the flux of scattered particles through the area $dA = r^2 d\Omega$ in the direction θ, per unit incident flux. The quantum mechanical current associated with a wave function ψ is

$$j = \frac{\hbar}{2mi}(\psi^* \nabla \psi - \psi \nabla \psi^*) \tag{1.29}$$

The scattered flux passing through dA in the channel β, for example, is obtained from the radial component of j. The radial component is

$$(\hat{r}_\beta \cdot j_\beta) d\mathbf{A} = \frac{\hbar k_\beta}{m_\beta} |f_{\beta\alpha}(\theta)|^2 d\Omega + O(\frac{1}{r_\beta}) \tag{1.30}$$

where the second term vanishes as $r_\beta \rightarrow \infty$. The incident flux passing through unit area, which is along the axis, is obtained from the plane wave (see [12]) as $\hbar k_\alpha / m_\alpha$. Thus the differential cross-section is

$$d\sigma = \frac{m_\alpha}{m_\beta} \frac{k_\beta}{k_\alpha} |f_{\beta\alpha}(\theta)|^2 d\Omega \tag{1.31}$$

or in terms of the t matrix

$$\left(\frac{d\sigma}{d\Omega}\right)_{\beta\alpha} = \frac{m_\alpha m_\beta}{(2\pi\hbar^2)}\frac{k_\beta}{k_\alpha}|T_{\beta\alpha}|^2. \tag{1.32}$$

Applying the previous discussion to the (d,p) reaction results in

$$\left(\frac{d\sigma}{d\Omega}\right)(J_A M_A \mu_\mathrm{d} \rightarrow J_B M_B \mu_\mathrm{p}) = \frac{m_\mathrm{d} m_\mathrm{p}}{(2\pi\hbar^2)}\frac{k_\mathrm{p}}{k_\mathrm{d}}|T|^2 \tag{1.33}$$

where m_d and m_p are the deuteron and proton reduced masses, respectively. Usually one does not measure the spin direction $\mu_B M_B$, therefore the measured cross-section is a sum over all final orientations produced by an average initial orientation

$$\begin{aligned}\left(\frac{d\sigma}{d\Omega}\right) &= \frac{1}{3(2J_A+1)}\sum_{M_B\mu_\mathrm{p}}\sum_{M_A\mu_\mathrm{d}}\frac{d\sigma}{d\Omega}(J_A M_A \mu_\mathrm{d} \rightarrow J_B M_B \mu_\mathrm{p}) \\ &= \frac{1}{2}\frac{m_\mathrm{d} m_\mathrm{p}}{(2\pi\hbar^2)^2}\frac{k_\mathrm{p}}{k_\mathrm{d}}\frac{2J_B+1}{2J_A+1}\sum_{ljml} S_{lj}|\mathrm{B}_l^{ml}|^2 \end{aligned} \tag{1.34}$$

This expression exhibits a division into two factors: S_{lj} the spectroscopic factor, which is determined solely by the properties of the nuclei and a factor $|\mathrm{B}|^2$, which contains all of the kinematic dependence through the wave functions of the relative motion and their overlap with each other in addition to the nuclear wave function of the transferred neutron.

1.4.1. The CHUCK3 Code

According to the previous discussions the reaction cross-section can be estimated using the DWBA, for which among others, the computer codes FRESCO [42], DWUCK [24] and CHUCK3 [23] are available. In this thesis DWBA calculations were performed utilizing the CHUCK3 code.

The coupled channels code CHUCK3 is a program to calculate the reaction cross-section by numerically solving an appropriate set of coupled equations. In addition to simple DWBA calculations, in which the particle transfer is treated as a direct one-step process, it is also possible to couple different reaction path ways (channels) from initial to final state through intermediate states. It can consider many channels, not only one-way coupling. It is necessary to include the exact coupling strength BETA in the input file, where BETA = $S_{lj}^{1/2} \times D_0$ for single-nucleon transfer reaction, BETA = $\sqrt{9.7} \cdot S_{lj}^{1/2} \times D_0$ for two-nucleon transfer reaction and D_0 is the true overlap. The coupling strength values for some reactions are listed in Table 1.1 from the CHUCK3 manual by P. D. Kunz [23].

In the CHUCK3 input file one should take care about a few points. The code accepts a maximum of 8 channels, which limited our results as will be discussed later, Section 4.2.6. The elastic channel must be the first one. One should also take care of multiplication factors if a certain set of parameters is used. For example if the C. M. Perey and F. G. Perey [32] optical model form is used, volume real and imaginary

Particles	Isospin factor	Amplitude	$S^{1/2}$	$S^{1/2}D_0$
p(n)d	$(\frac{1}{2}\frac{1}{2}-\frac{1}{2}\frac{1}{2}\|00)=\frac{-1}{\sqrt{2}}$	1	-1	122.5
n(p)d	$(\frac{1}{2}\frac{1}{2}\frac{1}{2}-\frac{1}{2}\|00)=\frac{1}{\sqrt{2}}$	1	+1	-122.5
d(n)t	$(0\frac{1}{2}0\frac{1}{2}\|\frac{1}{2}\frac{1}{2})=1$	$\frac{1}{\sqrt{2}}$	$\sqrt{\frac{3}{2}}$	-225
p(2n)t	$(\frac{1}{2}1-\frac{1}{2}1\|\frac{1}{2}\frac{1}{2})=-\sqrt{\frac{2}{3}}$	$\frac{-1}{\sqrt{2}}$	1	-1560*

Table 1.1.: The coupling strength values for some reactions used in CHUCK3, from P. D. Kunz manual [23]. $*$ Includes the factor $\sqrt{9.7}$ for the two-nucleon transfer.

potentials V_r and W must be negative. The surface imaginary potential W_D must be multiplied by factor of 4. The spin-orbit potential V_{so} also must be negative and multiplied by factor of 4 for neutrons and protons and 2 for deuteron.

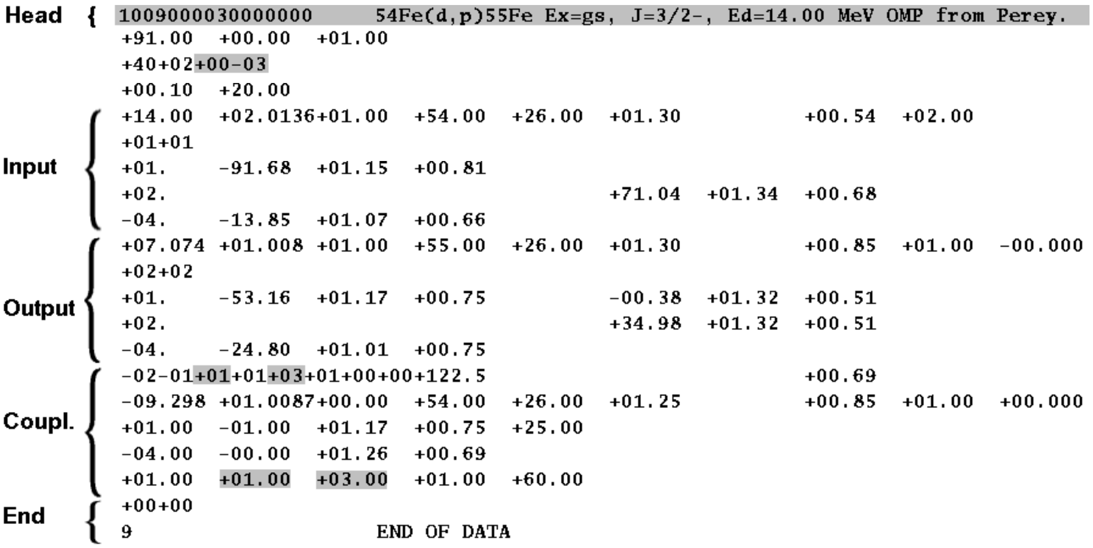

```
1009000030000000     54Fe(d,p)55Fe Ex=gs, J=3/2-, Ed=14.00 MeV OMP from Perey.
+91.00  +00.00  +01.00
+40+02+00-03
+00.10  +20.00
+14.00  +02.0136+01.00  +54.00  +26.00  +01.30          +00.54  +02.00
+01+01
+01.    -91.68  +01.15  +00.81
+02.                                    +71.04  +01.34  +00.68
-04.    -13.85  +01.07  +00.66
+07.074 +01.008 +01.00  +55.00  +26.00  +01.30          +00.85  +01.00  -00.000
+02+02
+01.    -53.16  +01.17  +00.75          -00.38  +01.32  +00.51
+02.                                    +34.98  +01.32  +00.51
-04.    -24.80  +01.01  +00.75
-02-01+01+01+03+01+00+00+122.5                          +00.69
-09.298 +01.0087+00.00  +54.00  +26.00  +01.25          +00.85  +01.00  +00.000
+01.00  -01.00  +01.17  +00.75  +25.00
-04.00  -00.00  +01.26  +00.69
+01.00  +01.00  +03.00  +01.00  +60.00
+00+00
9                    END OF DATA
```

Figure 1.7.: An example for CHUCK3 input file for the one-neutron transfer reaction $^{54}\mathrm{Fe}(\vec{\mathrm{d}},\mathrm{p})^{55}\mathrm{Fe}$, $\mathrm{E}_{\mathrm{d}}^{\mathrm{lab}}= 14$ MeV for ^{55}Fe ground state using Perey & Perey [32] OM-parameters.

Figure: 1.7 shows an example for a CHUCK3 input for the one-neutron stripping reaction $^{54}\mathrm{Fe}(\vec{\mathrm{d}},\mathrm{p})^{55}\mathrm{Fe}$ leading to the ^{55}Fe ground state with beam energy of $\mathrm{E}_{\mathrm{d}}^{\mathrm{lab}}= 14$ MeV. In this reaction one neutron is transferred from the deuteron to ^{54}Fe to produce ^{55}Fe. Since ^{54}Fe has $\mathrm{Z} = 26$ and $\mathrm{N} = 28$, from the shell model one expect the transferred neutron should occupy the $2p_{3/2}$ shell.

The CHUCK3 input file starts with a head line then lines 2 - 4 where the code is informed about the number of angles, first angle, angle increment, at which to calculate cross-section, analyzing power, etc, besides the total angular momentum of the input and the output channels and the integration step size in fm. The input file consist mainly of 3 parts (if only two channels are used):

- 1. Input channel where the reacting particles are identified (Lines 5 - 9 in this example).
- 2. Output channel where the reaction products are identified (Lines 10 - 14 in this example).
- 3. Coupling part where the code is informed, in which shell to set the transferred particle (Lines 15 - 19 in this example).

The CHUCK3 output file gives the reaction cross-section in unit of fm^2/sr, therefore it should be multiblied by a factor of 10, when the experimental cross-section is in mb/sr.

The parameters for the OM potential are taken from C. M. Perey and F. G. Perey [32]. For more details about the CHUCK3 code, please refer to P. D. Kunz [23].

Chapter 2

Experimental Apparatus

2.1. The Tandem Accelerator

The working principal of all electrostatic accelerators is to drive a particle with charge q through a potential V. In this way it gains a kinetic energy qV. Depending on this principle many types of electrostatic accelerators were built starting with the Cockroft-Walton accelerator in 1932 with a potential reaching 800 kV, through the Van de Graaff accelerator, to tandem Van de Graaff accelerators with terminal potentials in excess of 20 MV.

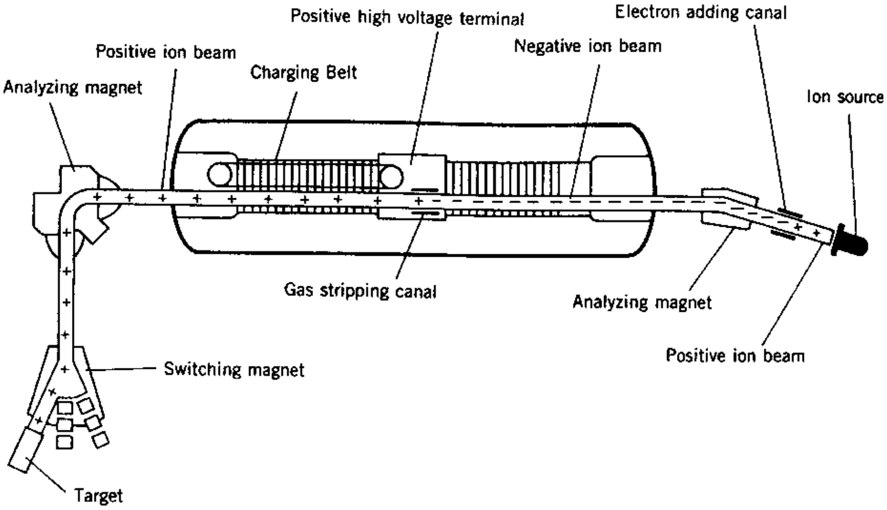

Figure 2.1.: The working principle of the Tandem Van de Graaff accelerator from K. S. Krane [21].

The principle layout of a tandem Van de Graaff accelerator is shown schematically in Figure 2.1. Singly charged negative ions are produced in the ion source. An injector preaccelerates and delivers the ions into the tandem tank. The negative ions are accelerated from the potential of the injector towards the high voltage terminal with voltage U in the middle of the tandem, resulting in kinetic energy eU. The terminal is charged by way of charging belt or chain. In the terminal the ions loose their negative charges when they pass through an electron stripper foil or gas stripping channel, turning to positive charged ions with charge state q. The positively charged ions are accelerated away from the high potential terminal towards ground potential at the end of the tandem, resulting in kinetic energy qU. In general the ions leave the Tandem tank with total energy $(q+1) \cdot U$.

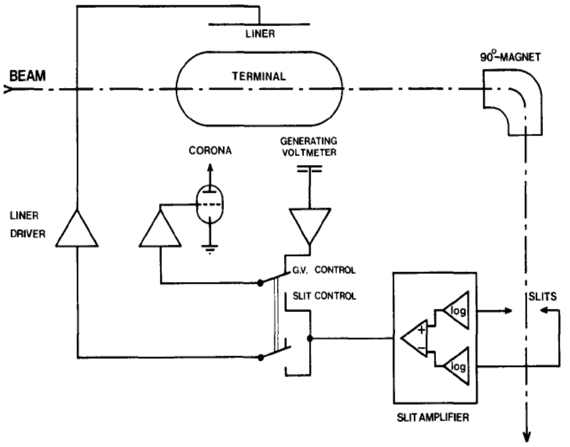

Figure 2.2.: Block diagram for MLL Tandem stabilization system, from W. Assmann *et al.* [1].

The beam energy is stabilized via an analyzing system consisting of a slit pair behind the 90° analyzing magnet. Figure 2.2 shows a block diagram of the system.
The slits measure the beam current, detect any energy deviation and send an error signal which is amplified and used to correct the terminal potential.
In this way energy stability of $\Delta E/E \approx 10^{-4}$ is achieved, for example with 14 MeV beam it is ~3 keV. Stability of the beam energy is extremely important during cross-section measurement for specific excited states.

To reach high terminal potential without discharge breakdown and sparking, the tandem tank is filled with the insulating gas SF_6 under 6×10^{-8} bar. An evacuated tube guides the ions from the source to the target which is at ground potential. For example, with terminal voltage of 7 MV protons can be accelerated to an energy of 14 MeV. Higher acceleration energy can be achieved with heavy ions, depending on the charge state after the stripper.

The MLL Tandem accelerator was used in the experiments presented in this thesis to accelerate the particle beams to the desirable energies in both normal and inverse kinematics reactions.

2.1.1. The Ion Source

In neutron transfer reactions obtaining the total angular momentum (J) for the levels is of major interest. To get information about the total transferred angular momentum, a polarized beam must be used. There are many known methods to polarize a beam of ions [31], for example the optical pumping, where the polarization happens by absorption of resonance radiation, polarization by scattering, gamma-ray polarization and polarization using Stern-Gerlach phenomenon, where the polarization is achieved by passing the beam through an appropriate magnetic field where the splitting depending on the spin occurs.

The Munich MLL Tandem beam source is using the latter method, which is why it has the name "Stern-Gerlach polarized ion source", R. Hertenberger *et al*. [15]. The polarized ion source consist of two main parts, Figure 2.3, the atomic beam source (ABS), where the beam polarization occurs using the Stern-Gerlach process and the charge exchange unit, where the beam is ionized. The ABS or Stern-Gerlach part consists of four sections: Section 1 contains the dissociator, sections 3 and 4 hold four Stern-Gerlach permanent magnets for the spin separation and section 2 between the two previous stages is equipped with additional pumps to reduce the scattering of the beam from any residual gas. The charge exchange unit also consists of two parts. The first one is the electron cyclotron resonance (ECR) plasma, where the atomic beam is ionized by electron impact. Two pancake coils (A,B) provide the axial magnetic field and six permanent dipoles (S1-S6) provide the radial magnetic field for the plasma confinement. The second part is the Cesium vapor jet, where the central part of the cesium jet crosses the ion beam and the charge exchange into negative ions by successive pickup of two electrons occurs. With such source polarized $\vec{D}^-$ and $\vec{H}^-$ ion beams of about 9μA and 15μA are obtained, respectively.

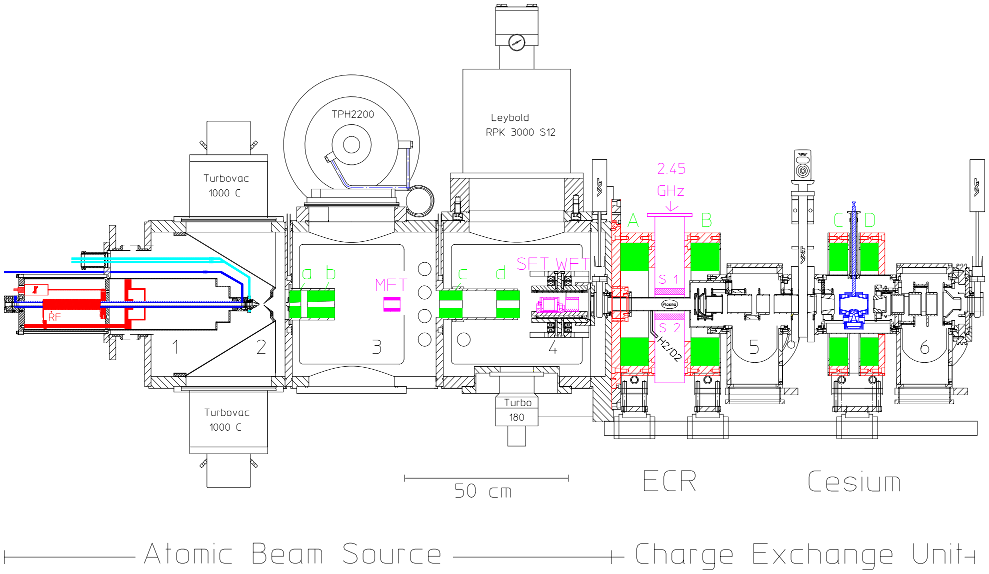

Figure 2.3.: Vertical section of the ion source: The Stern-Gerlach ABS consists of four differential pumping stages (1-4), four permanent sextupole magnets (a-d), adiabatic radio-frequency transitions (MFT,SFT,WFT) and the dissociator in vacuum chamber 1. For ECR ionization two pancake coils (A,B) produce an axial magnetic mirror field and six permanent FeNdB dipoles S1-S6 the radial magnetic field for plasma confinement. Shown are S1 and S2 only which are placed within the waveguide. The plasma within the RF-waveguide couples directly to the 2.45G Hz RF-field. Two pancake coils C and D provide a magnetic holding field near 100 mT to preserve polarization during successive pickup of two electrons in cesium vapor. The positive and negative ions are transported by a system of electrostatic electrodes, from R. Hertenberger *et al*. [15].

The spin type, up or down, and the degree of polarization of the ion beam is obtained by comparing the analysing power, equation 2.1 to the well known analysing power values from the reactions $^{12}\mathrm{C}(\vec{\mathrm{p}},\mathrm{p}_\circ)^{12}\mathrm{C}$ if a proton beam is used, and $^{65}\mathrm{Cu}(\vec{\mathrm{d}},\mathrm{d}_\circ)^{65}\mathrm{Cu}$, and equation 2.2 if a deuteron beam is used, since the deuteron is a spin 1 particle and has 3 magnetic substates m_s = 1, 0, -1.

$$A_\mathrm{y} = \frac{1}{p} \cdot \frac{\frac{d\sigma}{d\Omega}\uparrow - \frac{d\sigma}{d\Omega}\downarrow}{\frac{d\sigma}{d\Omega}\uparrow + \frac{d\sigma}{d\Omega}\downarrow} \tag{2.1}$$

$$A_\mathrm{y} = \frac{2}{3 \cdot p} \cdot \frac{\frac{d\sigma}{d\Omega}\uparrow - \frac{d\sigma}{d\Omega}\downarrow}{\frac{d\sigma}{d\Omega}\uparrow + \frac{d\sigma}{d\Omega}\downarrow} \tag{2.2}$$

where p is the beam degree of polarization, $\frac{d\sigma}{d\Omega}\uparrow$ and $\frac{d\sigma}{d\Omega}\downarrow$ are the differential reaction cross-sections obtained by using spin up or spin down polarized beam, respectively.

2.2. Forward Kinematics Tools

2.2.1. Kinematic Considerations

In forward (normal) kinematic reactions, for example $^{54}\mathrm{Fe}(\vec{\mathrm{d}},\mathrm{p})^{55}\mathrm{Fe}$, a light projectile hits a stationary and relatively heavy nucleus to produce a projectile like light outgoing particle. The detector should cover the forward angles, in the lab-system, where the light outgoing particle has higher intensity, especially if the simple angular momentum transfer $l = 1, 2, 3$ are under investigation.

Because of that, the MLL Q3D magnetic spectrograph equipped with a Cathode-Strip Detector was used to detect and analyze the light outgoing particles in this part of this thesis.

2.2.2. The Q3D

The Munich Q3D magnetic spectrograph was designed by H. A. Enge [9] and produced by Scanditronix, Stockholm in 1975. It consists mainly of a Quadrupole lens (Q) and three Dipoles magnets (D), therefore called Q3D. The apparatus has a maximum acceptance solid angle of 14.7 msr, a position resolution of 0.25 to 0.5 mm on the focal plane and an energy resolution $\Delta E/E = 0.0002$ with the full solid angle. The Q3D is sketched in Figure 2.4.

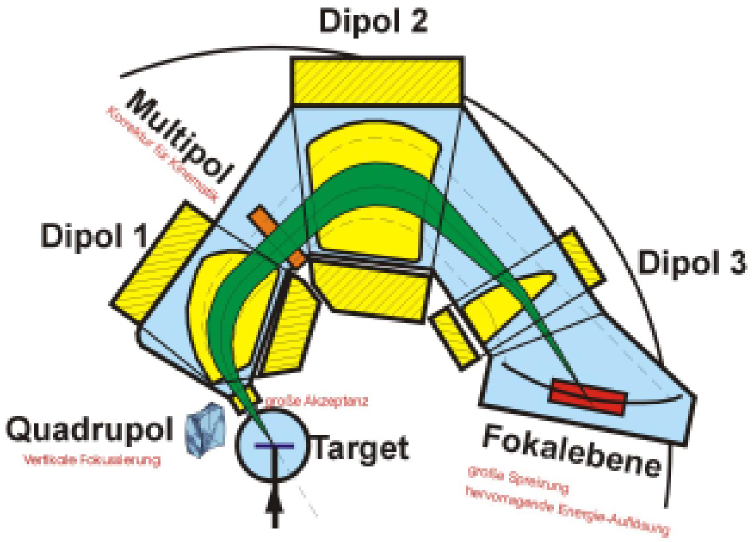

Figure 2.4.: Schematic digram for Garching Q3D magnetic spectrograph.

After a reaction takes place in the target chamber, the reaction products pass through the vertically focusing quadrupole, then they enter the dipoles where the magnetic fields at the end and the entrance of each dipole provide additional focusing. The magnetic field of the 3 dipoles also separate the particles depending on their momentum/charge ratio on different positions on the focal plane where the detector is situated. The opening solid angle $d\Omega$ of the Q3D can be changed by an entrance shutter in front of the quadrupole. The whole Q3D is built on a circular railway which allows the Q3D and the detector to be positioned at over scattering angles from 0° to 150°.

2.2.3. The Cathode-Strip Detector

In the normal kinematic reactions performed in this thesis, outgoing particles are detected by a gas-filled detector produced by H. F. Wirth [46] which has a working principle similar to that of a multiwire proportional chamber. The cathode-strip detector is based in the Q3D focal plane. The detector is filled with isobutane gas (500 mbar) and designed to detect light ions.

The detector consists of two major parts, which are shown in Figure 2.5.

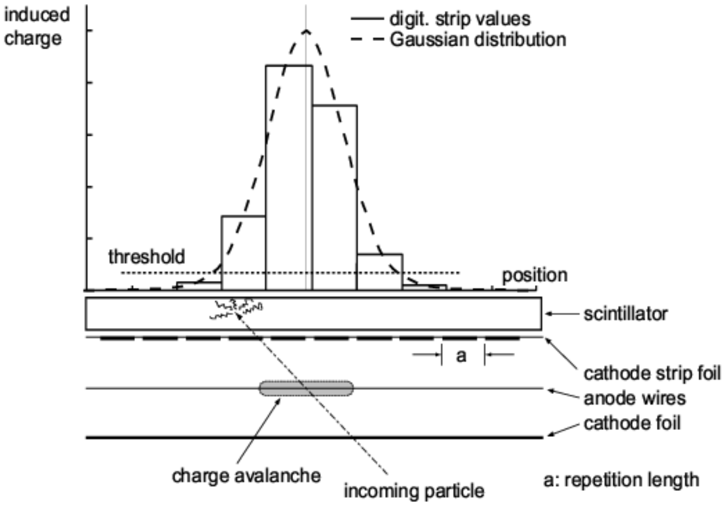

Figure 2.5.: The working principle of the cathode-strip detector from H. F. Wirth Ph.D. thesis [46]

The first one is a two-wire proportional chamber consisting of 2 anode wires (to define the detector height) between 2 cathodes, a cathode foil and a cathode strip foil with 272 strips, each 3mm wide and with 0.5 mm gaps in between. 255 of the strips are connected to individual preamplifiers. The second part is a 7mm thick plastic scintillator bar (NE-104) with two photomultipliers at both ends. The detectors active length is 89 cm.

The incoming particles ionize the gas inside the detector, producing a charge avalanche which induces a positive charge on 5 - 7 cathode strips, where the position is extracted from a fit to the pulse height distribution, see Figure 2.5. The particles are stopped in the plastic scintillator bar. The produced light is collected by the two photomultipliers. The signals are summed as the particle rest energy signal.

For each event its energy loss in the gas and its rest energy from the scintillator-photomultipliers are amplified, digitized and are combined with other information like the time and the cathode strip from which it is produced and recorded using the MARaBOU [26] data acquisition system.

Particles are identified from the energy loss and the photomultiplier signals, as described in section 2.2.4.

2.2.4. Particle Identification

Figure 2.6 illustrates how the particles are identified. On the x-axis the particle rest energy from the photomultiplier signals, on the y-axis the energy loss from the cathode strips signal is plotted. The light fast particles like the protons loose little energy in the gas and loose most of their energy in the scintillator, resulting in a small energy loss signal and high rest energy signal. Heavy slow particles like the triton or alpha loose a lot of energy in the gas and a small amount in the scintillator, resulting in a high energy loss signal and small rest energy signal.

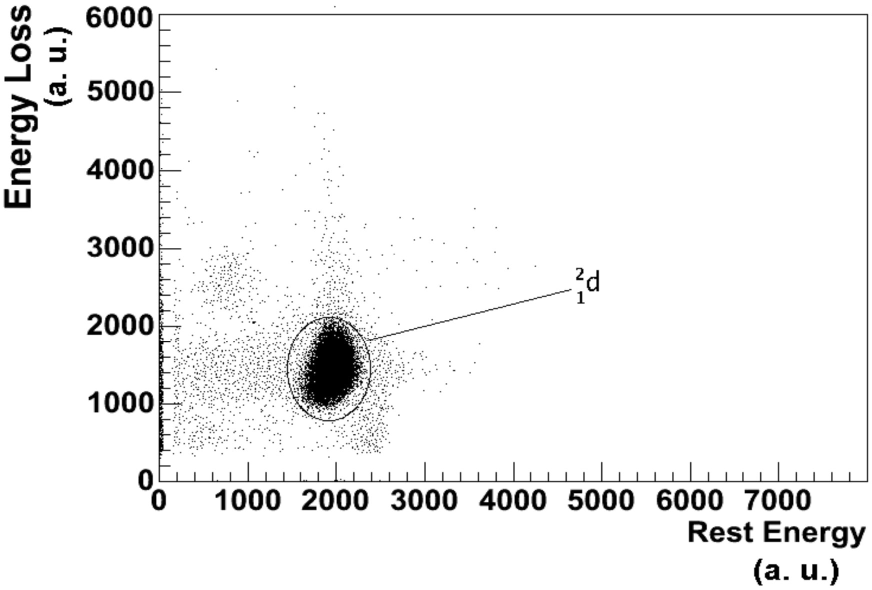

Figure 2.6.: Particle identification from the rest energy against the energy loss (using arbitrary unit for energy) in the gas signals from the reaction $^{58}\mathrm{Ni}(\vec{\mathrm{p}},\mathrm{t})^{56}\mathrm{Ni}$, $\mathrm{E}_{\vec{\mathrm{p}}} = 24.6$ MeV.

By defining a range for the energy loss and the rest energy signals, the desirable events are selected and particles from a specific reaction are collected.

2.3. Inverse Kinematics Tools

2.3.1. Kinematic Considerations

In inverse kinematic reactions where in the Lab-system frame a heavy projectile hits a stationary light nucleus, the heavy reaction products have high intensity in the forward angles and the light ejected particles, like protons produced from $\mathrm{d}(^{54}\mathrm{Fe,p})^{55}\mathrm{Fe}$ or $\mathrm{t}(^{40}\mathrm{Ar,p})^{42}\mathrm{Ar}$ reactions, will rather have high intensity in the back angles, in the lab-system.
Because of that the semiconductor detector used in inverse kinematics reactions where positioned to cover an angular range $\sim 130° \rightarrow 160°$ in the Lab-system, which for the reaction above corresponds to the angular range $\sim 10° \rightarrow 30°$ in the CM-system. This range is the best angular range to study the neutron transfers with low angular momentum transfer $l = 0$, 1 & 2.

2.3.2. The Double Sided Silicon Strip Detector (DSSSD)

The working principle of semiconductor detectors is similar to the gas ionization detector, where the radiation interacts with the detector material to produce electron-hole pairs, instead of electron-ion pairs in the ionization gas detectors, which are collected by an electric field. The energy required to produce electron-hole pairs is about 10 times less than that required to produce electron-ion pairs, which increases the detector resolution by $\sqrt{10}$. Moreover, because of their higher density they have higher stopping power, higher than the gas detectors. However, because of their crystal structure they are sensitive and can be damaged by radiation very quickly which limits their lifetime.

Because of the kinematic consideration discussed in Section 2.3.1 a Double Sided Silicon Strip Detector (DSSSD) was used in the inverse kinematic reactions. The DSSSD is a pn-junction to be operated under a reverse bias with external voltage of about 50 V, which enlarges the width of the depletion zone between p and n and provides the electric field for efficient electron-hole collection. Si semiconductors have the advantage of room temperature operation. The width of the depletion zone, which is the effective width of the detector (d), can be calculated from the relation mentioned in W. R. Leo [25]:

$$d = x_n + x_p = \left(\frac{2\varepsilon V_B}{e} \; \frac{(N_A + N_D)}{N_A \; N_D} \right)^{1/2} \tag{2.3}$$

where ε is the dielectric constant, x_n and x_p are the extent of the depletion zone in n, p-junction respectively, V_B is the bias voltage, N_A and N_D are the donor and acceptor impurity concentrations.
If $N_A \gg N_D$ and from the conductivity or resistivity relation

$$\frac{1}{\rho} \simeq e N_D \mu_e \tag{2.4}$$

where ρ is the resistivity in units of Ω cm, μ_e is the mobility of the electron and by evaluating some of the constants, we find for Silicon

$$d_{\mathrm{Si}} = \begin{cases} 0.53(\rho_n V_B)^{1/2} & \mu\mathrm{m} \quad \text{for n} - \text{type} \\ 0.32(\rho_p V_B)^{1/2} & \mu\mathrm{m} \quad \text{for p} - \text{type} \end{cases}$$

The two DSSSD used in this thesis work were produced by Micron Semiconductors Ltd. in UK, with 300 and 500 μm thickness. Figure 2.7 shows the thicker one.

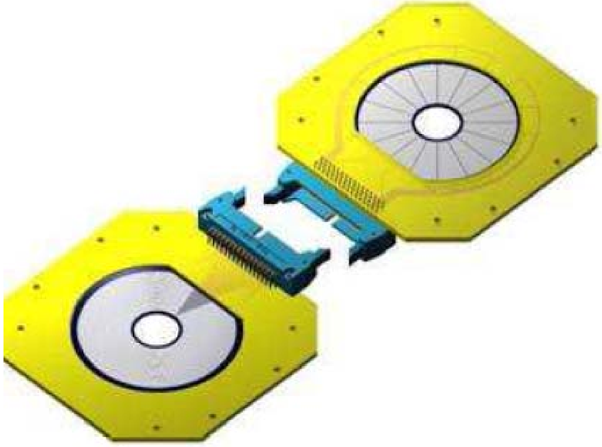

Figure 2.7.: The DSSSD used in the reaction $\mathrm{t}(^{40}\mathrm{Ar},\mathrm{p})^{42}\mathrm{Ar}$ consist of 48 rings on the front side (p-junction) and 16 sectors at the back side (n-junction). The detector is produced by Micron Semiconductors Ltd.

Such thicknesses were enough to stop the protons from the reactions up to energies of 9 and 12 MeV for the 300 and 500 μm thick detectors respectively. Both of the DSSSDs consist of 48 rings on the front side (p-junction) and 16 sectors at the back side (n-junction), they have the same geometry but different contact pads style. Each DSSSD has an active inner diameter of 22 mm and an active outer diameter of 70 mm, which means 35 cm^2 active area. The DSSSD is based on a 1.6 mm thick kapton frame to insure the detector stability and safety. The detectors were used to detect out going protons from the reactions $\mathrm{d}(^{54}\mathrm{Fe},\mathrm{p})^{55}\mathrm{Fe}$ and $\mathrm{t}(^{40}\mathrm{Ar},\mathrm{p})^{42}\mathrm{Ar}$ combined with the needed electronics as presented inFigure 2.8.

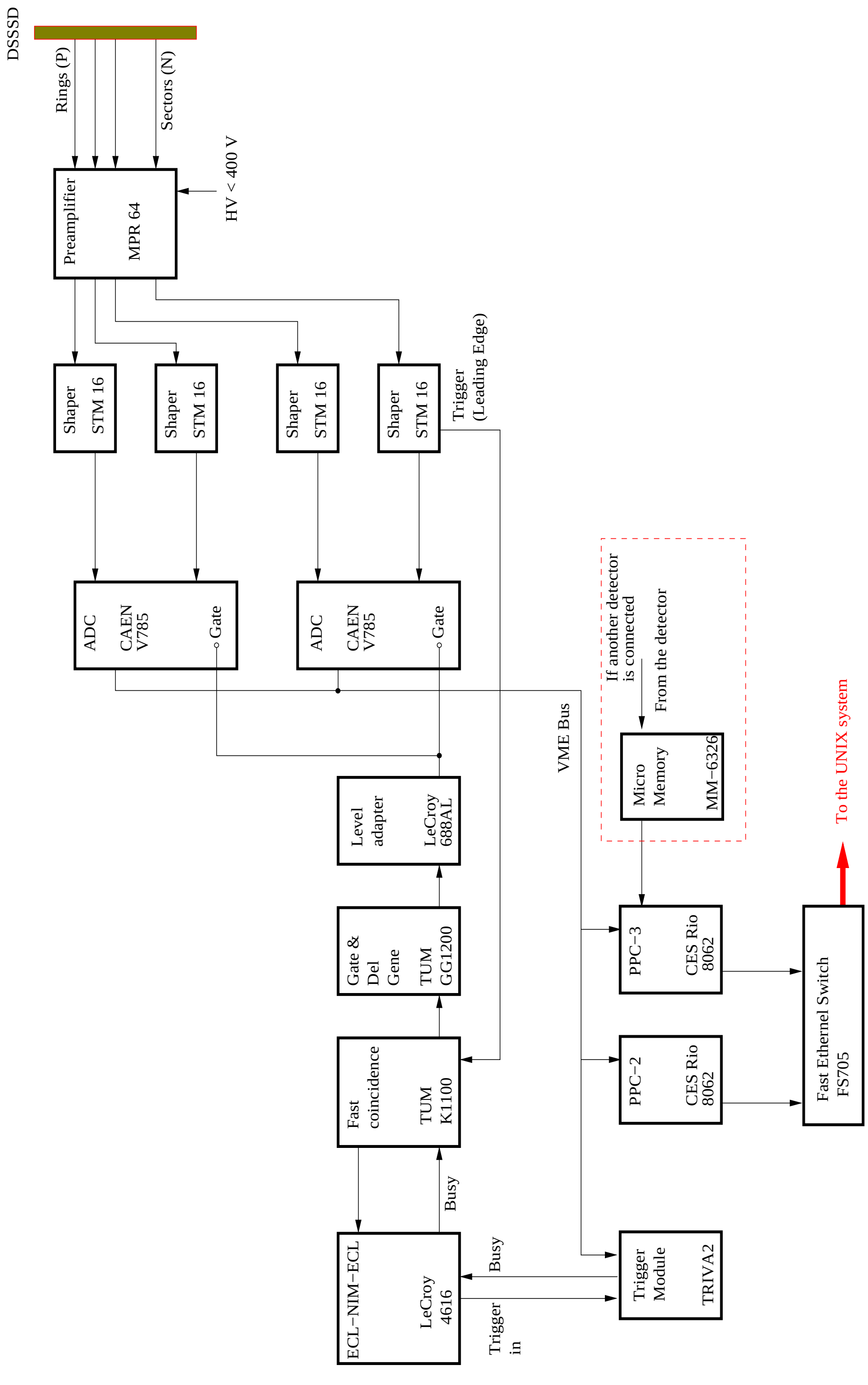

Figure 2.8.: The electronic set up for the DSSSD.

Chapter 3

Single Neutron Transfer Reaction

3.1. Forward Kinematics Reaction $^{54}\mathrm{Fe}(\vec{\mathrm{d}},\mathrm{p})^{55}\mathrm{Fe}$

3.1.1. Introduction

Neutron transfer reactions are a very powerful tool to study the structure of nuclei. Single-nucleon transfer reactions such as pick-up reactions (p,d) and (d,t) or stripping reactions as (d,p) enable the determination of many nuclear properties such as excitation energies $\mathrm{E_x}$ of individual excited state, orbital angular momentum l and the total angular momentum J if a polarized beam is used. In addition to that spectroscopic factors S can be also deduced.
The single neutron stripping reaction $^{54}\mathrm{Fe}(\vec{\mathrm{d}},\mathrm{p})^{55}\mathrm{Fe}$ was performed previously by T. Taylor *et al.* [41] and D. C. Kocher *et al.* [19], where the angular distributions of the differential reaction cross-section and the vector analyzing power were measured with beam energy of 10 MeV. Values of l, π, J besides spectroscopic factors S were deduced for a number of levels in ^{55}Fe. In this work the reaction is performed using the high resolution Q3D spectrograph, which allowed us to observe more levels, their l, π, J values and deduce more spectroscopic factors. Also great care was taken to identify levels belonging to other Fe isotopes that could falsely be identified as ^{55}Fe. For example, levels populated by the companion reactions $^{56}\mathrm{Fe}(\vec{\mathrm{d}},\mathrm{p})^{57}\mathrm{Fe}$ or $^{58}\mathrm{Fe}(\vec{\mathrm{d}},\mathrm{t})^{57}\mathrm{Fe}$ due to the target contamination.

In this thesis a detailed study of the single particle states in ^{55}Fe was performed with a particular emphasis on the $1f_{7/2}$ levels and their relation to the stability of the N = 28 shell closure. It should be mentioned that in the previous studies [41] and [19] the observed $7/2^-$ states were considered as two-step transfer, without linking them to the question of shell stability. However, our study in comparison to modern shell model calculations shows that the population of the $7/2^-$ levels in ^{55}Fe is very sensitive to the breaking of the N = 28 shell.

3.1.2. Experimental Procedure

The $^{54}\mathrm{Fe}(\vec{\mathrm{d}},\mathrm{p})^{55}\mathrm{Fe}$ reaction was studied by bombarding a $100\mu\mathrm{g/cm}^2$ thick ^{54}Fe target with 14 MeV polarized deuterons from the MLL tandem Van de Graaff accelerator. The enriched target was prepared by evaporation. Isotopic composition and target thickness are indicated in the Table 3.1

Target:	^{54}Fe
Thickness: (μg/cm^2)	100 ± 10%
Isotopes: (%)	^{54}Fe: 94.6 ^{56}Fe: 5.1 ^{57}Fe: 0.3 ^{58}Fe: -

Table 3.1.: Isotopic compositions of the target used in the $^{54}\mathrm{Fe}(\vec{\mathrm{d}},\mathrm{p})^{55}\mathrm{Fe}$ reaction.

The reaction products were analyzed with the Garching Q3D magnetic spectrograph and detected by a proportional counter filled with isobutane gas (500 mbar). More details about the experimental tools are presented in Section 2.2.
The reaction cross-section σ for ^{55}Fe levels was measured using a spin-up and spin-down polarized deuteron beam separately. The measurements covered an angular range from 5° to 40° in 5° steps plus one measurement at 50°. The differential cross-sections $\frac{d\sigma}{d\Omega}$ were measured up to an excitation energy $\mathrm{E_x}$ of 4450 keV. Each Q3D magnet setting covers an energy range of about 1400 keV, so that the Q3D was adjusted to three different magnetic settings centered at excitation energies of 600, 2200 & 3600 keV. Figure 3.1 shows the Q3D spectra for those settings at an angle of 30°.

By measuring the differential reaction cross-sections, taking the average of the measurement with spin-up or spin-down polarized beam, at different angles the angular distributions for ^{55}Fe levels were deduced.

3.1.3. Analysis

The experimental differential reaction cross-section is calculated using the known relation,

$$\frac{d\sigma}{d\Omega}(\theta) = \frac{\mathrm{Count}(\theta)}{\Delta\Omega \cdot N_{\mathrm{beam}} \cdot N_{\mathrm{target}}}. \tag{3.1}$$

Where $\Delta\Omega$ is the solid angle covered by the Q3D, N_{beam} is the integrated number of particles in the beam and N_{Target} is the number of particles in the target per cm^2.

N_{beam} is determined by dividing the total measured electric charge of the deuterons hitting the target by the electron charge

$$N_{\mathrm{beam}} = \frac{Q_{\mathrm{beam}}}{e} = \frac{I \cdot t}{e} = \frac{\left[\frac{\mathrm{Scaler1}-\mathrm{Scaler3}}{1000} \cdot \mathrm{skf} \cdot 10^{\mathrm{exp}}\right]}{1.6 \times 10^{-19}} \tag{3.2}$$

where the scaler values are obtained from the data acquisition system MARaBOU [26] and related to the number of the particles measured in the Faraday cup after the target, $\mathrm{skf} \cdot 10^{\mathrm{exp}}$ is adjustable charge/scaler ratio of the current integrator.

N_{target} is calculated from the target thickness and the target angle θ_{target} relative to the beam direction.

$$N_{\mathrm{target}} = \left[\frac{\rho_{\mathrm{target}} \cdot N_A}{A}\right] \cdot \frac{1}{\cos(\theta_{\mathrm{target}})} * T_{\mathrm{enr.}} \tag{3.3}$$

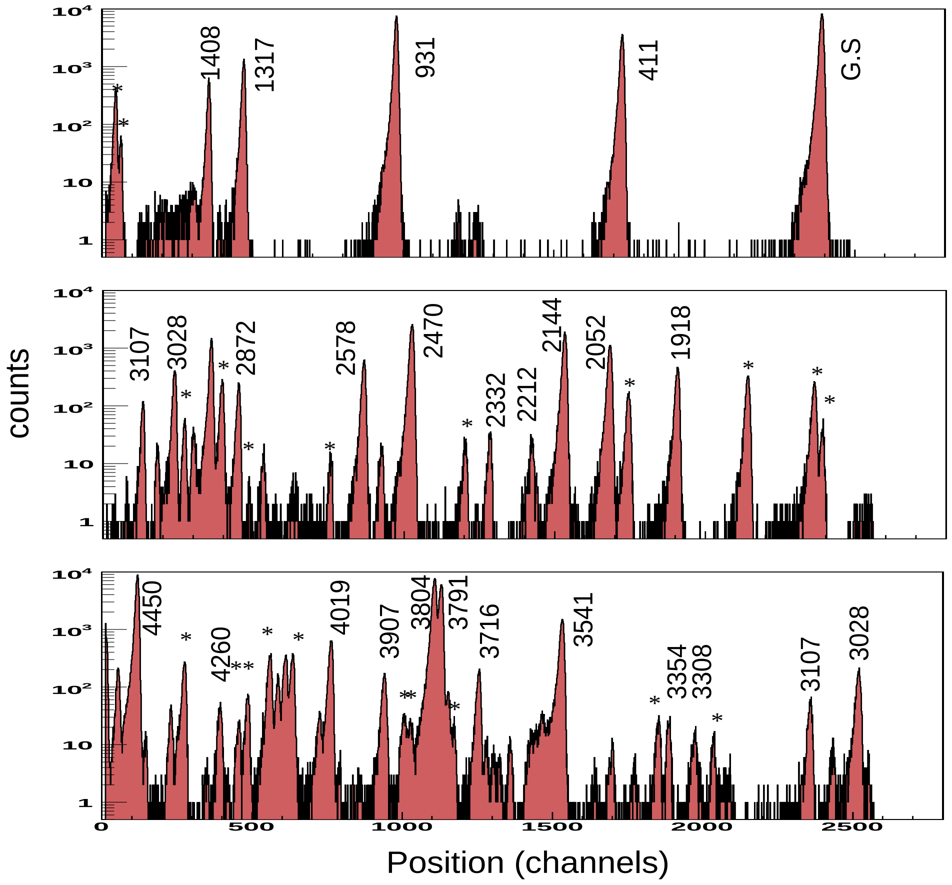

Figure 3.1.: Focal plane spectra of the Q3D observed at 30° with spin up polarized deuteron beam for the reaction ^{54}Fe($\vec{\mathrm{d}}$, p)^{55}Fe. Q3D excitation energy setting centered at about 600 keV (top), 2200 keV (middle) and 3600 keV (bottom), * ^{57}Fe levels (see Figure 3.2 and 3.3) . Energies as obtained in this work and in keV..

where ρ_{target} is the target thickness in unit of g/cm^2, N_A is the Avogadro number and A is the target nucleus mass number, $T_{\mathrm{enr.}}$ is the target enrichment.
Since a polarized beam was used, the analyzing power was also measured using the relation

$$A_{\mathrm{y}} = \frac{2}{3 \cdot p} \cdot \frac{\frac{d\sigma}{d\Omega} \uparrow - \frac{d\sigma}{d\Omega} \downarrow}{\frac{d\sigma}{d\Omega} \uparrow + \frac{d\sigma}{d\Omega} \downarrow} \tag{3.4}$$

where p is the beam degree of polarization, which was 0.65 in this experiment.

$\frac{d\sigma}{d\Omega} \uparrow$ and $\frac{d\sigma}{d\Omega} \downarrow$ are the differential reaction cross-sections for spin up and down beams, respectively. The transferred angular momentum l and the total angular momentum j of the levels are obtained by comparing the shapes of the experimental cross-section and analyzing power angular distribution, respectively, to those from well known levels and to the theoretical calculations using the Distorted Wave Born Approximation (DWBA), Section 1.4. The parity of the levels is obtained from the relation $\pi = (-1)^l$.

A number of unknown levels were observed in the ^{54}Fe spectra, which either could

Target:	^{54}Fe	^{56}Fe
Thickness: (μg/cm^2)	50	45
Isotopes: (%)	^{54}Fe: 92.9	^{54}Fe: 0.05
	^{56}Fe: 6.9	^{56}Fe: 99.9
	^{57}Fe: 0.2	^{57}Fe: 0.05
	^{58}Fe: -	^{58}Fe: < 0.05

Table 3.2.: Isotopic compositions of the target used in the $^{54}\mathrm{Fe}(\vec{\mathrm{d}},\mathrm{p})^{55}\mathrm{Fe}$ and $^{56}\mathrm{Fe}(\vec{\mathrm{d}},\mathrm{p})^{57}\mathrm{Fe}$ reactions to identify ^{57}Fe levels.

be new levels in ^{54}Fe or due to the dominant ^{56}Fe target impurity, therefore the (d, p) reaction was repeated again in a separate beamtime using a highly enriched ^{56}Fe target with purity of 99.9%. Table 3.2 shows the targets isotopic composition and thickness. Figures 3.2 and 3.3 show a comparison between ^{57}Fe and (^{55}Fe + ^{57}Fe) spectra. By comparing those spectra the ^{57}Fe levels were identified.

The focal plane spectra were fitted using the program GASPAN, Version 11.03.2005, which is a program to fit gamma and particle spectra. The program has been created by Friedrich Riess [38]. GASPAN fit parameters were varied to obtain the best fit. The 2500 channel focal plane spectra were divided into 5 regions to satisfy the GASPAN limitation of <1500 channel and to improve the fit quality. Tails were included in the peak fit and were set as a left tail type with decay constant and tail amplitude about 48% and 5.41, respectively. The background was very low, so that it was fixed to zero. Peaks within the same spectrum region had a width fixed to 9.00 channel, with variation range of ±50%, in general the peaks had FWHM of 6 keV. Since the peaks have Gaussian shape, χ^2 test divided by the number of data points N was performed to describe the quality of the fit. The χ^2/N for the fit was around 1.7 and in few fit regions rose to 8 where the fit was disturbed by background lines. An example for the fit is illustrated in Figure 3.4
The energy calibration was done with some well known peaks of ^{55}Fe. The calibration peaks are shown in Figure 3.1.

The experimental differential cross-section and analyzing powers were compared to the (DWBA) calculations, utilizing the coupled-channel code CHUCK3, Section 1.4.1. Three different sets for the Optical Model (OM) parameters (please refer to Section 1.3) were used separately in CHUCK3 to obtain the best agreement with the experimental results. An example for CHUCK3 input file is illustrated in Figure 1.7.

The first OM-parameters set is taken from C. M. Perey and F. G. Perey [32], which is valid for A > 40 and E < 50 MeV. The spin orbit potential V_{so} was taken from the book Theoretical Nuclear Physics by Herman Feshbach [6]. The second OM-parameters set was taken from a paper by T. Taylor and J. A. Cameron [41] after scaling $\mathrm{E}_{\mathrm{Beam}}$ to fit E_{d} = 14 MeV in this work. The last OM-parameters set is taken from the book Theoretical Nuclear Physics, by Herman Feshbach [6]. The OM-parameters sets are listed in the Tables 3.3, 3.4 and 3.5.
After comparing the three OM-parameters sets with our experimental data, Perey &

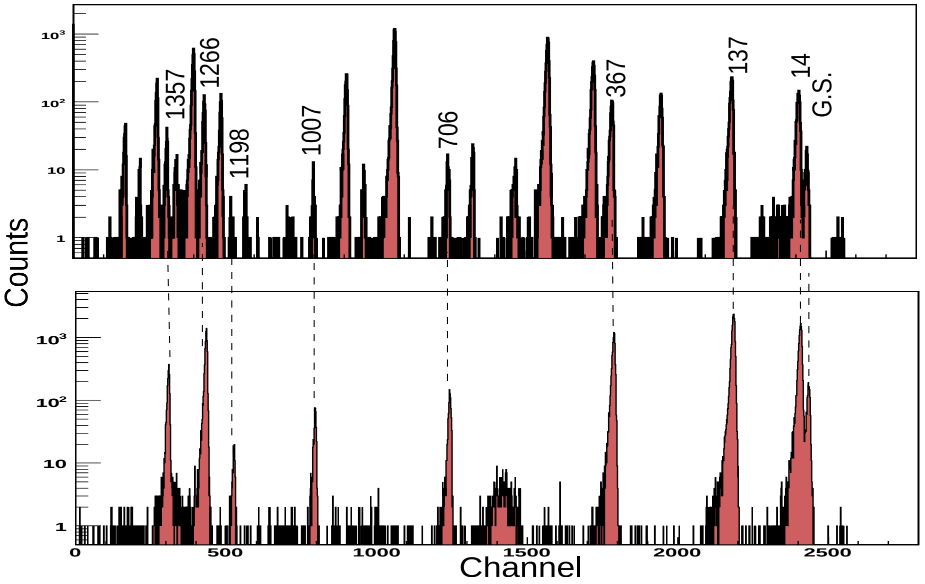

Figure 3.2.: Focal plane spectra of the Q3D observed at 30° with spin up polarized deuteron beam for ^{55}Fe + ^{57}Fe levels (top) compared to ^{57}Fe levels only (bottom) at $\mathrm{E_{Q3D}}$ setting centered at about 2200 keV.

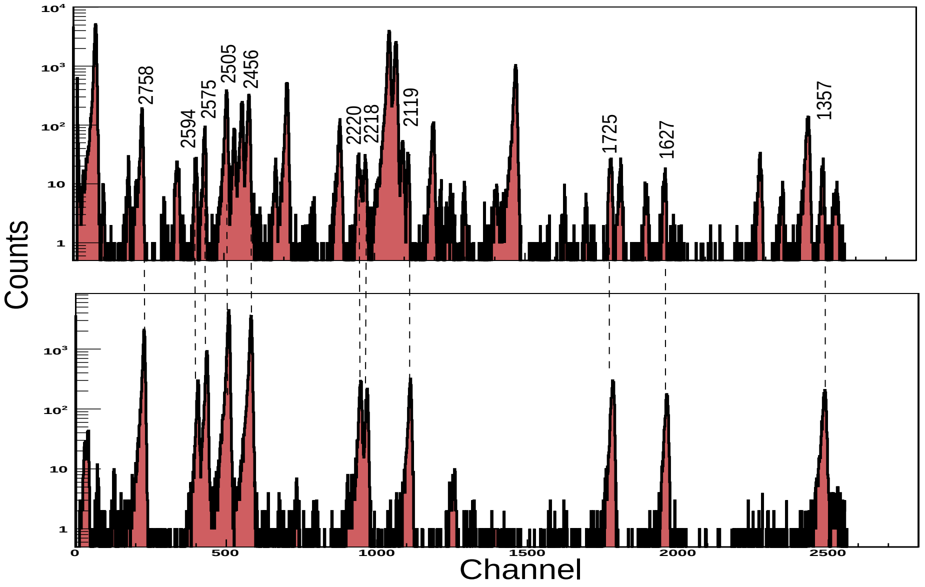

Figure 3.3.: Focal plane spectra of the Q3D observed at 30° with spin up polarized deuteron beam for ^{55}Fe + ^{57}Fe levels (top) compared to ^{57}Fe levels only (bottom) at $\mathrm{E_{Q3D}}$ setting centered at about 3550 keV. ^{57}Fe level energy values are from a beam time within this thesis frame work and in keV.

Perey and H. Feshbach sets have slightly better agreement for both the differential cross-section $\frac{d\sigma}{d\Omega}$ and the analyzing power A_{y}. This could be due to the systematic study through many nuclei, while T. Taylor & J. A. Cameron set is adjusted to fit the

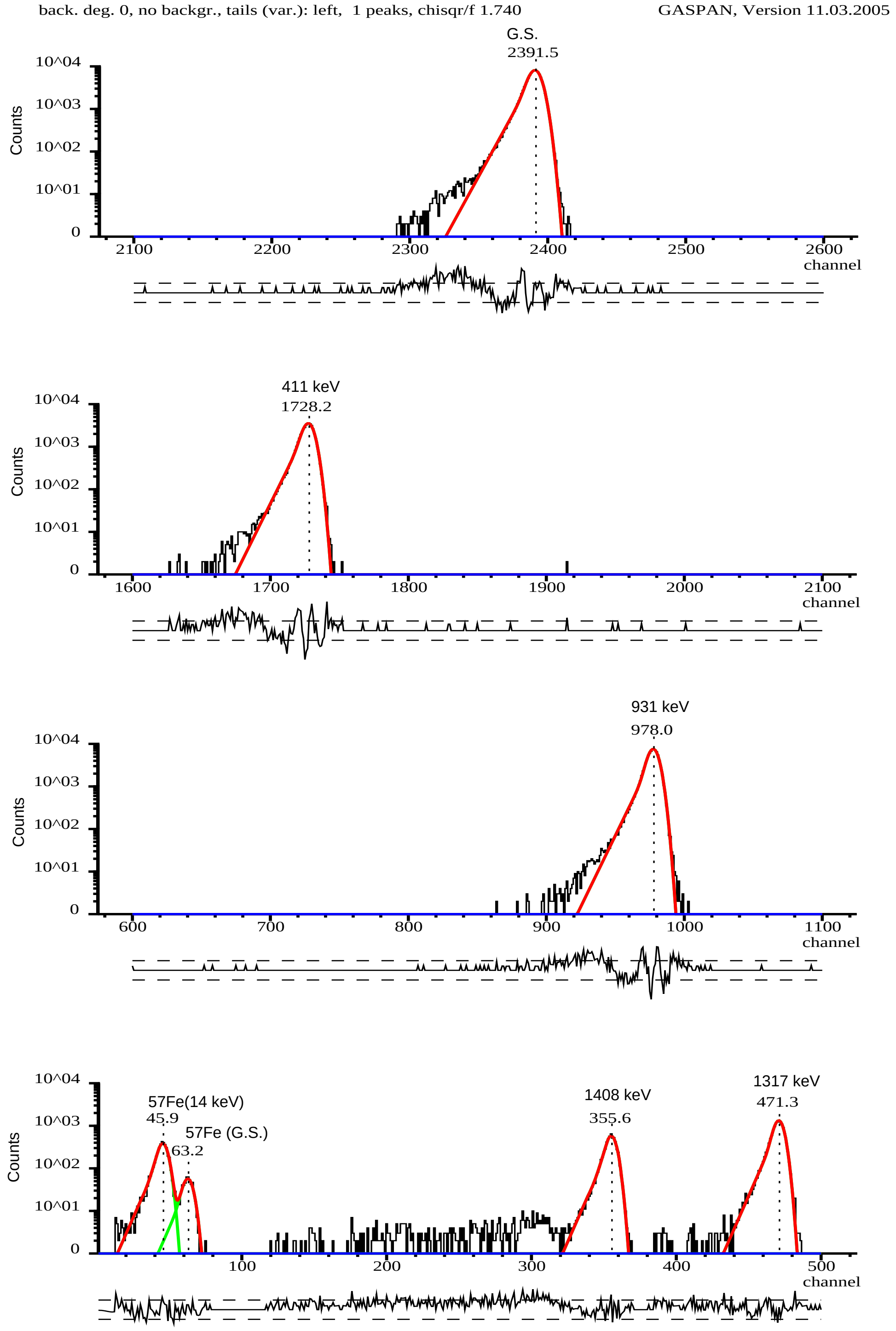

Figure 3.4.: Example for GASPAN fit for the Q3D focal plane spectrum. Q3D energy setting covering the range from 0.0 to 1700 keV, so that it was divided to 5 regions to obtain the best resolution. The background was fixed to zero. χ^2/N for the fit was around 1.7.

work on ^{54}Cr, ^{54,58}Fe and ^{58}Ni with $E_{\mathrm{Beam}} = 10$ MeV.

Potential		Real			Imaginary		
		V (MeV)	r_o (fm)	a_o (fm)	W (MeV)	r_I (fm)	a_I (fm)
Deuteron	Volume	-91.68	1.15	0.81			
	surface				17.76	1.34	0.68
	L.S	-6.92	1.07	0.66			
Proton	Volume	-53.16	1.17	0.75	-0.38	1.32	0.51
	surface				8.75	1.32	0.51
	L.S	-6.2	1.01	0.75			
Neutron	Volume	1.00	1.17	0.75			
	L.S	0.00	1.26	0.69			

Table 3.3.: Optical-Model parameters from C. M. Perey and F. G. Perey [32], V_{so} from Feshbach [6], for a beam energy of $E_{\mathrm{d}}^{\mathrm{lab}} = 14$ MeV.

Potential		Real			Imaginary		
		V (MeV)	r_o (fm)	a_o (fm)	W (MeV)	r_I (fm)	a_I (fm)
Deuteron	Volume	-92.64	1.05	0.86			
	surface				15.26	1.43	0.69
	L.S	-7.00	0.75	0.5			
Proton	Volume	-53.16	1.17	0.75	-0.38	1.32	0.51
	surface				8.75	1.32	0.51
	L.S	-6.2	1.01	0.75			
Neutron	Volume	1.00	1.17	0.75			
	L.S	0.00	1.26	0.69			

Table 3.4.: Optical-Model parameters from T. Taylor & J. A. Cameron [41], for a beam energy of $E_{\mathrm{d}}^{\mathrm{lab}} = 14$ MeV.

The non-locality parameter β for the particles mentioned in Table 3.6 is taken from J. H. Polane *et al.* [35]. The finite-range (R) parameters for the (d,p) reaction was set to zero since it was not used in ref: [41] and [19]. Including it in the calculations didn't significantly change the results.

Potential		Real			Imaginary		
		V (MeV)	r_o (fm)	a_o (fm)	W (MeV)	r_I (fm)	a_I (fm)
Deuteron	Volume	-90.91	1.17	0.73	-0.25	1.33	0.74
	surface				12.32	1.33	0.79
	L.S	-6.92	0.75	0.5			
Proton	Volume	-53.16	1.17	0.75	-0.38	1.32	0.51
	surface				8.74	1.32	0.51
	L.S	-6.2	1.01	0.75			
Neutron	Volume	1.00	1.17	0.75			
	L.S	0.00	1.26	0.69			

Table 3.5.: Optical-Model parameters from the Book: Theoretical Nuclear Physics, by Herman Feshbach [6], for a beam energy of $E_d^{lab} = 14$ MeV.

	Non-locality parameter p	Non-locality parameter d	Non-locality parameter n		Finite-range parameter (p,d)
β	0.85	0.54	0.85	R	0.0

Table 3.6.: DWBA parameters for Fe isotopes used in this work, from Polane *et al.* [35].

Spectroscopic factors S were determined by dividing the experimental cross-section $\sigma_{(\mathrm{Exp.})}$ by those obtained theoretically from DWBA calculations $\sigma_{(\mathrm{DWBA})}$, where S was set to 1 in the CHUCK3 code.

$$\sigma_{(\mathrm{Exp.})} = S * \sigma_{(\mathrm{DWBA})} \tag{3.5}$$

selecting the least χ^2/N value for S in dividing $\sigma_{(\mathrm{Exp.})}$ by $\sigma_{(\mathrm{DWBA})}$ over the angular range.

To avoid uncertainties arising in the calculations of the absolute cross-sections, spectroscopic factor values were also determined relative to the ground state spectroscopic factors. This step made our results easy to compare with the previous results from T. Taylor [41] and from Nuclear Data Sheets [19].

The average (Weighted Mean) of the normalized spectroscopic factors $S^{\mathrm{rel.}}_{\mathrm{Aver.}}$ of the three OM-parameters was obtained from the relation, ref [25]

$$S^{\mathrm{rel.}}_{\mathrm{Aver.}} = \frac{\Sigma S^{\mathrm{rel.}}_i/(\Delta S^{\mathrm{rel.}}_i)^2}{\Sigma 1/(\Delta S^{\mathrm{rel.}}_i)^2} \tag{3.6}$$

where $\Delta S^{\mathrm{rel.}}_i$ is the error in each normalized spectroscopic factor. The total error is calculated from the relation

$$\Delta S^{\mathrm{rel.}}_{\mathrm{Aver.}} = \sqrt{\frac{\sum(S^{\mathrm{rel.}}_i - S^{\mathrm{rel.}}_{\mathrm{Aver.}})^2}{n-1}} \tag{3.7}$$

where n is the number of the spectroscopic factors calculated from the different OM-parameters for each level, which was 3.

3.1.4. The Results

The experimental differential cross-sections $\frac{d\sigma}{d\Omega}$ and the experimental analyzing powers A_{y} were determined for ^{55}Fe levels up to an excitation energy of $\mathrm{E_x} = 4450$ keV. The results for each level were compared to the DWBA calculations utilizing the coupled-channel code CHUCK3 [23] using the three sets for the OM-potentials mentioned in Section 3.1.3. We can summarize some basic findings concerning our results:

- 39 levels of ^{55}Fe were observed in total in the energy range from 0.0 to 4450 keV.
- For 18 levels spin assignments were confirmed.
- For 4 levels with previously tentative spin assignment, spins were firmly established for the first time.
- For 4 levels were found to have other spin assignments.
- For 7 known levels spins were determined for the first time.
- 9 new levels at 2332, 2504, 3576, 3777, 3827, 4117, 4134, 4260 and 4292 keV were observed for the first time and spin assignments were made.
- Spectroscopic factors were determined for 25 levels for the first time.
- Besides that, we have strong evidence that five levels at 2015, 3285, 3860(10), 4123(10) and 4372(10) keV determined previously as ^{55}Fe levels, are rather the ^{57}Fe levels 367, 1627, 2220, 2456 and 2758 keV, respectively, Figures 3.2 & 3.3. All the published work observing those levels have considerable target contaminations and no work seems to have been done with γ-spectroscopy.

Concerning the last point, for example in the work using the reaction $^{54}\mathrm{Fe}(\mathrm{d},\mathrm{p})^{55}\mathrm{Fe}$ by Kocher *et al.* [19] a self supported target with 95% ^{54}Fe was used, which means the dominant ^{56}Fe isotope was also in the target and the reaction $^{56}\mathrm{Fe}(\mathrm{d},\mathrm{p})^{57}\mathrm{Fe}$ was also possible. The same situation is found with A. Sperduto *et al.* [40] with 2.34% ^{56}Fe and T. Taylor *et al.* [41] with 3.04% ^{56}Fe.

Also in the work using the reaction $^{56}\mathrm{Fe(d,t)}^{55}\mathrm{Fe}$ by M. H. Macfarlane *et al.* [29], they have target with 53% ^{58}Fe and 46% ^{56}Fe, which means the reaction $^{58}\mathrm{Fe(d,t)}^{57}\mathrm{Fe}$ is also possible and producing a significant amount of ^{57}Fe.
With thermal neutron capture (n,γ), for example J. Kopecky *et al.* [20] they used target with 93% ^{54}Fe and 6.8% ^{56}Fe, which means the reaction $^{56}\mathrm{Fe}(\mathrm{n},\gamma)^{57}\mathrm{Fe}$ can also happen to produce ^{57}Fe. Besides that, in none of the aforementioned publications a study of the reactions leading to ^{57}Fe has been presented, exept for A. Sperduto *et al.* [40], where they performed the reactions $^{54}\mathrm{Fe(d,p)}^{55}\mathrm{Fe}$ and $^{56}\mathrm{Fe(d,p)}^{57}\mathrm{Fe}$. The five ^{57}Fe levels 367, 1627, 2220, 2456 and 2721 keV were observed and the ^{55}Fe levels 3860, 4123 and 4372 keV but not 2015 and 3285 keV, which confirm our evidance for those two levels.

In general good agreement between the experimental results and DWBA calculations has been observed not only in the shapes of the angular distributions, but also for the analyzing powers. Also the average (Weighted Mean) of the normalized spectroscopic factors $S^{\mathrm{rel.}}_{\mathrm{Aver.}}$ from this work agree with the normalized spectroscopic factors $S^{\mathrm{rel.}}$ from Kocher *et al.* [19] for the 14 levels they measured.

Angular distributions for the cross-section and the analyzing power compared to the DWBA calculations for the levels are shown in Figures 3.5 → 3.13. Energies, spins and spectroscopic factors compared to the published data are shown in Tables 3.7 → 3.10.

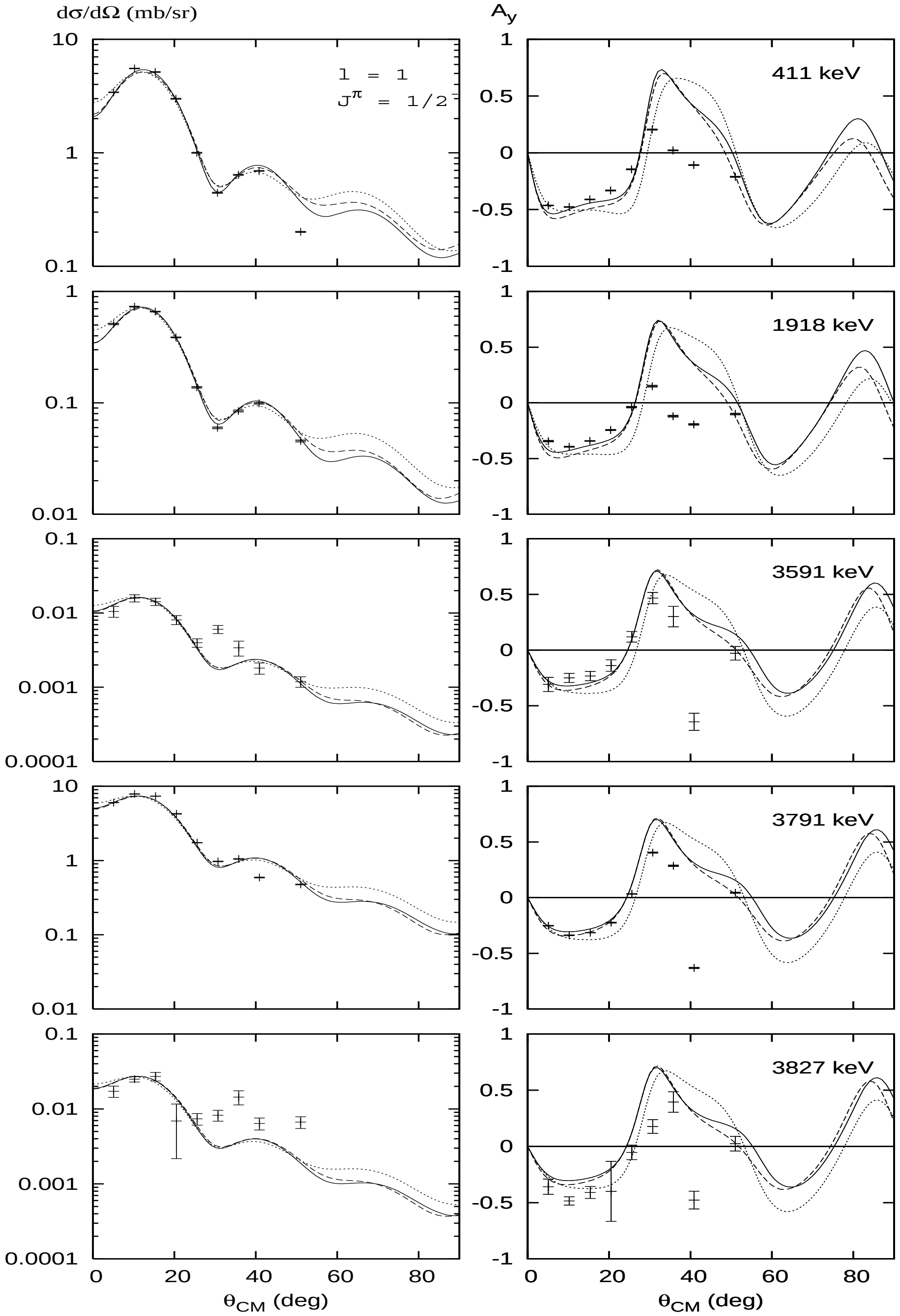

Figure 3.5.: Angular distributions for the differential cross-section $\frac{d\sigma}{d\Omega}$ and the analyzing power A_y for ^{55}Fe levels with $l = 1$ and $J^\pi = 1/2^-$. Curves indicate the DWBA calculations by CHUCK3 using the three different sets of OM-potentials, C. M. Perey and F. G. Perey [32] (Full curve), T. Taylor and J. A. Cameron [41] (dotted curve) and Herman Feshbach [6] (dashed curve).

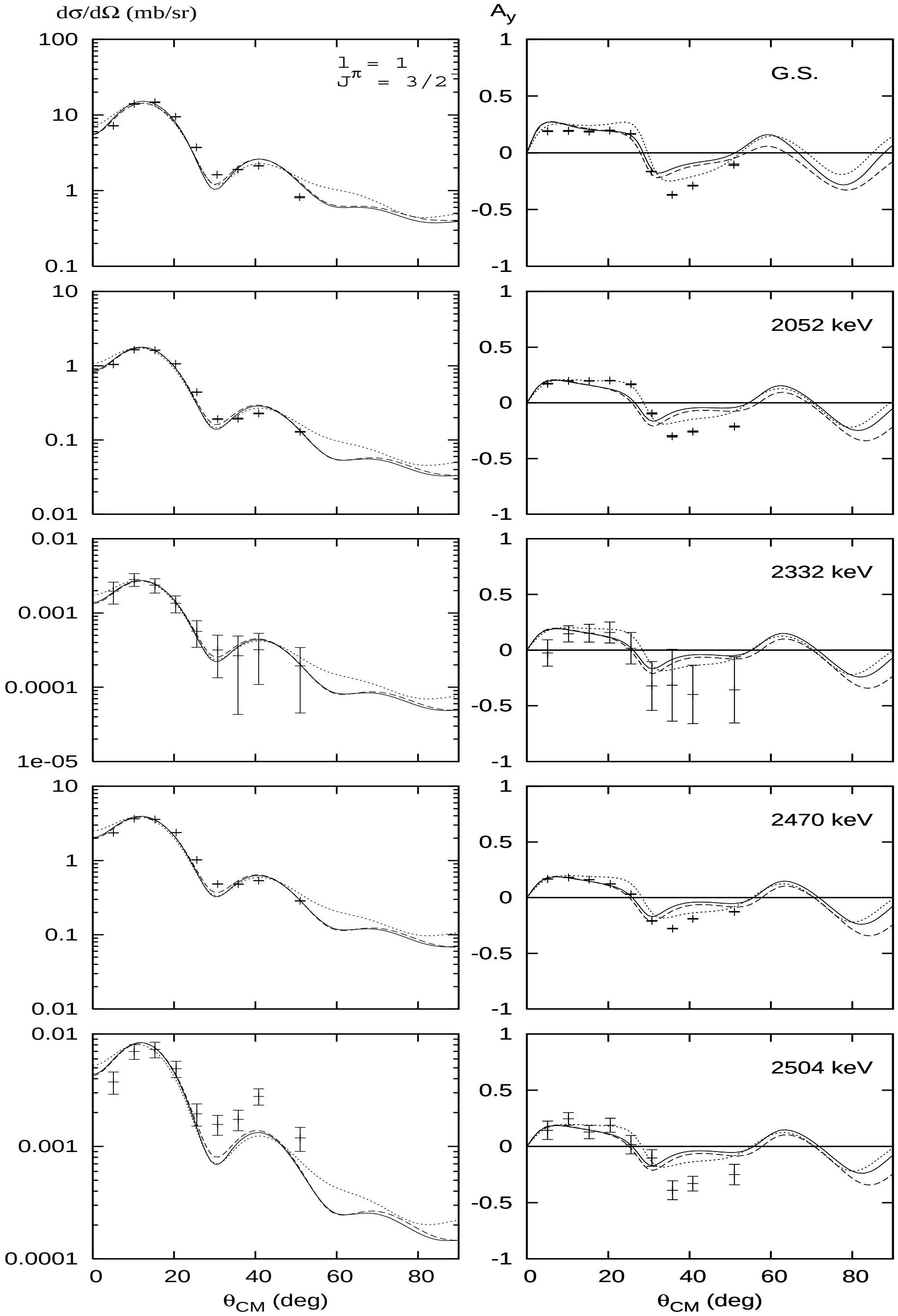

Figure 3.6.: Angular distributions for the differential cross-section $\frac{d\sigma}{d\Omega}$ and the analyzing power A_y for ^{55}Fe levels with $l = 1$ and $J^\pi = 3/2^-$. Curves indicate the DWBA calculations by CHUCK3 using the three different sets of OM-potentials, C. M. Perey and F. G. Perey [32] (Full curve), T. Taylor and J. A. Cameron [41] (dotted curve) and Herman Feshbach [6] (dashed curve).

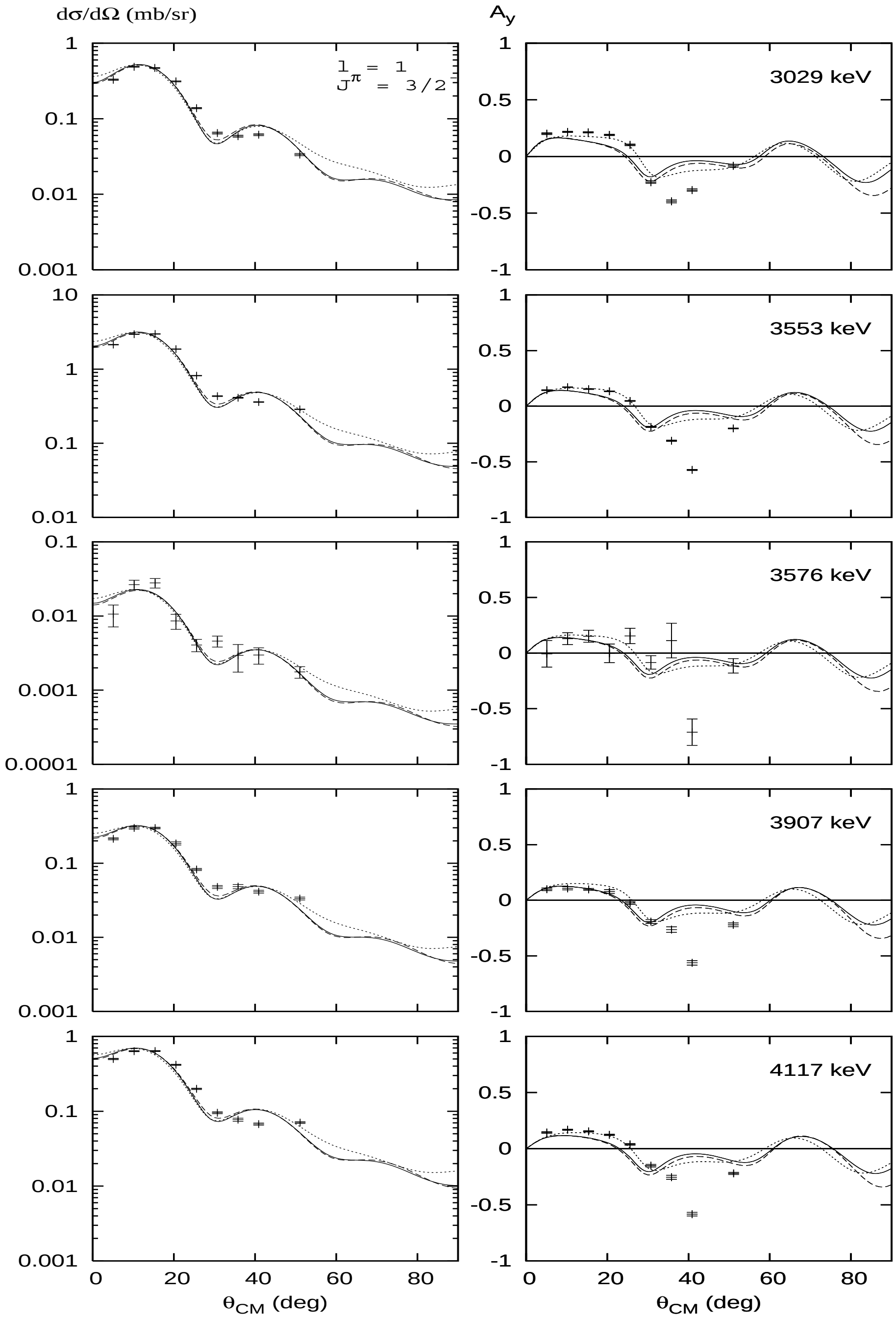

Figure 3.7.: Angular distributions for the differential cross-section $\frac{d\sigma}{d\Omega}$ and the analyzing power A_y for ^{55}Fe levels with $l = 1$ and $J^\pi = 3/2^-$. Curves indicate the DWBA calculations by CHUCK3 using the three different sets of OM-potentials, C. M. Perey and F. G. Perey [32] (Full curve), T. Taylor and J. A. Cameron [41] (dotted curve) and Herman Feshbach [6] (dashed curve).

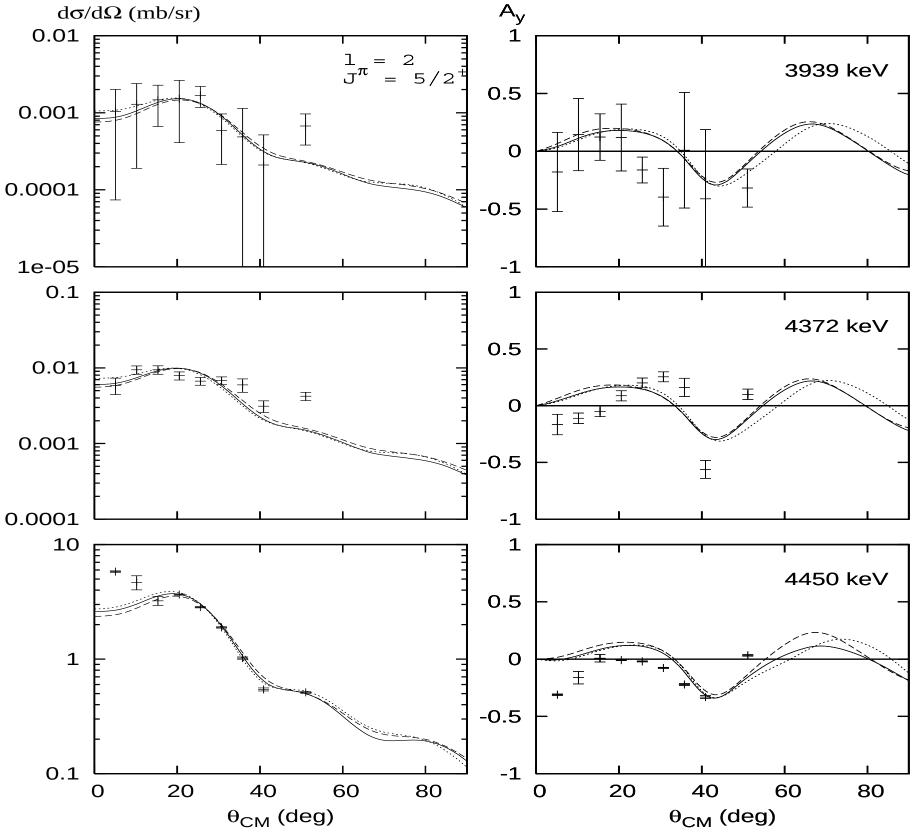

Figure 3.8.: Angular distributions for the differential cross-section $\frac{d\sigma}{d\Omega}$ and the analyzing power A_y for ^{55}Fe levels with $l = 2$ and $J^\pi = 5/2^+$. Curves indicate the DWBA calculations by CHUCK3 using the three different sets of OM-potentials, C. M. Perey and F. G. Perey [32] (Full curve), T. Taylor and J. A. Cameron [41] (dotted curve) and Herman Feshbach [6] (dashed curve)..

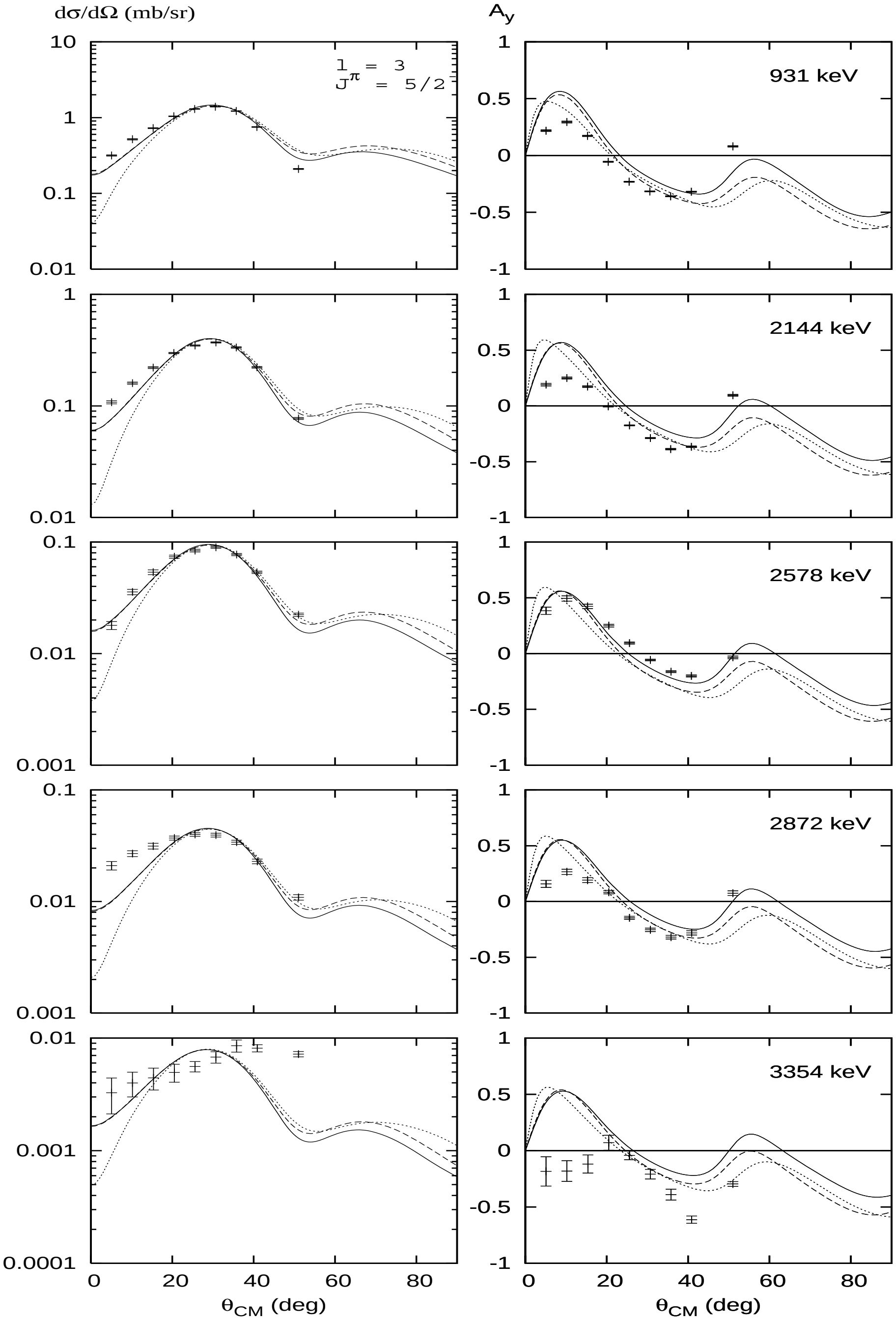

Figure 3.9.: Angular distributions for the differential cross-section $\frac{d\sigma}{d\Omega}$ and the analyzing power A_y for ^{55}Fe levels with $l = 3$ and $J^{\pi} = 5/2^{-}$. Curves indicate the DWBA calculations by CHUCK3 using the three different sets of OM-potentials, C. M. Perey and F. G. Perey [32] (Full curve), T. Taylor and J. A. Cameron [41] (dotted curve) and Herman Feshbach [6] (dashed curve).

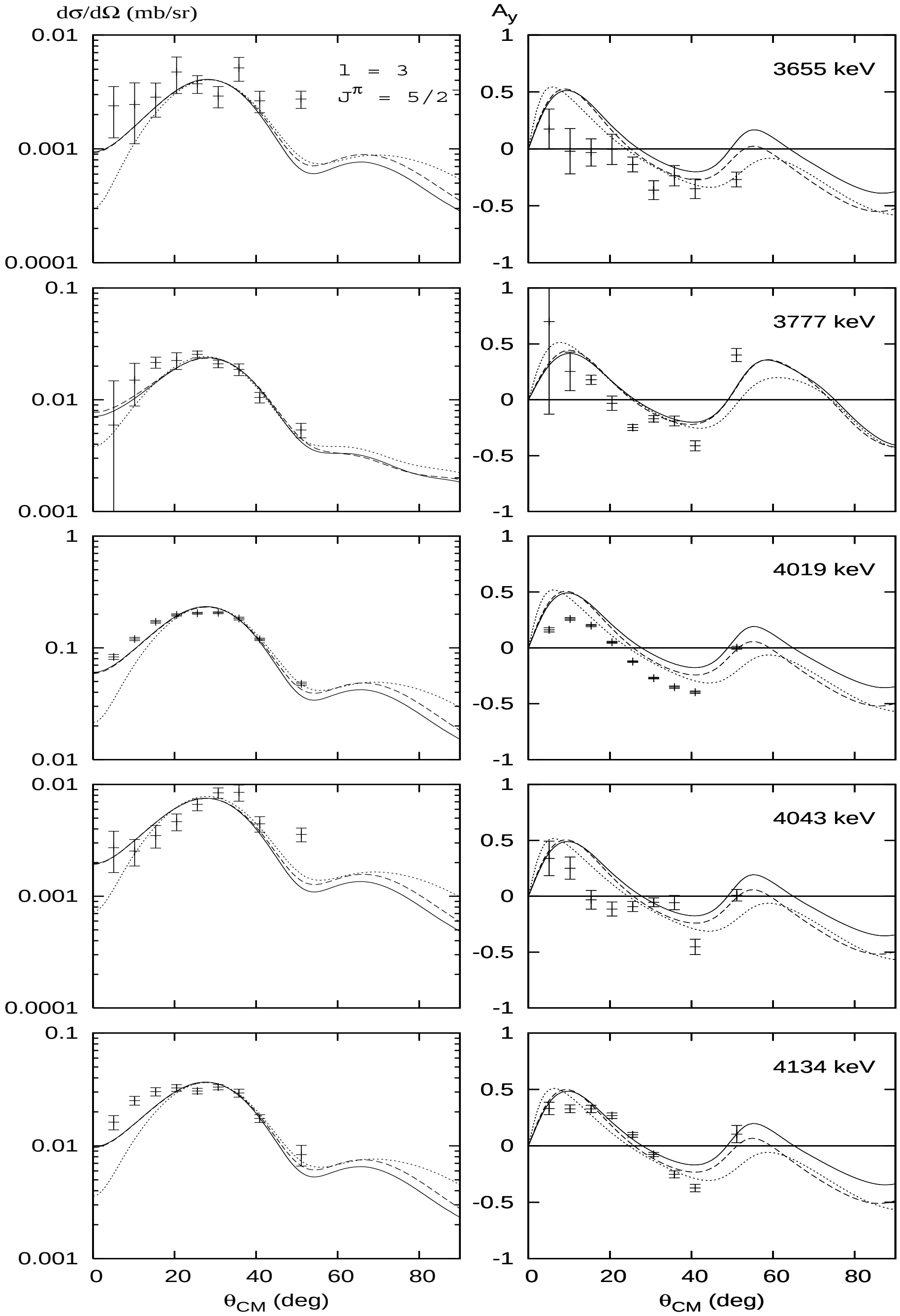

Figure 3.10.: Angular distributions for the differential cross-section $\frac{d\sigma}{d\Omega}$ and the analyzing power A_y for ^{55}Fe levels with $l = 3$ and $J^\pi = 5/2^-$. Curves indicate the DWBA calculations by CHUCK3 using the three different sets of OM-potentials, C. M. Perey and F. G. Perey [32] (Full curve), T. Taylor and J. A. Cameron [41] (dotted curve) and Herman Feshbach [6] (dashed curve).

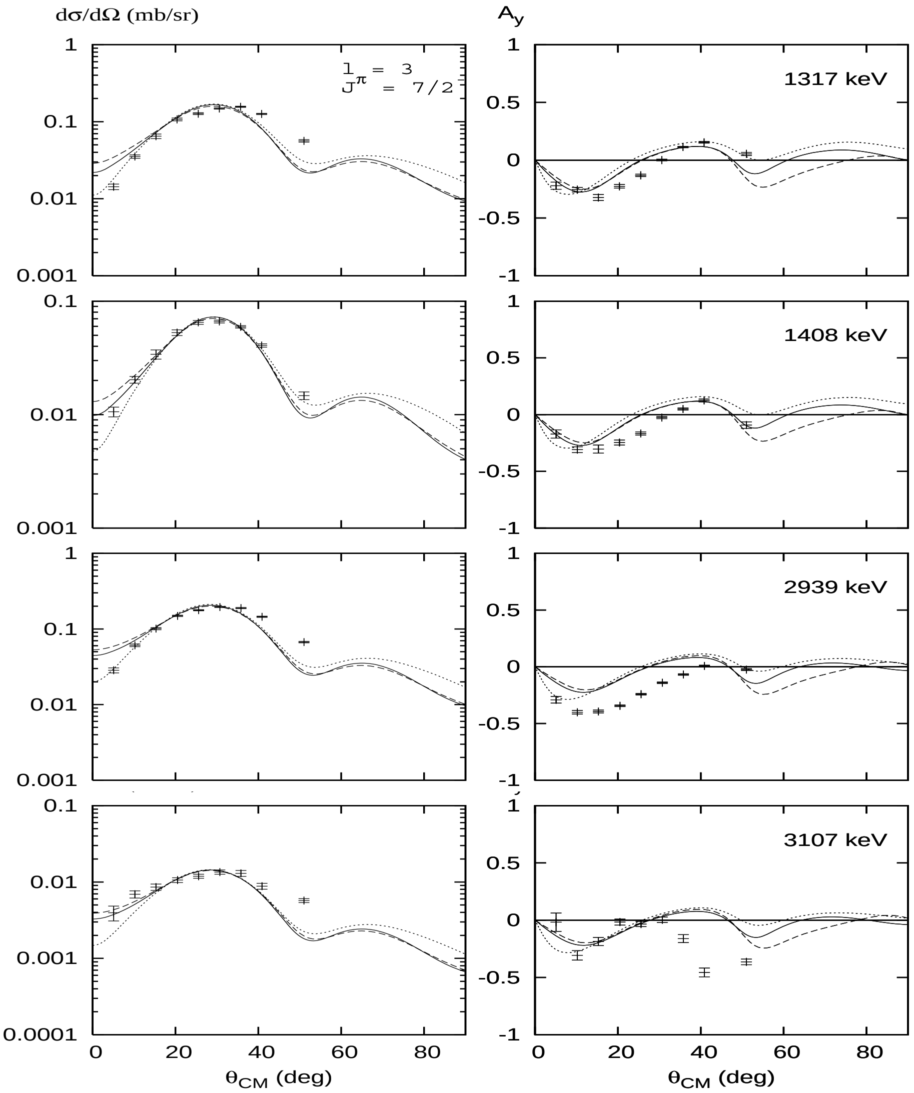

Figure 3.11.: Angular distributions for the differential cross-section $\frac{d\sigma}{d\Omega}$ and the analyzing power A_y for ^{55}Fe levels with $l = 3$ and $J^\pi = 7/2^-$. Curves indicate the DWBA calculations by CHUCK3 using the three different sets of OM-potentials, C. M. Perey and F. G. Perey [32] (Full curve), T. Taylor and J. A. Cameron [41] (dotted curve) and Herman Feshbach [6] (dashed curve).

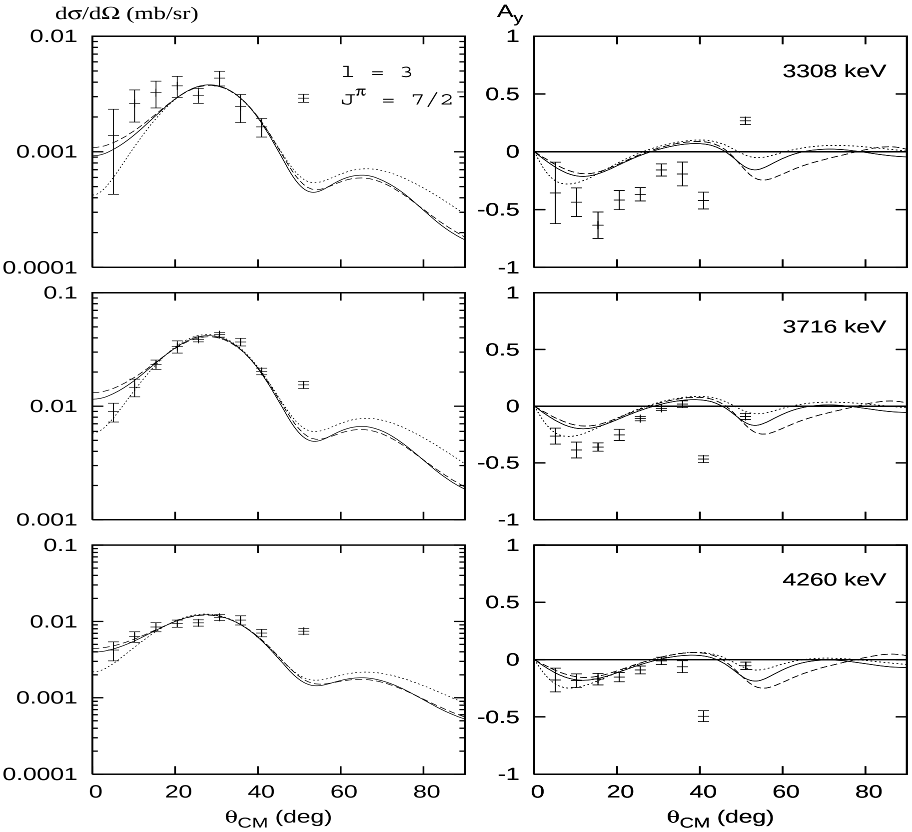

Figure 3.12.: Angular distributions for the differential cross-section $\frac{d\sigma}{d\Omega}$ and the analyzing power A_{y} for ^{55}Fe levels with $l = 3$ and $J^{\pi} = 7/2^{-}$. Curves indicate the DWBA calculations by CHUCK3 using the three different sets of OM-potentials, C. M. Perey and F. G. Perey [32] (Full curve), T. Taylor and J. A. Cameron [41] (dotted curve) and Herman Feshbach [6] (dashed curve).

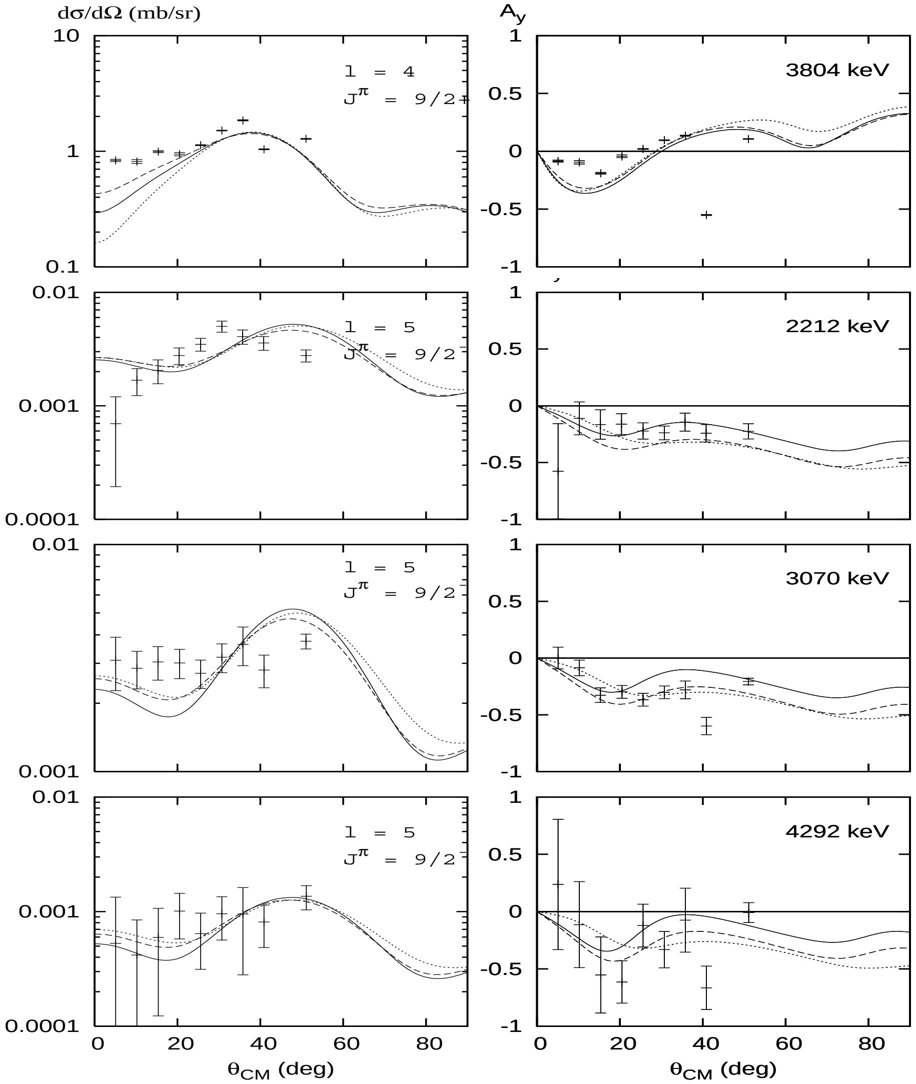

Figure 3.13.: Angular distributions for the differential cross-section $\frac{d\sigma}{d\Omega}$ and the analyzing power A_{y} for ^{55}Fe levels with $l = 4$ (top figure) and $l = 5$ (rest of the figures). Curves indicate the DWBA calculations by CHUCK3 using the three different sets of OM-potentials, C. M. Perey and F. G. Perey [32] (Full curve), T. Taylor and J. A. Cameron [41] (dotted curve) and Herman Feshbach [6] (dashed curve).

E_x (keV)	Δl	J^π	$J^\pi_\mathrm{Ref[19]}$	$(\frac{\mathrm{d}\sigma}{\mathrm{d}\Omega})^\mathrm{max}_\mathrm{mb/sr}$ θ_max	S_Perey	S_Taylor	S_Feshbach	$S_\mathrm{Aver.}$	$S^\mathrm{rel.}_\mathrm{Aver.}$	$S^\mathrm{rel.}_\mathrm{Ref[41]}$	$S^\mathrm{rel.}_\mathrm{Ref[19]}$
0.0	1	$\frac{3}{2}^-$	$\frac{3}{2}^-$	14.67(2) 15.3	0.506(2)	0.486(2)	0.485(2)	0.49(1)	1.000(0)	1.000	1.000
411.05(0.13)	1	$\frac{1}{2}^-$	$\frac{1}{2}^-$	5.53(5) 10.2	0.366(1)	0.353(1)	0.344(1)	0.35(1)	0.72(1)	0.522	0.808
931.41(0.12)	3	$\frac{5}{2}^-$	$\frac{5}{2}^-$	1.39(1) 30.6	0.449(2)	0.421(2)	0.416(2)	0.43(2)	0.87(2)	0.6087	0.945
1316.54(0.12)	3	$\frac{7}{2}^-$	$\frac{7}{2}^-$	0.156(3) 35.7	0.0287(3)	0.0272(3)	0.0285(3)	0.0281(8)	0.057(1)	0.0652	0.068
1408.21(0.15)	3	$\frac{7}{2}^-$	$\frac{7}{2}^-$	0.066(2) 30.6	0.0124(2)	0.0115(2)	0.0125(2)	0.0121(5)	0.025(1)	0.0261	0.0226

Table 3.7.: Table showing ^{55}Fe levels from $^{54}\mathrm{Fe}(\vec{\mathrm{d}},\mathrm{p})^{55}\mathrm{Fe}$ reaction, transferred angular momentum Δl, total angular momentum J^π from this work compared to J^π from nuclear data sheets ref. [19], maximum cross-section and its position, spectroscopic factors S from the three different OM-parameters sets, $S_\mathrm{Aver.}$ the weighted average of those spectroscopic factors, the normalized to the G.S. average $S^\mathrm{rel.}_\mathrm{Aver.}$ compared to the published values.

S_Perey: S is deduced using OM-parameters for DWBA calculations from C. M. Perey and F. G. Perey [32],

S_Taylor: S is deduced using OM-parameters for DWBA calculations from T. Taylor and J. Cameron [41]

S_Feshbach: S is deduced using OM-parameters for DWBA calculations from H. Feshbach [6].

E_x (keV)	Δl	J^π	$J^\pi_{\mathrm{Ref[19]}}$	$(\frac{d\sigma}{d\Omega})^{\mathrm{max}}_{\mathrm{mb/sr}}$ θ_{max}	S_{Perey}	S_{Taylor}	S_{Feshbach}	$S_{\mathrm{Aver.}}$	$S^{\mathrm{rel.}}_{\mathrm{Aver.}}$	$S^{\mathrm{rel.}}_{\mathrm{Ref[41]}}$	$S^{\mathrm{rel.}}_{\mathrm{Ref[19]}}$
1918.08(0.09)	1	$\frac{1}{2}^-$	$\frac{1}{2}^-$	0.731(7) 10.2	0.0403(2)	0.0400(2)	0.0396(2)	0.0400(3)	0.081(2)	0.0695	0.096
2050.12(0.05)	1	$\frac{3}{2}^-$	$\frac{3}{2}^-$	1.641(12) 10.2	0.0458(2)	0.0454(2)	0.0468(2)	0.046(1)	0.093(3)	0.113	0.109
2144.03(0.06)	3	$\frac{5}{2}^-$	$\frac{5}{2}^-$	0.371(4) 30.7	0.1050(6)	0.0975(6)	0.1010(6)	0.101(4)	0.205(4)	0.1709	0.219
2211.53(0.22)	(5)	$(\frac{9}{2}^-)$	$\frac{9}{2}^-$	0.005(1) 30.7	0.0040(2)	0.0031(2)	0.0030(2)	0.0032(6)	0.0066(9)		
2332.17(0.76)*	1	$\frac{3}{2}^-$		0.003(1) 10.2	0.00007(1)	0.00007(1)	0.00007(1)	0.000068(1)	0.00014(1)		
2470.19(0.06)	1	$\frac{3}{2}^-$	$\frac{3}{2}^-$	3.653(20) 10.2	0.0959(2)	0.0950(2)	0.0979(2)	0.0963(2)	0.196(6)	0.1696	0.205
2503.75(0.43)*	1	$\frac{3}{2}^-$		0.007(1) 15.3	0.00020(1)	0.00020(1)	0.0002(1)	0.00020(1)	0.00041(2)		
2579.21(0.07)	3	$\frac{5}{2}^-$	$\frac{5}{2}^-$	0.090(2) 30.7	0.0233(3)	0.0214(2)	0.0226(2)	0.0224(9)	0.046(1)	–	0.068
2872.43(0.08)	3	$\frac{5}{2}^-$	$\frac{5}{2}^-,\frac{7}{2}^-$	0.040(2) 25.6	0.0106(2)	0.0096(2)	0.0103(2)	0.0102(5)	0.0207(8)		
2938.75(0.06)	3	$\frac{7}{2}^-$	$\frac{7}{2}^-$	0.195(3) 30.7	0.0280(2)	0.0276(2)	0.0285(2)	0.0280(5)	0.057(2)		
3028.22(0.07)	1	$\frac{3}{2}^-$	$\frac{3}{2}^-$	0.487(7) 10.2	0.0118(1)	0.0118(1)	0.0121(1)	0.0119(2)	0.0241(8)		
3070.23(0.32)	5	$\frac{9}{2}^-$	3072.0(4), $\frac{11}{2}^-$	0.0038(3) 51.0	0.0038(2)	0.0029(2)	0.0030(2)	0.0031(5)	0.0064(9)		

Table 3.8.: ^{55}Fe Excitation levels from $^{54}\mathrm{Fe}(\vec{\mathrm{d}},\mathrm{p})^{55}\mathrm{Fe}$ reaction, Q3D magnetic settings centered at excitation energy of 2200 keV.

* New ^{55}Fe levels.

E_x (keV)	Δl	J^π	$E_\mathrm{x}, J^\pi_\mathrm{Ref[19]}$	$(\frac{\mathrm{d}\sigma}{\mathrm{d}\Omega})^\mathrm{max}_\mathrm{mb/sr}$ θ_max	S_Perey	S_Taylor	S_Feshbach	$S_\mathrm{Aver.}$	$S^\mathrm{rel.}_\mathrm{Aver.}$	$S^\mathrm{rel.}_\mathrm{Ref[41]}$	$S^\mathrm{rel.}_\mathrm{Ref[19]}$
3107.18(0.14)	3	$\frac{7}{2}^-$	3108(1)$\frac{5}{2}^-$,$\frac{7}{2}^-$	0.013(1) 30.7	0.0020(1)	0.0019(1)	0.0021(1)	0.0020(1)	0.0041(2)		
3307.99(0.29)	3	$\frac{7}{2}^-$	3311(10)$\frac{5}{2}^-$,$\frac{7}{2}^-$	0.004(1) 30.7	0.00048(4)	0.00047(4)	0.00050(5)	0.00048(2)	0.00098(4)		
3354.43(0.17)	3	$\frac{5}{2}^-$	3362(10),NoJ^π	0.009(1) 35.8	0.0017(1)	0.0016(1)	0.0017(1)	0.0017(1)	0.0034(1)		
3553.37(0.44)	1	$\frac{3}{2}^-$	$\frac{3}{2}^-$	2.982(25) 15.4	0.0665(2)	0.0669(2)	0.0680(2)	0.0671(1)	0.1363(3)	0.148	0.15
3576.24(0.37)*	1	$\frac{3}{2}^-$		0.028(4) 15.4	0.00047(4)	0.00048(4)	0.00049(4)	0.00048(2)	0.00097(4)		
3591.18(0.22)	1	$\frac{1}{2}^-$	3599(10),$\frac{1}{2}^-$	0.016(2) 10.2	0.00072(4)	0.00072(4)	0.00073(4)	0.00072(2)	0.00147(4)		
3654.66(0.24)	3	$\frac{5}{2}^-$	3660(11),NoJ^π	0.005(1) 35.8	0.0008(1)	0.0008(1)	0.0008(1)	0.00080(5)	0.0016(1)		
3715.56(0.1)	3	$\frac{7}{2}^-$	3722(10),NoJ^π	0.043(2) 30.7	0.0049(1)	0.0049(1)	0.0050(1)	0.0050(1)	0.0101(2)		
3776.78(0.47)*	3	$\frac{5}{2}^-$		0.025(2) 25.6	0.0015(1)	0.0016(1)	0.0016(1)	0.00155(4)	0.0031(1)		
3790.57(0.47)	1	$\frac{1}{2}^-$	3790(8), $\frac{1}{2}^-$	7.87(6) 10.2	0.319(1)	0.319(1)	0.325(1)	0.3208(6)	0.651(1)	–	0.68
3803.96(0.47)	4	$\frac{9}{2}^+$	3814(10),$\frac{7}{2}^+$,$\frac{9}{2}^+$	1.85(2) 35.8	0.273(1)	0.301(1)	0.255(1)	0.2734(7)	0.555(2)		
3826.53(0.56)*	1	$\frac{1}{2}^-$		0.027(4) 15.4	0.0012(1)	0.0011(1)	0.0012(1)	0.00117(3)	0.0024(1)		

Table 3.9.: ^{55}Fe Excitation levels from ^{54}Fe($\vec{\mathrm{d}}$, p)^{55}Fe reaction, Q3D magnetic settings centered at excitation energy of 3600 keV.

* New ^{55}Fe levels.

E_x (keV)	Δl	J^π	$E_\mathrm{x}, J^\pi_{\mathrm{Ref[19]}}$	$(\frac{\mathrm{d}\sigma}{\mathrm{d}\Omega})^{\mathrm{max}}_{\mathrm{mb/sr}}$ θ_{max}	S_{Perey}	S_{Taylor}	S_{Feshbach}	$S_{\mathrm{Aver.}}$	$S^{\mathrm{rel.}}_{\mathrm{Aver.}}$	$S^{\mathrm{rel.}}_{\mathrm{Ref[41]}}$	$S^{\mathrm{rel.}}_{\mathrm{Ref[19]}}$
3906.81(0.48)	1	$\frac{3}{2}^-$	3907(8),$\frac{3}{2}^-$	0.299(11) 10.2	0.0064(1)	0.0064(1)	0.0066(1)	0.0065(1)	0.0132(5)		
3939.18(0.65)	2	$\frac{5}{2}^+$	3960(10),NoJ^π	0.002(1) 25.6	0.00004(1)	0.00004(1)	0.00003(1)	0.000036(3)	0.00007(1)		
4018.92(0.49)	3	$\frac{5}{2}^-$	4028(10),NoJ^π	0.206(4) 30.7	0.0442(4)	0.0410(4)	0.0443(4)	0.043(2)	0.088(4)	–	0.082
4043.18(0.55)	3	$\frac{5}{2}^-$	4057(10),$\frac{5}{2}^-$,$\frac{7}{2}^-$	0.009(1) 35.8	0.0014(1)	0.0014(1)	0.0014(1)	0.00140(3)	0.0029(1)		
4116.95(0.5)*	1	$\frac{3}{2}^-$	4123(10),NoJ^π	0.636(9) 15.4	0.0135(1)	0.0136(1)	0.0139(1)	0.0137(2)	0.028(1)		
4133.74(0.51)*	3	$\frac{5}{2}^-$		0.033(2) 30.7	0.0068(2)	0.0063(2)	0.0068(2)	0.0066(3)	0.0134(6)		
4259.81(0.54)*	3	$\frac{7}{2}^-$	4273(10),$\frac{1}{2}^+$	0.011(1) 30.7	0.0013(1)	0.0013(1)	0.0013(1)	0.00130(2)	0.0026(1)		
4291.93(1.13)*	5	$\frac{9}{2}^-$		0.0014(3) 51.1	0.0009(1)	0.0007(1)	0.0008(1)	0.0008(1)	0.0016(2)		
4371.56(0.55)	2	$(\frac{5}{2}^+)$	4387(10),NoJ^π	0.009(1) 15.4	0.00021(1)	0.00023(1)	0.00021(1)	0.00022(1)	0.00044(3)		
4449.95(0.1)	2	$\frac{5}{2}^+$	$\frac{5}{2}^+$	5.80(9) 5.1	0.233(1)	0.268(2)	0.225(1)	0.24(2)	0.49(5)	–	0.178

Table 3.10.: ^{55}Fe Excitation levels from ^{54}Fe($\vec{\mathrm{d}}$, p)^{55}Fe reaction, Q3D magnetic settings centered at excitation energy of 3600 keV.

* New ^{55}Fe levels.

3.1.5. Discussion

Most of the differential reaction cross-section $\frac{d\sigma}{d\Omega}$ and analyzing powers A_{y} for the observed ^{55}Fe levels exhibit the characteristic l dependent pattern predicted by the one-step transfer reaction from the DWBA calculations. Few levels (ex: 3070, 4292 keV) show rather flat and featureless shape. A common property of the levels showing such a behavior is that they are weakly excited. Therefore in these cases two-step processes are generally thought to be competing with the one-step process. Generally, the average of the normalized spectroscopic factors $S^{\mathrm{rel.}}_{\mathrm{Aver.}}$ calculated in this work agree with the known $S^{\mathrm{rel.}}$ from D.C. Kocher [19] and T. Taylor [41], presented in the Tables 3.7 → 3.10. Few levels show new behavior or contrary to the expected. Such levels will be discussed briefly in this section.

The 2211 keV level ($\frac{9}{2}^{-?}$)

The 2211 keV level (2212 keV in ref: [7]) is assigned in a previous work by H. J. Fischbeck [7] as $J^{\pi} = \frac{9}{2}^{-}$, based on the 804 keV γ-transition to the $\frac{7}{2}^{+}$ level at 1408 keV, which is the only transition observed from the 2211 keV level.
First, we considered it as a simple direct transition from ^{54}Fe 0^{+} ground state to ^{55}Fe $\frac{9}{2}^{-}$ 2211 keV and compare the DWBA calculations with the experimental results. A disagreement in the differential cross-sections $\frac{d\sigma}{d\Omega}$ and agreement in the analyzing powers A_{y} curves were observed, Figure 3.15 (top). The other parity $J^{\pi} = \frac{9}{2}^{+}$ was considered for this level, but the situation is just reversed, good agreement in the $\frac{d\sigma}{d\Omega}$ and disagreement in the A_{y} were observed, Figure 3.15 (middle).
Finally we consider a Coupled Channel (CC) scheme consisting of three routes, Figure 3.14
- Transition from ^{54}Fe G.S. to ^{55}Fe 2211 keV via ^{54}Fe 2^{+} level at 1408 keV.
- Transition from ^{54}Fe G.S. to ^{55}Fe 2211 keV via ^{55}Fe $\frac{5}{2}^{-}$ level at 931 keV.
- The direct transition from ^{54}Fe G.S. to ^{55}Fe 2211 keV.

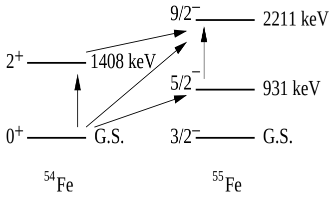

Figure 3.14.: The three coupled channel (CC) routes suggested for the 2211 keV level through ^{54}Fe 2^{+} level at 1408 keV, ^{55}Fe $\frac{5}{2}^{-}$ level at 931 keV and the direct transition.

Unfortunately, the disagreement between the experimental and the theoretical angular distributions is still observed, Figure 3.15 (bottom). It could be due to other intermediate steps that should be included in the calculations. In any case, due to the evidence from the γ-spectroscopy by Fischbeck *et al.* [7], the assignment of this level as $\frac{9}{2}^{-}$ seems firm.

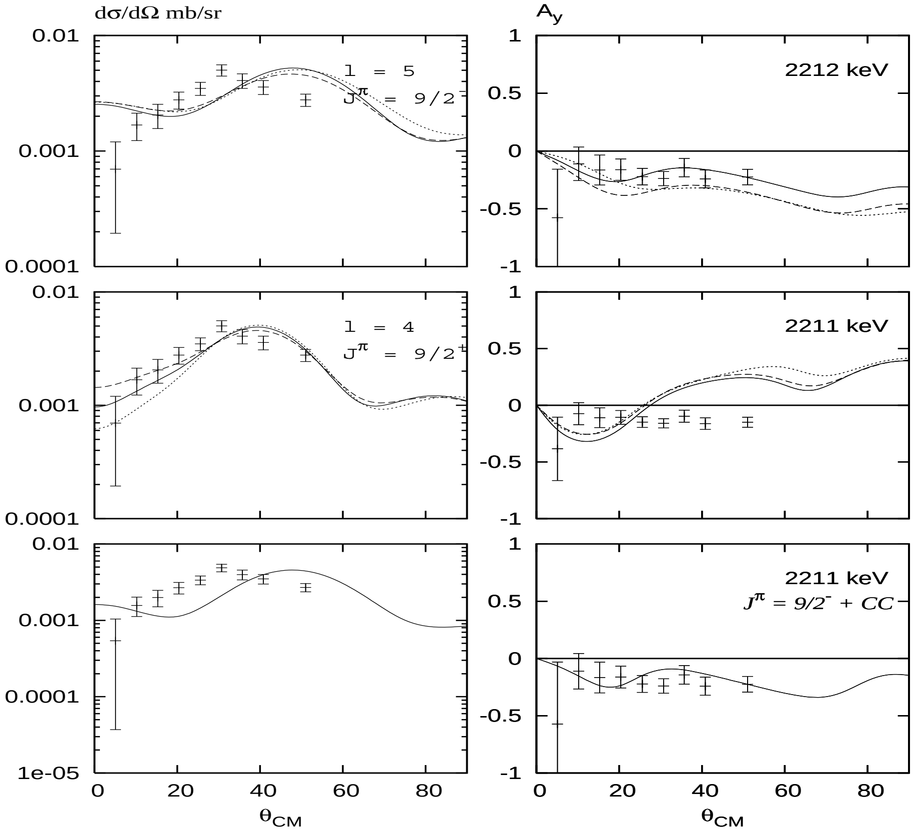

Figure 3.15.: Angular distributions for the 2211 keV level considering its $J^\pi = \frac{9}{2}^-$ (top), $J^\pi = \frac{9}{2}^+$ (middle), $J^\pi = \frac{9}{2}^-$ through 2^+ excitation at 1408 keV in ^{54}Fe and $\frac{5}{2}^+$ excitation at 931 keV in ^{55}Fe (bottom), using the OM-potential set from C. M. Perey and F. G. Perey [32] (Full curve).

The 2872, 4043 keV levels ($\frac{5}{2}^-$)

The 2872, 4043 (4057 ±10) keV levels are assigned in the nuclear data sheets by H. Junde [18] as $\frac{5}{2}^-$ or $\frac{7}{2}^-$. By comparing the shapes of ($\frac{d\sigma}{d\Omega}$) and (A_y) to DWBA calculation, Figures 3.9 and 3.10, it is clear they have $l = 3$ transfer and $J^\pi = \frac{5}{2}^-$.

The 3070 level ($\frac{9}{2}^-$)

3070 keV is assigned previously as $\frac{11}{2}^-$ but after comparing the experimental A_y with the DWBA calculations for the two cases $J^\pi = \frac{9}{2}^-$ and $\frac{11}{2}^-$, the first assignment seems to be more realistic, Figure 3.16. However, one should keep in mind its low reaction cross-section $(\frac{\mathrm{d}\sigma}{\mathrm{d}\Omega})^{\max} = 0.004$ mb/sr which could also make a two-step process possible.

The 3308 level ($\frac{7}{2}^-$)

3308 (3311 ±10) keV level was listed previously with two possible spin values $\frac{5}{2}^-$ or $\frac{7}{2}^-$ but from Figure 3.12, we are sure it is $l = 3$ transfer and has $J^\pi = \frac{7}{2}^-$.

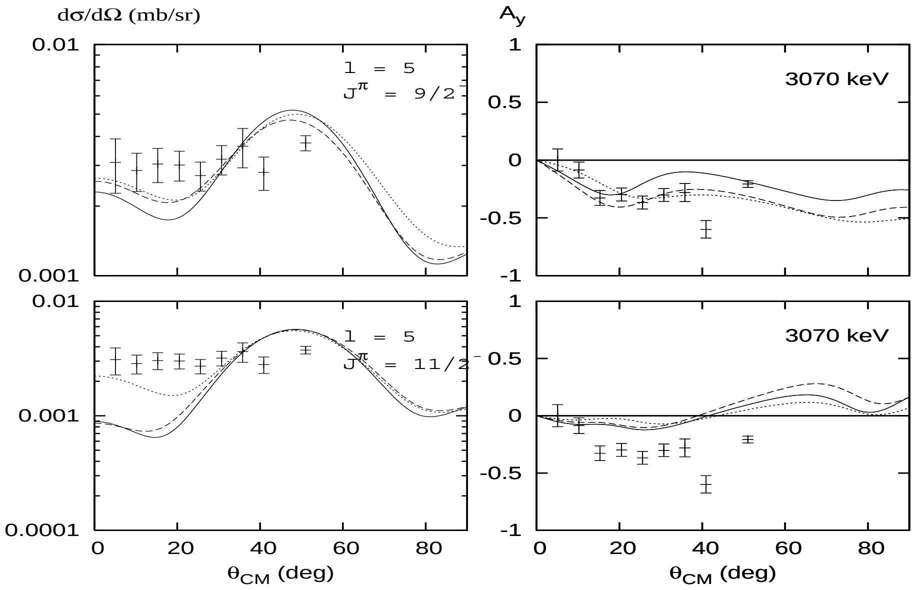

Figure 3.16.: Experimental results for the 3070 keV level compared to DWBA calculations considering it $\frac{9}{2}^-$ top and $\frac{11}{2}^-$ bottom.

The 3804 level ($\frac{9}{2}^+$)

3804 keV is assigned previously with two possible spin values $\frac{7}{2}^+$ or $\frac{9}{2}^+$ (3814 ±10 keV) but by comparing our experimental A_y with the DWBA calculations we are sure it is $\frac{9}{2}^+$, Figure 3.13.

The 4260 keV level ($\frac{7}{2}^-$)

Also 4260 keV is assigned as $\frac{1}{2}^+$ (4273 ±10 keV) but from Figure 3.12, we are sure it is $l = 3$ transfer and has $J^\pi = \frac{7}{2}^-$.

3.1.6. Interpretation

The results obtained from the $^{54}\mathrm{Fe}(\vec{\mathrm{d}},\mathrm{p})^{55}\mathrm{Fe}$ reaction provide an excellent test for the stability of the N = 28 shell closure. The $^{54}_{26}\mathrm{Fe}_{28}$ nucleus has Z = 26 and N = 28. Under the assumption that N = 28 is a good neutron shell closure, with a simple approach it could be considered as a core of the good doubly magic nucleus $^{48}_{20}\mathrm{Ca}_{28}$ plus 6 protons in the $1f_{7/2}$ shell. By transferring one neutron to the $^{54}_{26}\mathrm{Fe}_{28}$ via the (d,p) reaction, the additional neutron should occupy any shell higher than the closed $1f_{7/2}$ and no levels with $J^\pi = \frac{7}{2}^-$ should be observed or only at very high excitation energy, enough to break the closed $1f_{7/2}$ shell, see top part of Figure 3.17.

In contradiction to this simple expectation 8 levels with $J^\pi = \frac{7}{2}^-$ were observed in the current work, three of them are the previously well known levels 1316, 1408 and 2938 keV, which exist at low energy. This means the $^{54}_{26}\mathrm{Fe}_{28}$ ground state wave function does not have a pure closed $1f_{7/2}$ shell configuration $(f_{7/2})^8$ for the neutrons, but a considerable fraction of it has two particle two hole configuration (cross shell excitation), see bottom part of Figure 3.17, and the transferred neutron occupied one of the $1f_{7/2}$ holes, resulting in a single particle configuration in the $1f_{7/2}$ shell. So that the spin $J^{\pi} = \frac{7}{2}^{-}$ is observed.

This interpretation is expected from the previous study by M. Honma and T. Otsuka *et al.* [17]. Our precision data allow for a comparison with modern shell model calculations and to obtain information on how many particles have to be excited across the shell to obtain good agreement with the data.

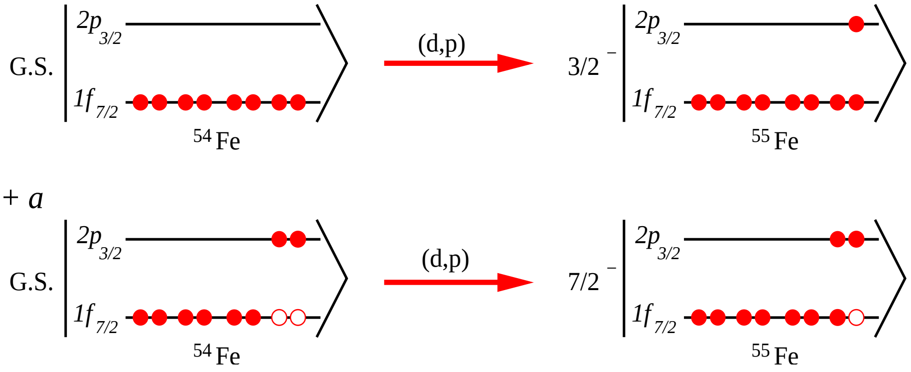

Figure 3.17.: Top part: If the $^{54}_{26}$Fe$_{28}$ G.S. wave function has a strongly closed $1f_{7/2}$ shell for neutrons, the additional neutron after the (d,p) reaction should occupy any higher shell not the $1f_{7/2}$.
Bottom part: But if the $^{54}_{26}$Fe$_{28}$ ground state wave function has a cross shell excitation the additional neutron could occupy one of the $1f_{7/2}$ gaps, resulting in levels with $J^{\pi} = \frac{7}{2}^{-}$.

To confirm this conclusion, additional large scale shell model calculations have been performed by A. Lisetskiy, using the ANTOINE code [5] and GXPF1 effective interaction from M. Honma and T. Otsuka *et al.* [17], once considering

- The ^{54}Fe G.S. wave function has strong closed $1f_{7/2}$, no free nucleons (n = 0).

And once else considering

- The ^{54}Fe G.S. wave function has a broken $1f_{7/2}$ shell and up to 6 nucleons are allowed to move to the rest of the fp-shell region (n = 6).

The results from the ANTOINE code are listed in Table 3.11 which shows J^{π}, the calculated energies, the corresponding spectroscopic factors S and $S^{\mathrm{rel.}}$ from the two previous considerations (n = 0) and (n = 6).

The Figures from: 3.18 to 3.22 show the spectroscopic factors normalized to that of the ground state spectroscopic factors $S^{\mathrm{rel.}}$ obtained experimentally (middle) compared to ANTOINE calculations with (n = 6) assumption (top) and with (n = 0) assumption (bottom) for $J^{\pi} = \frac{1}{2}^{-}, \frac{3}{2}^{-}, \frac{5}{2}^{-}, \frac{7}{2}^{-}$and $\frac{9}{2}^{-}$ levels.
By comparing the $S^{\mathrm{rel.}}$ values from both calculations (n = 0) and (n = 6) to our experimental results, in the previous figures, the closed shell assumption (n = 0) shows

energy values much higher than the experiment. Also it can not predict many of the levels observed experimentally, besides that it gives all the $J^\pi = \frac{7}{2}^-$ levels $S < 0.000001$, Figures 3.21 and 3.22, which means such levels would not be observable in this transfer reaction. The calculations with up to 6 particle hole excitations across the N = 28 gap (n = 6) show better agreement for the energy values and give S values for the $J = \frac{7}{2}^-$ levels near to what is obtained experimentally.

From those figures one can observe the better agreement of (n = 6) assumption with the experiment, although both calculations can not predict all the experimental levels.

Figure 3.23 shows the (n = 6) calculations compared to the experiment for all the levels in the first two columns left, then for each spin separately. The identification and connection between theoretical and experimental levels was based on the level energies and the normalized spectroscopic factor $S^{\mathrm{rel.}}$ values, which are shown more clearly in Figures 3.18 to 3.21. For example, in Figure 3.23 the theoretical level 3462.18 keV and the experimental level 3790.57 keV were connected because both have $J^\pi = \frac{1}{2}^-$ and they have $S^{\mathrm{rel.}}$ in the same order of magnitude, 0.322 and 0.651, respectively, where the other two neighboring experimental levels 3591.18 and 3826.53 keV have much lower $S^{\mathrm{rel.}}$,(0.0015) and (0.0024), respectively, Figure 3.18.

Generally, the agreement between theoretical shell model calculations with (n = 6) and experiment is very satisfactory up to 2.2 MeV as indicated in Figure 3.24 for the first 5 levels of ^{55}Fe, where the thick horizontal bars represent the spectroscopic factors, with S = 1 corresponding to the full length of the thin level line. Above 2.2 MeV the experiment observes more levels with $J^\pi = \frac{3}{2}^-$, $\frac{5}{2}^-$ and $\frac{7}{2}^-$ than predicted, Figure 3.23. This may be due to the fact that even more particle-hole excitations even from lower shells need to be taken into account. At the same time collective excitations coupled to the odd neutron may also play a role, which was not considered in this calculation. Also the measured absolute spectroscopic factor for the ground state (0.49) is in reasonable agreement with the (n = 6) calculation (0.62). The obtained spectroscopic factor for the ground state is also consistent with the values obtained by T. Taylor *et al.* [41] (0.575) with 25% uncertainty estimated for S and from D.C. Kocher *et al.* [19] (0.73) with 25% uncertainty.

It is also worth to mention here that the first positive parity state at 3804 keV observed experimentally with firmly established spin $J^\pi = 9/2^+$ arising from the $1g_{9/2}$ excitation has a surprisingly large cross-section ($\frac{\mathrm{d}\sigma}{\mathrm{d}\Omega}^{\mathrm{max}}$ = 1.85 mb/sr).

From the previous discussion we can extract that the magic number N = 28 is not very strong in ^{54}Fe, in agreement with the predictions by M. Honma *et al.* [17].
Now, to satisfy the second target of this thesis, another question needs to be answered, can the inverse kinematics reaction give the same conclusion ?
To answer this question the same (d,p) reaction was repeated in inverse kinematics and is reported in the next section.

J^{π}	$\mathrm{E_x}$(MeV)	$\mathrm{E_x}$(MeV)	$\mathrm{E_x}$(MeV)	S(abs)	S^{rel}	S(abs)	S^{rel}
	n=0	n=6	Exp.	n=0	n=0	n=6	n=6
$3/2^-$	0.00000	0.00000	0.000	0.87158	1.00000	0.61844	1.00000
$1/2^-$	0.97168	0.54410	0.411	0.24787	0.28439	0.34935	0.56490
$5/2^-$	1.21317	1.03747	0.931	0.70532	0.80924	0.49707	0.80374
$7/2^-$	1.20132	1.36430	1.316	0.00000	0.00000	0.02556	0.04134
$7/2^-$	2.80057	1.46865	1.408	0.00000	0.00000	0.00544	0.00880
$3/2^-$	1.93764	2.05125	2.051	0.08754	0.10044	0.06331	0.10237
$5/2^-$	1.78165	2.10525	2.144	0.09673	0.11098	0.12380	0.20018
$1/2^-$	2.45634	2.15925	1.918	0.03574	0.04101	0.07122	0.11517
$9/2^-$	2.13592	2.34889	2.211	0.00000	0.00000	0.00000	0.00000
$9/2^-$	2.55194	2.37784		0.00000	0.00000	0.00000	0.00000
$11/2^-$	1.99620	2.66596	2.539	0.00000	0.00000	0.00000	0.00000
$7/2^-$	3.20652	2.72278		0.00000	0.00000	0.01599	0.02585
$5/2^-$	2.67713	2.77896		0.00015	0.00017	0.00240	0.00388
$3/2^-$	2.67330	3.00679		0.02754	0.03160	0.08159	0.13193
$9/2^-$	3.59111	3.01688		0.00000	0.00000	0.00000	0.00000
$11/2^-$	2.90484	3.02135		0.00000	0.00000	0.00000	0.00000
$11/2^-$	3.52054	3.23844		0.00000	0.00000	0.00000	0.00000
$5/2^-$	3.29852	3.27446		0.09085	0.10423	0.01513	0.02446
$1/2^-$	2.93836	3.46218		0.71639	0.82194	0.19888	0.32158
$3/2^-$	3.67836	3.52779		0.00020	0.00023	0.04248	0.06869
$7/2^-$	4.14628	3.55393		0.00000	0.00000	0.00017	0.00028
$1/2^-$	-	3.75785		-	-	0.05640	0.09120
$9/2^-$	4.16251	4.01600		0.00000	0.00000	0.00000	0.00000
$11/2^-$	4.32950	4.10936		0.00000	0.00000	0.00000	0.00000
$5/2^-$	4.13647	4.16632		0.00061	0.00069	0.01327	0.02146
$3/2^-$	4.07242	4.30168		0.01314	0.01508	0.02347	0.03795
$7/2^-$	4.68770	4.54074		0.00000	0.00000	0.00164	0.00265
$9/2^-$	4.78784	4.77784		0.00000	0.00000	0.00000	0.00000
$11/2^-$	4.99349	5.05595		0.00000	0.00000	0.00000	0.00000
$1/2^-$	-	5.08093		-	-	0.00129	0.00208

Table 3.11.: Predicted J^{π}, E_{x}, S and $S^{\mathrm{rel.}}$ values for ^{55}Fe levels from the shell model calculations performed by A. Lisetskiy, using the ANTOINE code [5] and GXPF1 effective interaction from Otsuka *et al.* [17], considering
- The ^{54}Fe G.S. wave function has strong closed $1f_{7/2}$, no free nucleons (n = 0).
- The ^{54}Fe G.S. wave function has a broken $1f_{7/2}$ shell and up to 6 nucleons are allowed to move to the rest of the fp-shell region (n = 6).

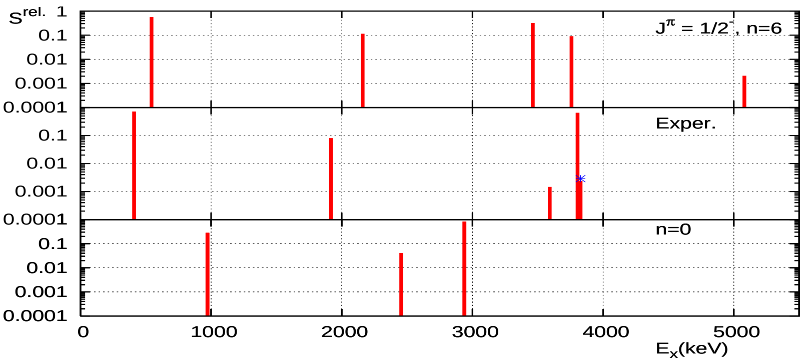

Figure 3.18.: $S^{\mathrm{rel.}}$ for $J^\pi = \frac{1}{2}^-$ levels.

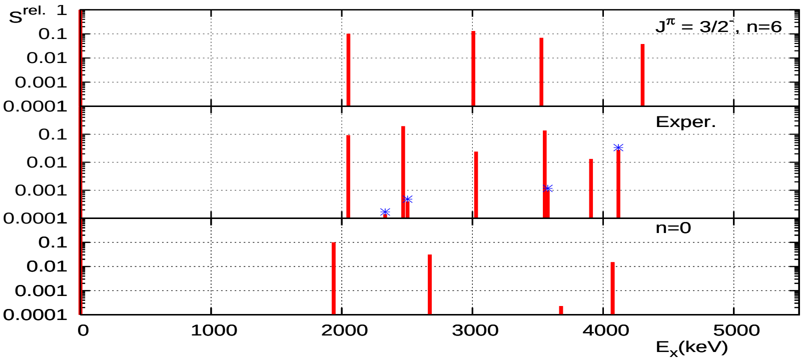

Figure 3.19.: $S^{\mathrm{rel.}}$ for $J^\pi = \frac{3}{2}^-$ levels.

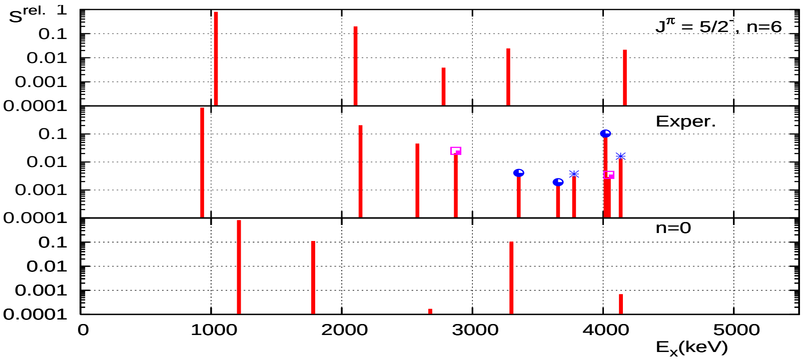

Figure 3.20.: Normalized spectroscopic factors $S^{\mathrm{rel.}}$ obtained experimentally (middle) compared to ANTOINE calculations under (n = 6) assumption (top) and under (n = 0) assumption (bottom) for $J^\pi = \frac{5}{2}^-$ levels.
$*$ new level.
• previously unknown spin.
☐ previously two possible spin values listed.
↓ levels with $S < 0.000001$ so they are not observed, but they are plotted to give an idea about their possible position.

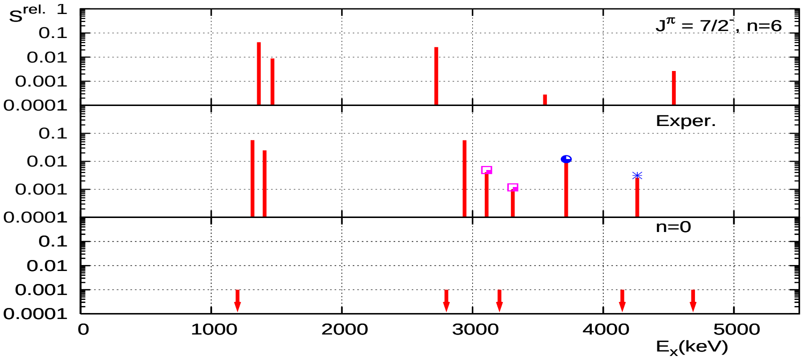

Figure 3.21.: $S^{\mathrm{rel.}}$ for $J^\pi = \frac{7}{2}^-$ levels.

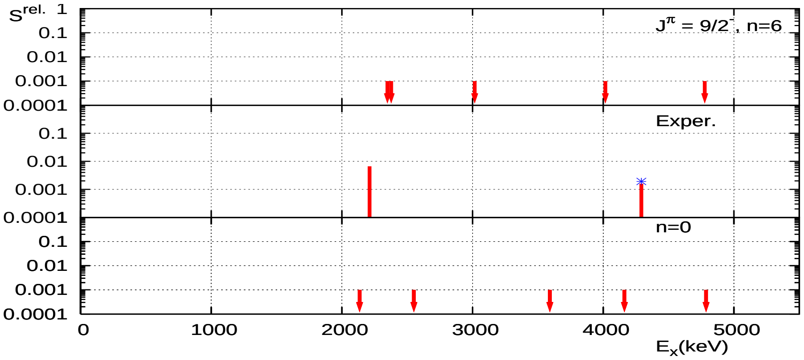

Figure 3.22.: $S^{\mathrm{rel.}}$ for $J^\pi = \frac{9}{2}^-$ levels.
↓ levels with $S < 0.000001$ so they are not observed, but they are plotted to give an idea about their possible position.

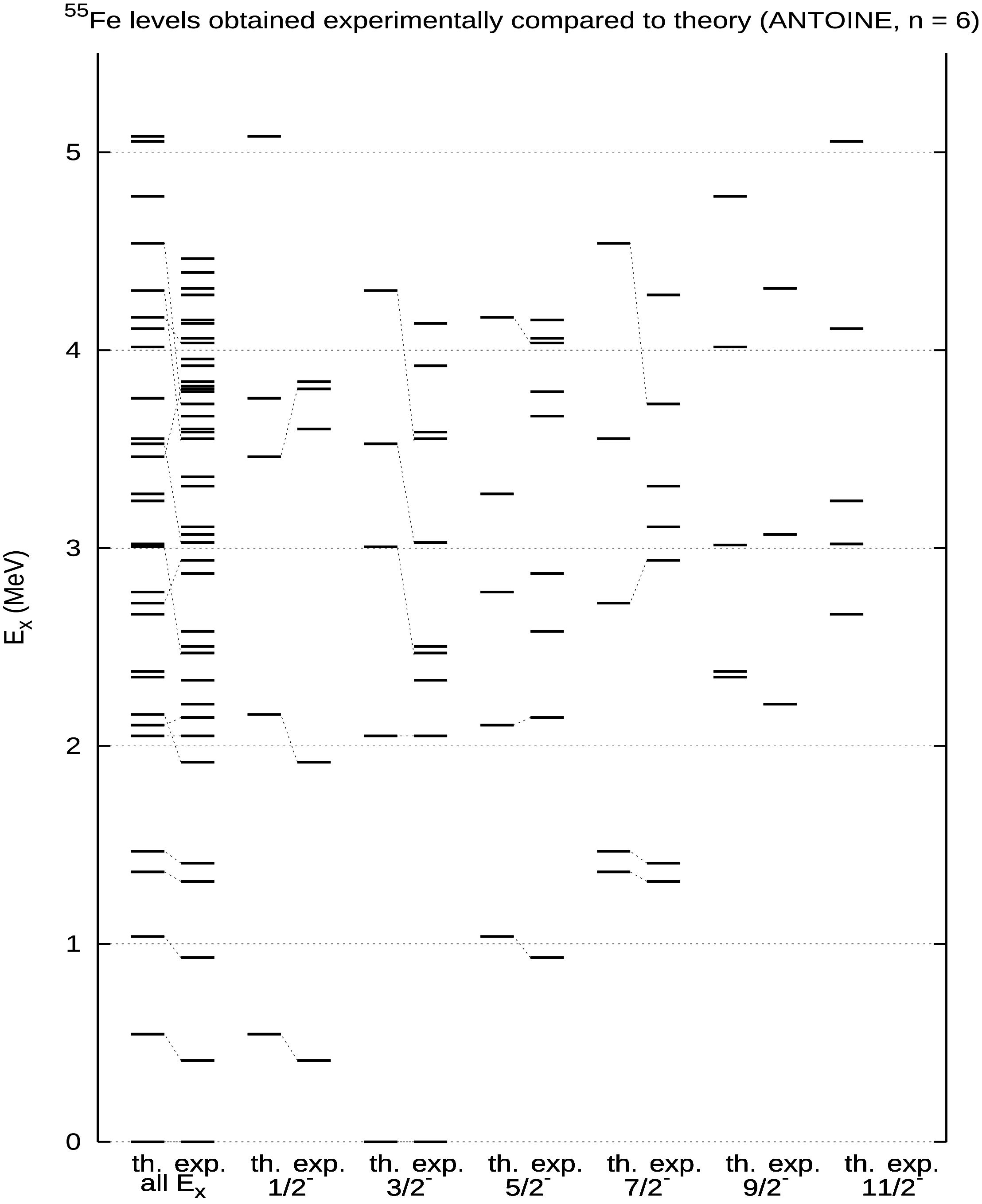

Figure 3.23.: ^{55}Fe levels obtained experimentally (exp.) up to E$_x$ = 4450 keV compared to theoretical calculations (th.) using ANTOINE code considering 6 free nucleons in the $1f_{7/2}$ shell (n = 6). It is clear that some improvement is achieved by breaking the shell, but only for $E_x < 2$ MeV. At higher levels the disagreement between the experiment and calculations become larger and larger. The number of experimental levels is more than the number from calculations. Levels with $J^\pi = \frac{9}{2}^-$ and $\frac{11}{2}^-$ have $S < 0.000001$ in the theoretical calculations, so they will not be observed, but they are plotted to give an idea about their possible position compared to experimental levels. Connection between (exp.) and (th.) levels is made to give an idea about the agreement or disagreement between experiment and theory. It was decided by connecting each level observed experimentally with a theoretically predicted one which has the same J and relatively similar S and E$_x$.

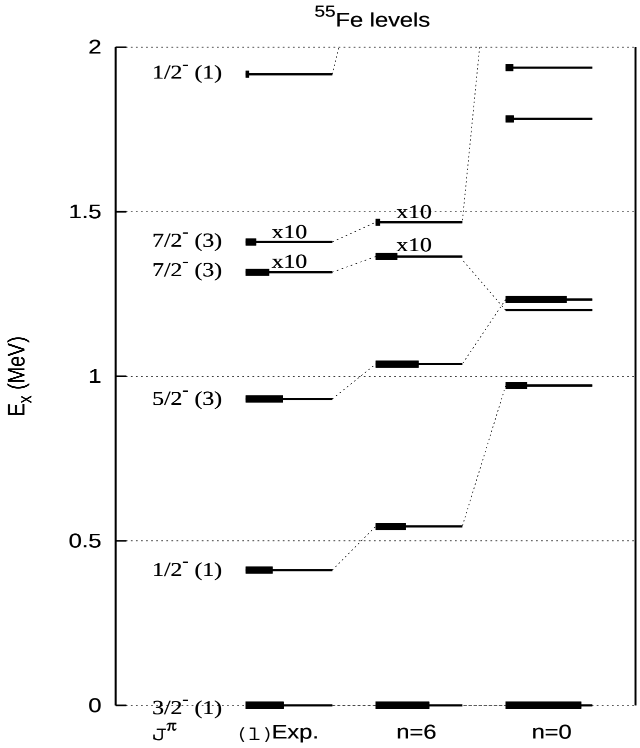

Figure 3.24.: ^{55}Fe experimental levels compared to predicted levels using ANTOINE code considering $1f_{7/2}$ as a closed shell labeled as n = 0 and as a broken shell with allowing up to 6 nucleons to be excited from th $1f_{7/2}$ to the rest of the fp-shell region labeled as n = 6. Thick horizontal bars represent the spectroscopic factors, with $S = 1$ corresponding to the full length of the thin level line.

3.2. Inverse Kinematics Reaction $\mathrm{d}(^{54}\mathrm{Fe},\mathrm{p})^{55}\mathrm{Fe}$

3.2.1. Introduction

One of the major goals of this thesis is to study how transfer reactions can be used to investigate the structure of exotic nuclei far off stability. Such nuclei can not be produced as targets, they must be used as radioactive beams. To perform a transfer reaction with a radioactive beam, inverse kinematics is needed.

After performing the normal kinematics reaction $^{54}\mathrm{Fe}(\vec{\mathrm{d}},\mathrm{p})^{55}\mathrm{Fe}$ in Section 3.1, we confirm that the N = 28 shell is not very strong in Fe and find that up to 6 particles 6 holes excitation across the N = 28 shell are needed to obtain reasonable agreement with the observed single-particle structure. To test whether inverse kinematics transfer reactions give the same results, the previous reaction is repeated again in inverse kinematics, by using the deuterons as the target and ^{54}Fe as the beam.

3.2.2. Experimental Procedure

The $\mathrm{d}(^{54}\mathrm{Fe},\mathrm{p})^{55}\mathrm{Fe}$ reaction was studied using a beam of ^{54}Fe accelerated by the MLL tandem Van de Graaff accelerator, (sect.2.1), to the lab energy $\mathrm{E}^{\mathrm{lab}}_{^{54}\mathrm{Fe}} = 134$ MeV = 2.488 AMeV (after deducing the beam energy lose in the target), which corresponds to the low CM energy for deuterons $\mathrm{E}^{\mathrm{CM}}_{\mathrm{d}} = 2.311$ AMeV, compared to the $\mathrm{E}^{\mathrm{CM}}_{\mathrm{d}} = 6.459$ AMeV used in the forward kinematics experiment. The target was 500 μg/cm^2 thick titanium foil loaded with deuterons with the ratio Ti:d, 1:1.13.

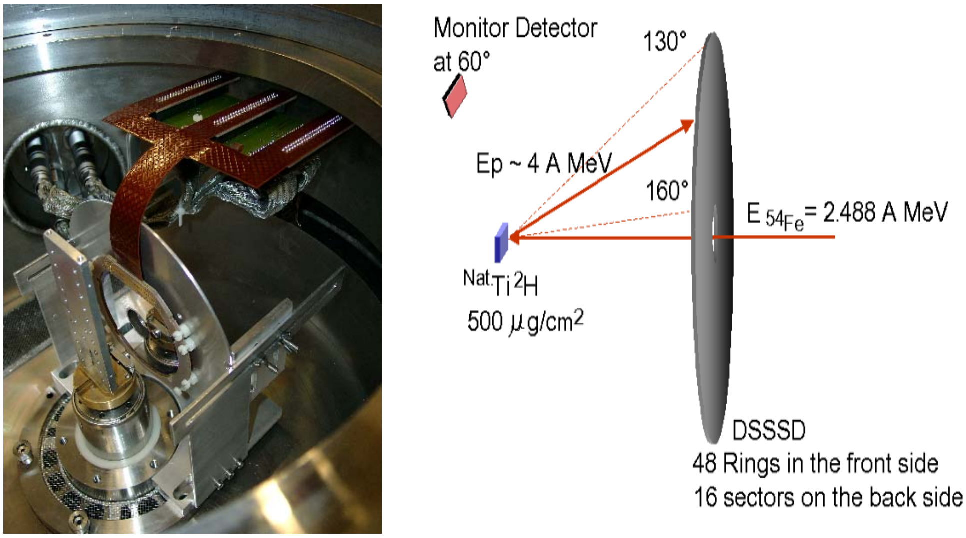

Figure 3.25.: The DSSSD set up for the $\mathrm{d}(^{54}\mathrm{Fe},\mathrm{p})^{55}\mathrm{Fe}$ reaction.

A 300 μm thick Double Sided Silicon Strip Detector (DSSSD) was used to detect the out going protons from the (d,p) reaction, more details about the detector are given in Section 2.3.2. The DSSSD was positioned 29 mm backwards from the target, (see Figure 3.25). In this way it covered an angular range from 129.6° to 159.2° in the Lab-system, which corresponds roughly to the angular range $\sim 10°$ to $\sim 30°$ in the

CM-system, where θ_{CM} varies depending on the excitation energy. By observing the shape of the angular distribution in this range $l = 0$, 1 & 2 transitions were easily identified. A monitor detector was placed in the reaction chamber to detect elastically scattered deuterons for the determination of the luminosity needed to deduce absolute differential cross-sections. The monitor was 85 mm away from the target and positioned at $\theta_{\text{Mon.}} = (60°)_{\text{lab}} = (60°)_{\text{CM}}$. At this angle elastically scattered particles can be observed and well separated as shown by a kinematic calculation previously performed using the program Kine [16]. Figure 3.26 (top) shows the monitor spectrum where the elastically scattered deuterons peak is identified.

A number of runs were collected during the beam time. 4 good runs with total run time = 7:49 hours are selected and summed to increase the statistics. The sum spectrum was analyzed using the Gaspan fitting program [38], see Figure 3.28.

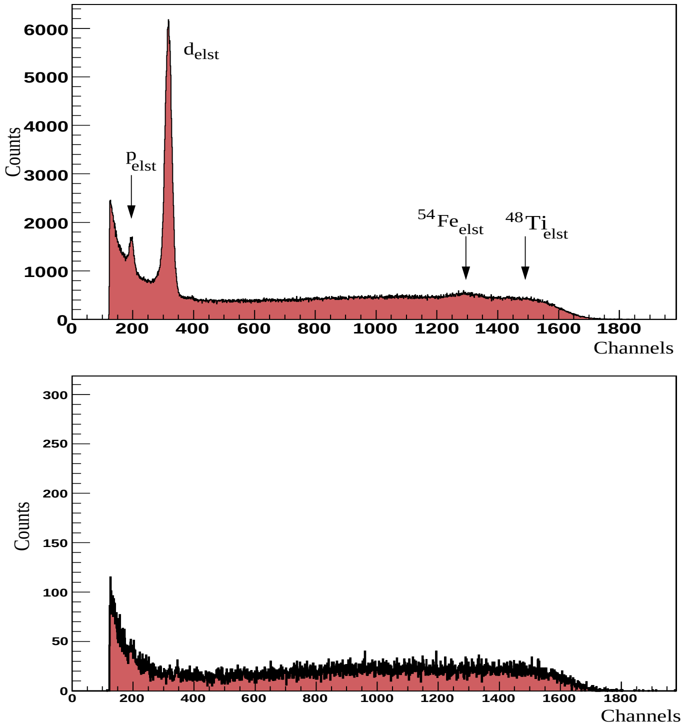

Figure 3.26.: The monitor detector spectrum from the d(^{54}Fe, p)^{55}Fe experiment using a beam of ^{54}Fe with energy $E^{\text{lab}}_{^{54}\text{Fe}} = 2.488$ AMeV with the titanium loaded deuterons target (top) for the sum of four runs and with a natural titanium target (bottom) for one run. By comparing the two spectra and from a previous calculation by Kine [16] the $d_{\text{elst.}}$ peak from elastically scattered d is identified and serves to measure $(N_{\text{beam}} \cdot N_{\text{target}})$. The detector is based in forward angle where elastic scattering products have higher $\frac{d\sigma}{d\Omega}$. P_{elst} peak raised from protons in the target and $^{48}\text{Ti}_{\text{elst}}$ from the target holding material.

3.2.3. Analysis

The reaction cross-section is usually calculated using relation 3.1 as in the forward kinematics section, but to avoid any mistake in calculating N_{beam} and N_{target}, we used in addition the Rutherford elastic scattering reaction $\mathrm{d}(^{54}\mathrm{Fe},\mathrm{d})^{54}\mathrm{Fe}$ measured with the monitor detector. The $(N_{\mathrm{beam}} \cdot N_{\mathrm{target}})$ was calculated by comparing the $\left(\frac{\mathrm{d}\sigma}{\mathrm{d}\Omega}\right)^{\mathrm{cm}}_{\mathrm{Ruth}}$ obtained from the Rutherford elastic scattering relation for the reaction $\mathrm{d}(^{54}\mathrm{Fe},\mathrm{d})^{54}\mathrm{Fe}$, where

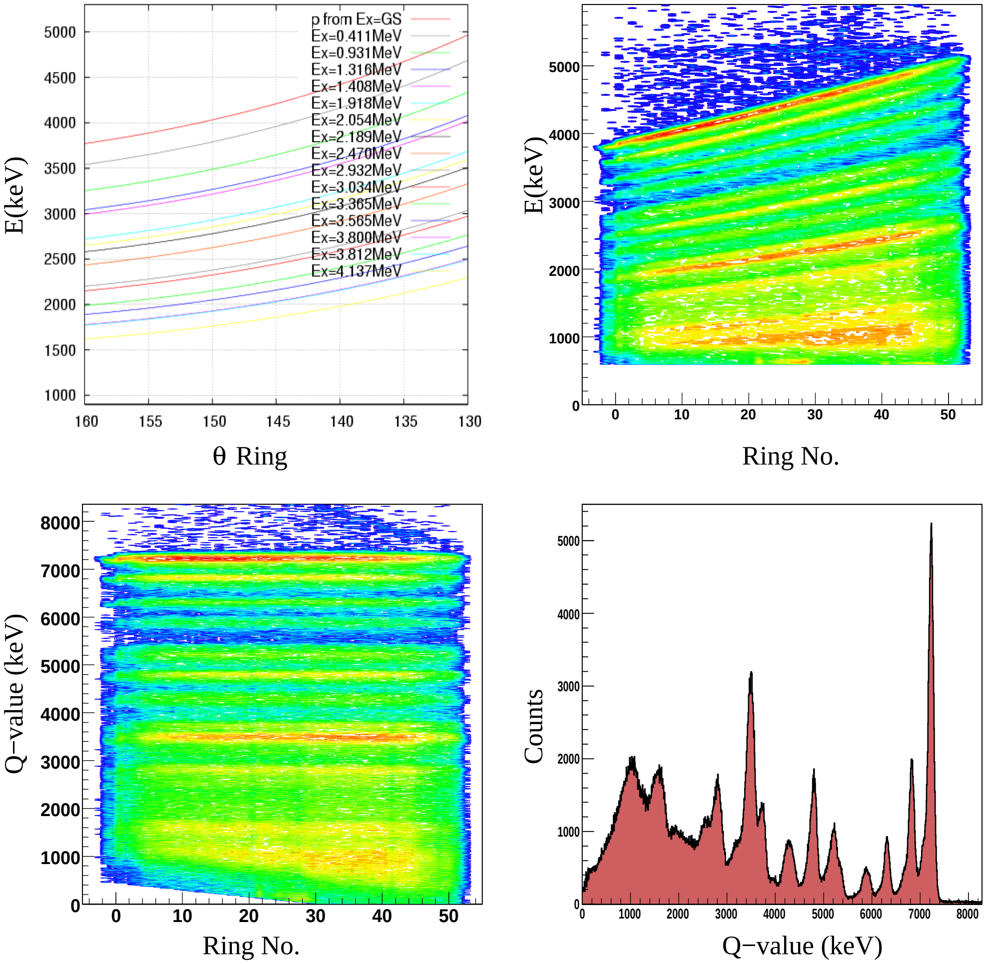

Figure 3.27.: A DSSSD spectrum compared to kine calculations for the reaction $\mathrm{d}(^{54}\mathrm{Fe},\mathrm{p})^{55}\mathrm{Fe}$ and $\mathrm{E}^{\mathrm{lab}}_{^{54}\mathrm{Fe}} = 2.488$ AMeV. The predicted shape of the 48 rings spectrum (top left) compared to experiment (top right). The events energy were translated to the reaction Q-value. With this step events from the same excitation level have the same position on each ring and the kinematics effect disappeared (bottom left). The Q-value spectrum was projected on y-axis (bottom right), where this spectrum was used to obtain Gaspan fitting parameters for the individual ring spectra.

$$\left(\frac{\mathrm{d}\sigma}{\mathrm{d}\Omega}\right)^{\mathrm{cm}}_{\mathrm{Ruth}} = \left(\frac{e^2}{4\pi\epsilon_o}\frac{Z_{^{54}\mathrm{Fe}}Z_{\mathrm{d}}}{4E_{\mathrm{cm}}\sin^2(\frac{\theta^{\mathrm{Mon.}}_{\mathrm{cm}}}{2})}\right)^2 \tag{3.8}$$

to the $\left(\frac{\mathrm{d}\sigma}{\mathrm{d}\Omega}\right)^{\mathrm{cm}}_{\mathrm{Ruth}}$ obtained experimentally for $\mathrm{d}_{\mathrm{elst.}}$ from the relation.

$$\left(\frac{d\sigma}{d\Omega}\right)^{\rm cm}_{\rm Ruth} = \frac{\mathrm{Count_d}}{(\Delta\Omega^{\rm lab}_{\rm Mon.}\cdot\frac{\Delta\Omega_{\rm cm}}{\Delta\Omega_{\rm lab}})\cdot N_{\rm beam}\cdot N_{\rm target}} \tag{3.9}$$

where $E_{\rm cm}$ refers to the energy of the relative motion between ^{54}Fe and d in the CM-system, $\theta^{\rm Mon.}_{\rm cm}$ is the monitor CM angle, $\Delta\Omega^{\rm lab}_{\rm Mon.} = 0.0019$ sr is the solid angle covered by the monitor in the lab-system, $\frac{\Delta\Omega_{\rm cm}}{\Delta\Omega_{\rm lab}} = 1.999$ is the transformation factor from the lab to the cm-system obtained from Kine program [16] for the monitor detector angle.

Because of the low statistics on each individual ring and to obtain the best fit parameters, the events from the 48 rings were summed into one spectrum, after translating the event energy to the reaction Q-value, thus removing all kinematics effects which is demonstrated in Figure 3.27.

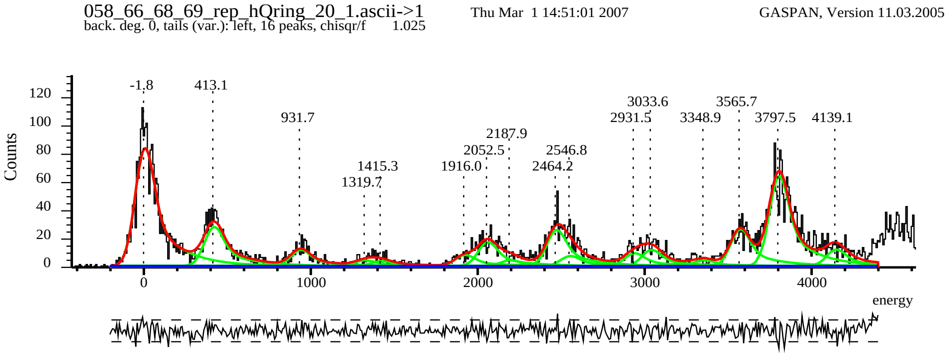

Figure 3.28.: A spectrum of a single ring of the DSSSD, ring 20, from the d(^{54}Fe, p)^{55}Fe reaction using a beam of ^{54}Fe with energy $\mathrm{E}^{\rm lab}_{^{54}\rm Fe} = 2.488$ AMeV. The lower part of the figure shows the residual between the fit and the data, normalized with the error of the data.

In this way the best fit parameters for Gaspan were obtained from the sum spectrum and then applied on each ring spectrum separately. An example for a Gaspan fit for ring number 20 is shown in Figure 3.28.

For the energy calibration the same steps were followed as in the forward reaction experiment. A calibration file with the calibration polynomial degree, position and the energy values from the Nuclear Data Sheets for some well known levels was given to Gaspan.

The ^{54}Fe levels were observed within about 700 channels, making a division into smaller fit regions as was done in the forward reaction part not very profitable. Tails were included in the peak fit and were set as a left tail type with decay constant and tail amplitude of about 22.4% and 2.1, respectively. The background was low, so it had a starting value of zero but the program was allowed to vary it. Peaks within the same spectrum had the same width. A primary width of 10 channels was observed, but the width increased with the ring number, because of the kinematic effect since the outer rings have bigger solid angles and cover a broad range in θ. In general the peaks had FWHM of 120 keV. The χ^2/N for the fit was around 1.1.

The experimental angular distributions were compared to the DWBA calculations using the coupled channel code CHUCK3 ref. [23] using the same three sets of OM-potentials used in the normal kinematics part after adjusting them to fit the new CM beam energy, see appendix (A). The parameters are given in Tables 3.12 - 3.14.

Potential		Real			Imaginary		
		V (MeV)	r_o (fm)	a_o (fm)	W (MeV)	r_I (fm)	a_I (fm)
Deuteron	Volume	-93.66	1.15	0.81			
	surface				15.6	1.34	0.68
	L.S	-7.185	1.07	0.66			
Proton	Volume	-56.04	1.17	0.75	-01.6	1.32	0.51
	surface				10.99	1.32	0.51
	L.S	-6.2	1.01	0.75			
Neutron	Volume	1.00	1.17	0.75			
	L.S	0.00	1.26	0.69			

Table 3.12.: Optical-Model parameters from Perey & Perey [32] and Feshbach [6] for a beam energy of $E^{\mathrm{lab}}_{^{54}\mathrm{Fe}} = 2.488$ AMeV.

Potential		Real			Imaginary		
		V (MeV)	r_o (fm)	a_o (fm)	W (MeV)	r_I (fm)	a_I (fm)
Deuteron	Volume	-92.64	1.05	0.86			
	surface				15.26	1.43	0.69
	L.S	-7.00	0.75	0.5			
Proton	Volume	-56.04	1.17	0.75	-01.6	1.32	0.51
	surface				10.99	1.32	0.51
	L.S	-6.2	1.01	0.75			
Neutron	Volume	1.00	1.17	0.75			
	L.S	0.00	1.26	0.69			

Table 3.13.: Optical-Model parameters from T. Taylor & J. A. Cameron [41], for a beam energy of $E^{\mathrm{lab}}_{^{54}\mathrm{Fe}} = 2.488$ AMeV.

The same steps as in Section 3.1 were followed in analyzing the results. Spectroscopic factors were determined by dividing the experimental cross-section $\sigma_{(\mathrm{Exp.})}$ over those obtained theoretically from DWBA calculations $\sigma_{(\mathrm{DWBA})}$ as in the relation 3.5. The average (Weighted Mean) of the normalized spectroscopic factors $S^{\mathrm{rel.}}_{\mathrm{Aver.}}$ of the three

Potential		Real			Imaginary		
		V (MeV)	r_o (fm)	a_o (fm)	W (MeV)	r_I (fm)	a_I (fm)
Deuteron	Volume	-93.25	1.17	0.72	-0.03	1.33	0.74
	surface				12.3	1.33	0.79
	L.S	-7.185	0.75	0.5			
Proton	Volume	-56.04	1.17	0.75	-1.6	1.32	0.51
	surface				10.99	1.32	0.51
	L.S	-6.2	1.01	0.75			
Neutron	Volume	1.00	1.17	0.75			
	L.S	0.00	1.26	0.69			

Table 3.14.: Optical-Model parameters from the Book: Theoretical Nuclear Physics, by Herman Feshbach [6], for a beam energy of $E^{lab}_{^{54}Fe} = 2.488$ AMeV.

sets of OM-parameters was calculated from the relation 3.6 and the error $\Delta S^{rel.}_{Aver.}$ from the relation 3.7.

3.2.4. The Results

The same analysis procedure as in the forward transfer reaction was performed here, see Section 3.1. Figures 3.29 - 3.32 show the angular distributions for the observed ^{54}Fe levels up to an excitation energy of E_x = 4137 keV and sorted by their total angular momentum. Energies, transferred angular momentum and spectroscopic factors compared to the published data are shown in Tables 3.15 and 3.16.

Less number of ^{55}Fe levels was observed now, 15 levels in total, compared to 34 in the normal kinematics in the same excitation energy window. This is due to the lower resolution of the DSSSD making it impossible to observe weakly populated states.

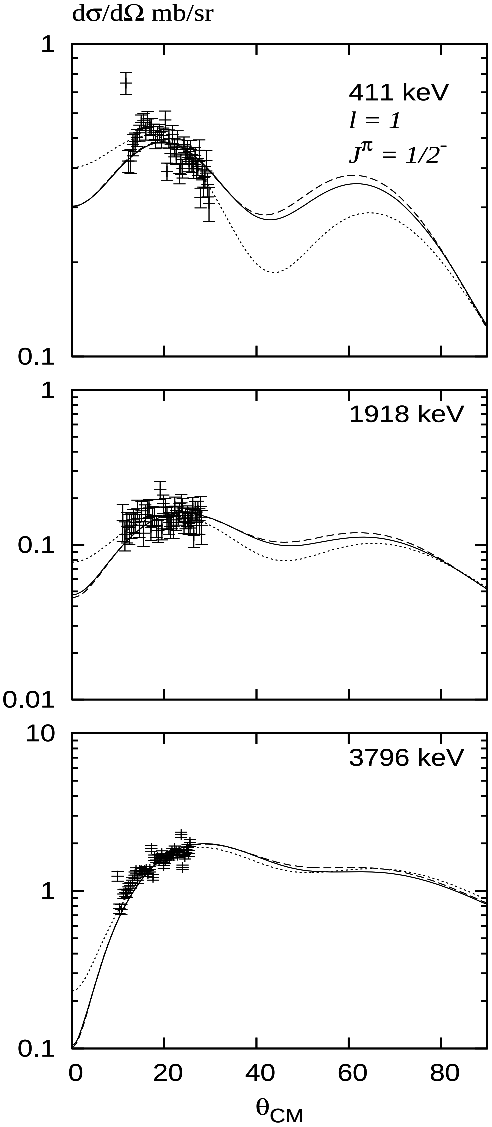

Figure 3.29.: The differential cross-section angular distribution for ^{55}Fe levels from the reaction d(^{54}Fe, p)^{55}Fe, $E^{\mathrm{lab}}_{^{54}\mathrm{Fe}}$= 2.488 AMeV, for l = 1 transfer and $J^{\pi} = 1/2^{-}$. Curves indicate the DWBA calculations by CHUCK3 using the three different sets of OM-potentials, C. M. Perey and F. G. Perey [32] (Full curve), T. Taylor and J. A. Cameron [41] (dotted curve) and Herman Feshbach [6] (dashed curve).

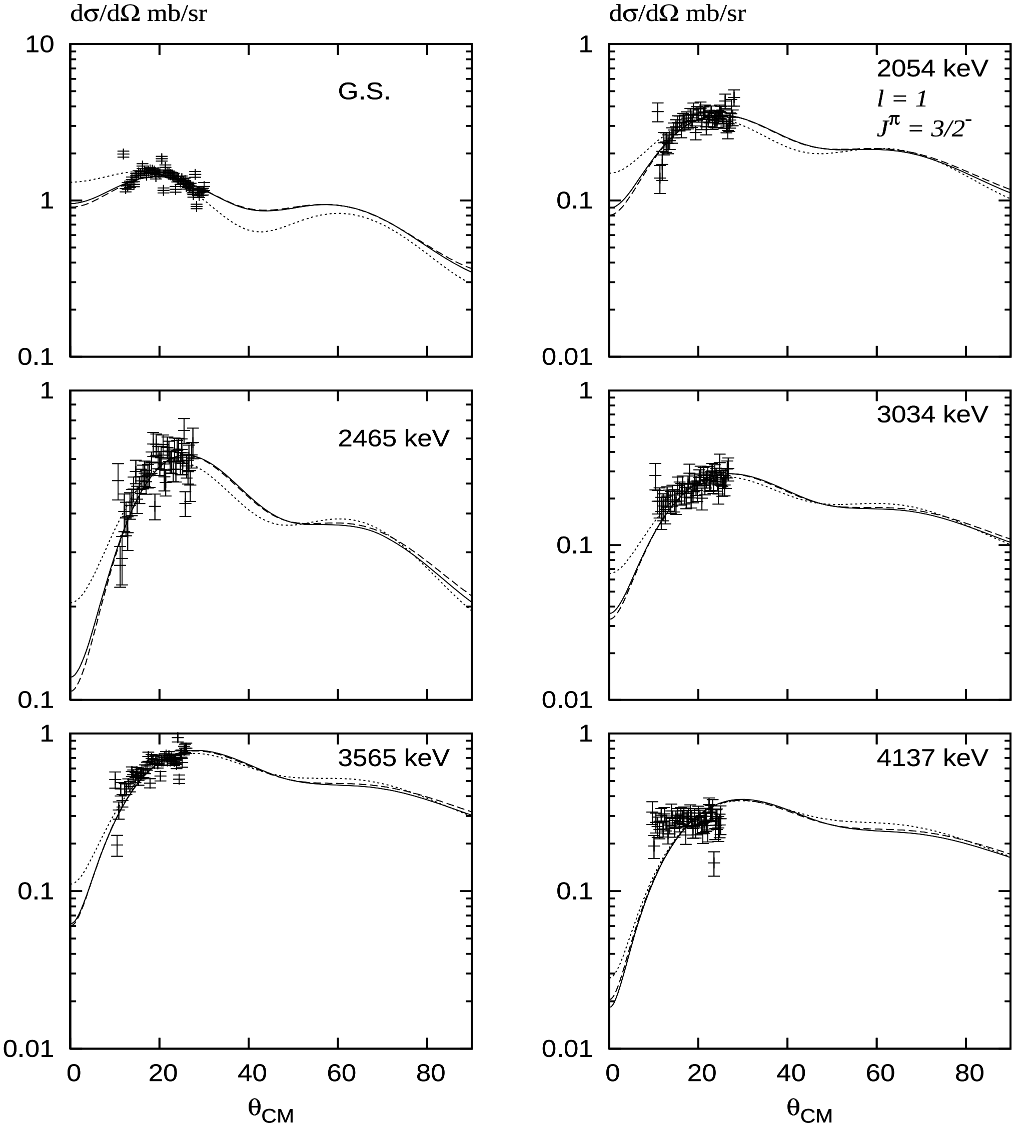

Figure 3.30.: The differential cross-section angular distribution for ^{55}Fe levels from the reaction d(^{54}Fe, p)^{55}Fe, $E^{\mathrm{lab}}_{^{54}\mathrm{Fe}}$= 2.488 AMeV, for $l = 1$ transfer and $J^{\pi} = 3/2^{-}$. Curves indicate the DWBA calculations by CHUCK3 using the three different sets of OM-potentials, C. M. Perey and F. G. Perey [32] (Full curve), T. Taylor and J. A. Cameron [41] (dotted curve) and Herman Feshbach [6] (dashed curve).

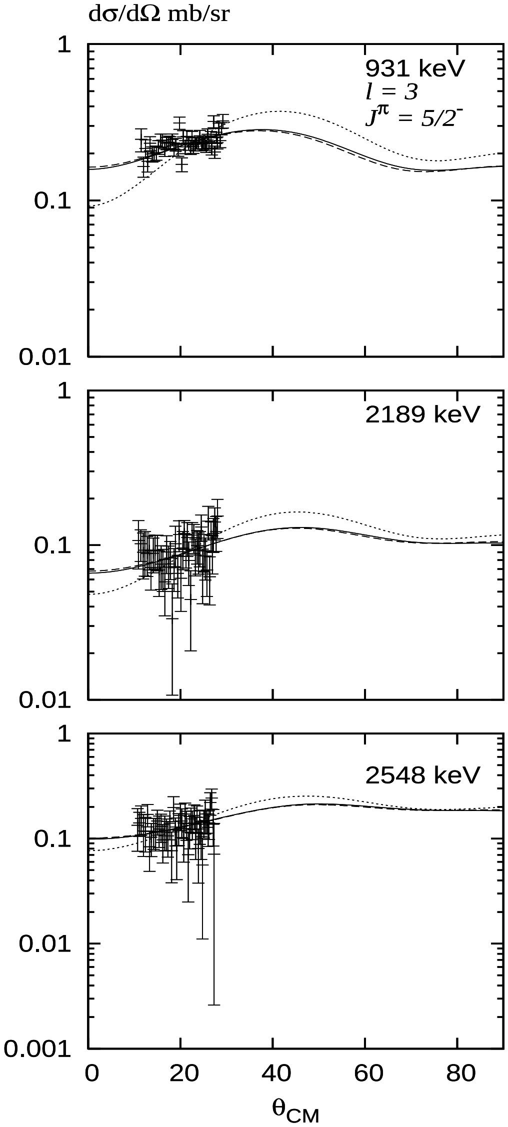

Figure 3.31.: The differential cross-section angular distribution for ^{55}Fe levels from the reaction d(^{54}Fe, p)^{55}Fe, $E^{\mathrm{lab}}_{^{54}\mathrm{Fe}}$= 2.488 AMeV, for $l = 3$ transfer and $J^{\pi} = 5/2^{-}$. Curves indicate the DWBA calculations by CHUCK3 using the three different sets of OM-potentials, C. M. Perey and F. G. Perey [32] (Full curve), T. Taylor and J. A. Cameron [41] (dotted curve) and Herman Feshbach [6] (dashed curve).

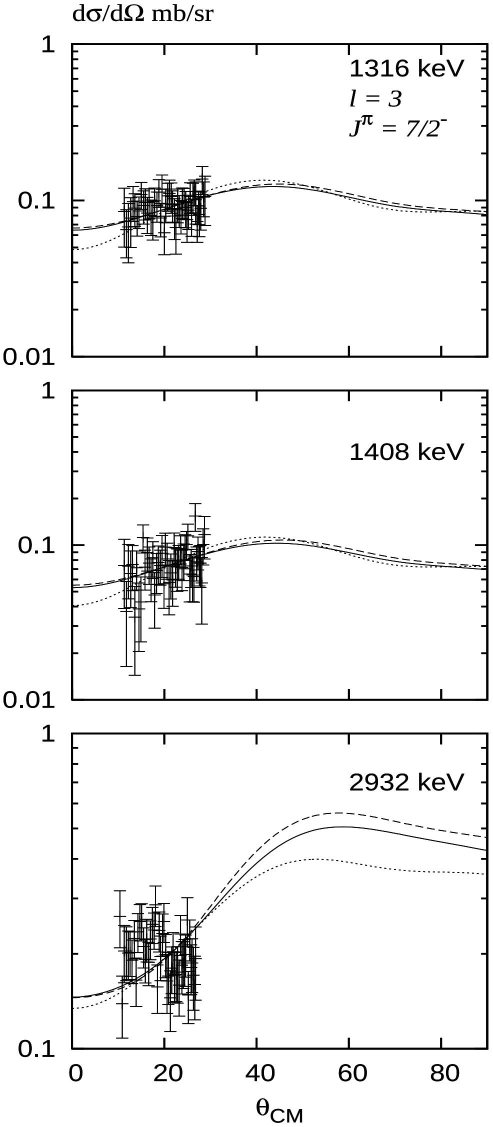

Figure 3.32.: The differential cross-section angular distribution for ^{55}Fe levels from the reaction d(^{54}Fe, p)^{55}Fe, $E^{\mathrm{lab}}_{^{54}\mathrm{Fe}}$= 2.488 AMeV, for l = 3 transfer and $J^\pi = 7/2^-$. Curves indicate the DWBA calculations by CHUCK3 using the three different sets of OM-potentials, C. M. Perey and F. G. Perey [32] (Full curve), T. Taylor and J. A. Cameron [41] (dotted curve) and Herman Feshbach [6] (dashed curve).

E_x (keV)	Δl	J^π	$E_\mathrm{x}, J^\pi_{\mathrm{Ref}[19]}$	$(\frac{d\sigma}{d\Omega})^{\max}_{\mathrm{mb/sr}}$ $\theta_{\max}$	$S^{\mathrm{Inv.}}_{\mathrm{Perey}}$	$S^{\mathrm{Inv.}}_{\mathrm{Taylor}}$	$S^{\mathrm{Inv.}}_{\mathrm{Feshbach}}$	absolute S $S^{\mathrm{Inv.}}_{\mathrm{Aver.}}$	absolute S $S^{\mathrm{Forw.}}_{\mathrm{Aver.}}$	relative S $S^{\mathrm{Inv.}}_{\mathrm{Aver.}}$	relative S $S^{\mathrm{Forw.}}_{\mathrm{Aver.}}$
0.0	1	$\frac{3}{2}^-$	0.0,$\frac{3}{2}^-$	1.56(5) 19.7	0.445(2)	0.472(3)	0.518(3)	0.48(4)	0.49(1)	1.000	1.000
413.11(0.46)	1	$\frac{1}{2}^-$	411.42(21),$\frac{1}{2}^-$	0.55(3) 16.0	0.304(3)	0.313(3)	0.353(3)	0.32(3)	0.35(1)	0.68(1)	0.72(1)
931.75(0.41)	3	$\frac{5}{2}^-$	931.29(13),$\frac{5}{2}^-$	0.28(2) 28.6	0.406(6)	0.656(9)	0.447(6)	0.46(14)	0.43(2)	0.9(3)	0.87(2)
1319.71(0.45)	3	$\frac{7}{2}^-$	1316.54(13),$\frac{7}{2}^-$	0.10(3) 28.2	0.105(4)	0.124(4)	0.125(4)	0.12(1)	0.0281(8)	0.25(2)	0.057(1)
1415.28(0.45)	3	$\frac{7}{2}^-$	1408.45(14),$\frac{7}{2}^-$	0.10(2) 27.3	0.088(4)	0.103(4)	0.105(4)	0.097(9)	0.0121(5)	0.21(1)	0.025(1)

Table 3.15.: Table showing ^{55}Fe levels from the reaction $d(^{54}\mathrm{Fe},p)^{55}\mathrm{Fe}$, $E^{\mathrm{lab}}_{^{54}\mathrm{Fe}} = 2.488$ AMeV, transferred angular momentum Δl, total angular momentum J^π from this work, compared to the excitation energies E_x and J^π from the nuclear data sheets ref. [19], maximum cross-section and its position, spectroscopic factors S from the three different OM-parameters sets, the weighted average of those spectroscopic factors $S^{\mathrm{Inv.}}_{\mathrm{Aver.}}$, compared to the weighted average obtained from the forward kinematic reaction $S^{\mathrm{Forw.}}_{\mathrm{Aver.}}$, and their normalized to the G.S. averages, respectively.

S_{Perey}: S is deduced using OM-parameters for DWBA calculations from C. M. Perey and F. G. Perey [32],

S_{Taylor}: S is deduced using OM-parameters for DWBA calculations from T. Taylor and J. Cameron [41]

S_{Feshbach}: S is deduced using OM-parameters for DWBA calculations from H. Feshbach [6].

E_x (keV)	Δl	J^π	$E_\mathrm{x}, J^\pi_{\mathrm{Ref[19]}}$	$(\frac{d\sigma}{d\Omega})^{\mathrm{max}}_{\mathrm{mb/sr}}$ θ_{max}	$S^{\mathrm{Inv.}}_{\mathrm{Perey}}$	$S^{\mathrm{Inv.}}_{\mathrm{Taylor}}$	$S^{\mathrm{Inv.}}_{\mathrm{Feshbach}}$	absolute S $S^{\mathrm{Inv.}}_{\mathrm{Aver.}}$	absolute S $S^{\mathrm{Forw.}}_{\mathrm{Aver.}}$	relative S $S^{\mathrm{Inv.}}_{\mathrm{Aver.}}$	relative S $S^{\mathrm{Forw.}}_{\mathrm{Aver.}}$
1916.01(0.47)	1	$\frac{1}{2}^-$	1918.3(5),$\frac{1}{2}^-$	0.17(2) 19.8	0.069(2)	0.071(2)	0.080(2)	0.073(6)	0.0400(3)	0.153(2)	0.081(2)
2052.45(0.46)	1	$\frac{3}{2}^-$	2051.7(4),$\frac{3}{2}^-$	0.37(3) 25.4	0.064(1)	0.069(1)	0.074(1)	0.069(5)	0.046(1)	0.145(1)	0.093(3)
2187.93(0.45)	3	$\frac{5}{2}^-$		0.13(3) 27.4	0.181(7)	0.252(10)	0.202(8)	0.21(4)	–	0.43(8)	–
2464.16(0.41)	1	$\frac{3}{2}^-$	2470.2(6),$\frac{3}{2}^-$	0.64(5) 25.0	0.100(1)	0.108(1)	0.114(2)	0.107(7)	0.0963(2)	0.224(4)	0.196(6)
2548.76(0.4)	3	$\frac{5}{2}^-$	2577.7(4),$\frac{5}{2}^-$	0.18(4) 26.2	0.29(1)	0.36(2)	0.32(2)	0.32(5)	0.0224(9)	0.67(9)	0.046(1)
2932.53(0.35)	3	$\frac{7}{2}^-$	2938.9(4),$\frac{7}{2}^-$	0.24(3) 17.4	0.352(9)	0.320(8)	0.436(1)	0.36(6)	0.0280(5)	0.76(9)	0.057(2)
3033.62(0.34)	1	$\frac{3}{2}^-$	3028.5(7),$\frac{3}{2}^-$	0.28(4) 26.2	0.039(1)	0.043(1)	0.045(1)	0.042(3)	0.0119(2)	0.089(3)	0.0241(8)
3553.37(0.46)	1	$\frac{3}{2}^-$	3552.3(8),$\frac{3}{2}^-$	0.76(5) 25.5	0.090(1)	0.101(1)	0.102(1)	0.097(7)	0.0671(1)	0.20(0)	0.1363(3)
3797.50(0.6)	1	$\frac{1}{2}^-$	3800(10),$\frac{3}{2}^-$	1.85(6) 23.2	0.470(3)	0.518(3)	0.537(3)	0.51(4)	0.3208(6)	1.06(3)	0.651(1)
4137.07(0.87)	1	$\frac{3}{2}^-$	4123(10),NoJ	0.31(4) 22.7	0.037(1)	0.042(1)	0.042(1)	0.040(3)	0.0137(2)	0.084(5)	0.028(1)

Table 3.16.: Table showing ^{55}Fe levels from the reaction d(^{54}Fe, p)^{55}Fe, $\mathrm{E}^{\mathrm{lab}}_{^{54}\mathrm{Fe}}$= 2.488 AMeV, transferred angular momentum Δl, total angular momentum J^π from this work, compared to the excitation energies E_x and J^π from the nuclear data sheets ref. [19], maximum cross-section and its position, spectroscopic factors S from the three different OM-parameters sets, the weighted average of those spectroscopic factors $S^{\mathrm{Inv.}}_{\mathrm{Aver.}}$, compared to the weighted average obtained from the forward kinematic reaction $S^{\mathrm{Forw.}}_{\mathrm{Aver.}}$, and their normalized to the G.S. averages, respectively.

3.2.5. Discussion

Reasonable agreement between the experimental results and DWBA calculations is observed, mostly for well separated levels and levels with high reaction cross-section. Due to the low energy the angular distributions are less pronounced, making it very difficult to distingush between levels with $\Delta l > 2$ values. For many levels, the average (Weighted Mean) of the normalized spectroscopic factors $S^{\mathrm{rel.}}_{\mathrm{Aver.}}$ can be reliably extracted and agrees with the normalized spectroscopic factors from normal kinematic presented previously in this work, Section 3.1 and also with that from D. C. Kocher $S^{\mathrm{rel.}}_{\mathrm{Ref[19]}}$, Tables 3.15 and 3.16. Disagreement is observed when overlap between different levels occurs or if the levels are weakly populated, like the 1316 and 1408 keV levels. Also the lower beam energy here ($\mathrm{E}^{\mathrm{lab}}_{^{54}\mathrm{Fe}} = 2.488$ AMeV) and the reliability of the new OM-parameter sets and so $\sigma_{(\mathrm{DWBA})}$ calculated from this energy can play an important role. For example the 1316 and 1408 keV levels produced nearly equal $S^{\mathrm{rel.}}$, although in our normal kinematic experiment and in the published data $S^{\mathrm{rel.}}_{1316\mathrm{keV}}$ should be about 3 times more than $S^{\mathrm{rel.}}_{1408\mathrm{keV}}$. Also $S^{\mathrm{rel.}}$ for both levels are higher than the obtained values from the normal kinematic reaction and the published data. However we attribute this discrepancy to their lower spectroscopic factors, for which a reaction at such a low reaction energy does not produce reliable results.
The levels 1916 (1918 5), 2052.42 (2051.7 4), 3033.62 (3028.5 7), 3553.37 (3552.3 8), 3797.5 (3800 10) and 4137 (4123 10) keV also have higher S values than in the normal kinematic experiment, but still in the same order of magnitude. The experimental angular distributions for the levels 2932 and 4137 keV show flat and featureless shapes due to their low reaction cross-section.
In spite of the lower DSSSD resolution and the lower reaction cross-section, the levels 1314, 1408 and 2932 keV with $J^{\pi} = \frac{7}{2}^{-}$ are observed.

In general the total number of the observed levels here (15 levels) is less than the number observed in normal kinematic (39 levels), on one hand because of the lower observation limit now compared with the limit in normal kinematic. On the other hand due to the lower DSSSD resolution $\simeq 150$ keV, which results in the fact that some of the known levels can not be observed or separated, due to their low cross-section, for example 2503, 2579, 2872 keV levels, and because of their overlap with levels with higher cross-section. For example the observed 2464 keV level could be the 2470 keV, which has $\frac{\mathrm{d}\sigma}{\mathrm{d}\Omega}^{\mathrm{max}} = 3.46$ mb/sr in normal kinematic and hide the levels 2332, 2503 keV with $\frac{\mathrm{d}\sigma}{\mathrm{d}\Omega}^{\mathrm{max}} = 0.003$, 0.007 mb/sr respectively, where all of them have $J^{\pi} = 3/2^{-}$.

The three OM-parameter sets lead to similar $S^{\mathrm{rel.}}$ but the disagreement between S obtained from normal kinematic and S obtained from inverse kinematic or more clearly between $S_{\mathrm{E_{Beam}} \simeq 2.5\ \mathrm{AMeV}}$ and $S_{\mathrm{E_{Beam}} \simeq 7\ \mathrm{AMeV}}$ could raise the question about the reliability of the extrapolating the used OM-parameters to such low beam energy.

Chapter 4

Two Neutron Transfer Reaction

4.1. Introduction

The stability of the magic number N = 28 was tested in the previous Chapter (3) by performing precision spectroscopy of levels up to 4.463 MeV in ^{55}Fe. In this chapter we investigated two-neutron transfer and its sensitivity to pairing correlations and the breaking of the N = 28 shell closure in ^{56}Ni.
Neutron pairing was studied for N = 28 in Ni isotopes using the two neutron transfer reaction $^{58}\mathrm{Ni}(\vec{\mathrm{p}},\mathrm{t})^{56}\mathrm{Ni}$ combined with the single neutron transfer reaction $^{58}\mathrm{Ni}(\vec{\mathrm{p}},\mathrm{d})^{57}\mathrm{Ni}$ to study the transfer mechanism. The latter reaction is important to obtain information on the role of two-step reactions proceeding through states in ^{57}Ni. In principle, also the reaction $^{57}\mathrm{Ni}(\vec{\mathrm{d}},\mathrm{t})^{56}\mathrm{Ni}$ should be studied, however, due to the short half-life of ^{57}Ni target ($t_{1/2}$ = 36 h) we can only rely on the DWBA calculations.

The main point in this experiment is to test the neutron pairing correlation in Ni and the role of cross-shell excitation in ^{56}Ni, by testing the two-neutron transfer mechanism and the contribution of simultaneous and sequential transfer. We also investigate if the (p,t) reaction, namely the obtained angular distributions, are sensitive to the presence of particle-hole contributions in the ^{56}Ni wave functions due to the breaking of the N = 28 shell.

In the second part of this chapter we studied the two neutrons transfer in inverse kinematics as a feasibility study for future (t,p) experiments in inverse kinematics with short-lived nuclei. Due to issues related to the use of the tritium target we performed the experiment at the HMI Berlin, where a ^{40}Ar beam was available.

The $^{58}\mathrm{Ni}(\vec{\mathrm{p}},\mathrm{t})^{56}\mathrm{Ni}$ and $^{58}\mathrm{Ni}(\vec{\mathrm{p}},\mathrm{d})^{57}\mathrm{Ni}$ reactions were studied before by J. H. Polane *et al.* [34] and [33], respectively, with $\mathrm{E}_\mathrm{p}^\mathrm{lab}$ = 24.6 MeV. However, for the (p,t) reaction they studied only the ^{56}Ni G.S. and assumed an inert ^{56}Ni core with closed $1f7/2$ shell. In this work we observed and included another three higher levels into the study and took into account the breaking of the $1f7/2$ shell in the shell model calculations.
The $^{40}\mathrm{Ar}(\mathrm{t},\mathrm{p})^{42}\mathrm{Ar}$ reaction was studied before by E. R. Flynn *et al.* [8] in normal kinematic and with higher beam energy, $\mathrm{E}_\mathrm{t}^\mathrm{lab}$ = 20 MeV, compared to the experiment presented here. They measured the E_x, identified l and J values for the observed levels, but they didn't measure explicitly the spectroscopic factors, rather a related value "Enhancement factor"ε, which describes the ratio between σ_exp and σ_DWBA. More discussion about this point is presented in Section 4.3.5.

Despite the low DSSSD resolution, more ^{42}Ar levels were observed in the energy range under the study of this work compared to E. R. Flynn *et al.* [8]. The transferred angular momentum $l_{\text{trans.}}$ for many levels were identified and the scaling factors between σ_{exp} and σ_{DWBA} were deduced for each level. In this way one can compare the inverse kinematics results obtained from the current work with the normal kinematics results by E. R. Flynn *et al.* [8] and judge if the inverse kinematics are able to detect and measure the level energies and deduce $l_{\text{trans.}}$ as efficient as normal kinematics, paving the road for future (t,p) experiments in inverse kinematics with short-lived nuclei.

4.2. Forward Kinematics Reactions $^{58}\mathrm{Ni}(\vec{\mathrm{p}},\mathrm{d})^{57}\mathrm{Ni}$ and $^{58}\mathrm{Ni}(\vec{\mathrm{p}},\mathrm{t})^{56}\mathrm{Ni}$

4.2.1. Experimental Procedures.

Nearly the same procedures as presented in Section 3.1 are repeated here for the one- and two-neutron transfer reaction $^{58}\mathrm{Ni}(\vec{\mathrm{p}},\mathrm{d})^{57}\mathrm{Ni}$ and $^{58}\mathrm{Ni}(\vec{\mathrm{p}},\mathrm{t})^{56}\mathrm{Ni}$, respectively. The light ion reactions were performed by bombarding ^{58}Ni enriched targets, 99.89%, with 24.6 MeV polarized protons from the MLL tandem Van de Graaff accelerator. Three targets were used with the thickness 111, 240, 400 $\pm 10\%$ $\mu\mathrm{g/cm}^2$, prepared by evaporation. The 111 $\mu\mathrm{g/cm}^2$ target was used for the reaction $^{58}\mathrm{Ni}(\vec{\mathrm{p}},\mathrm{d})^{57}\mathrm{Ni}$ except in the back angular range $\theta^{\text{lab}}_{\text{Q3D}}$ from 70° to 90° where a thicker target 240 $\mu\mathrm{g/cm}^2$ was used because of the lower cross-section in this part. For the $^{58}\mathrm{Ni}(\vec{\mathrm{p}},\mathrm{t})^{56}\mathrm{Ni}$ reaction the 240 $\mu\mathrm{g/cm}^2$ was used for the ^{56}Ni ground state. For the weakly populated level at 2700 keV the thick 400 $\mu\mathrm{g/cm}^2$ target was used. For the two close ^{56}Ni levels at 3923 and 3956 keV the thin 111 $\mu\mathrm{g/cm}^2$ target was used.

The reaction products were analyzed with the Garching Q3D magnetic spectrograph and detected by the proportional counter filled with isobutane gas (500 mbar) introduced in Section 2.2.

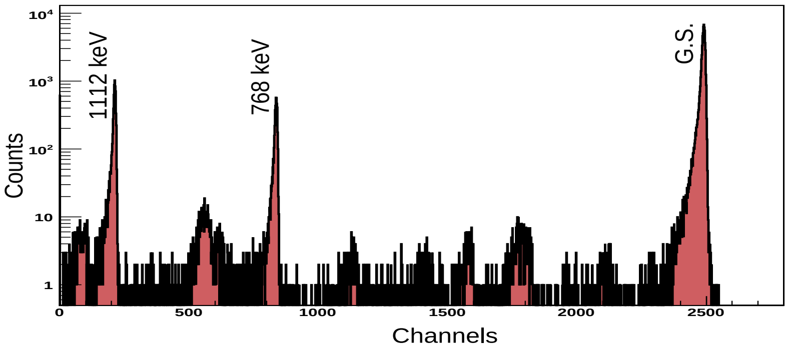

Figure 4.1.: Focal plane spectrum of the deuterons from the reaction $^{58}\mathrm{Ni}(\vec{\mathrm{p}},\mathrm{d})^{57}\mathrm{Ni}$, $\mathrm{E}_{\mathrm{p}}^{\text{lab}} =$ 24.6 MeV, observed at 20° with spin up polarized proton beam. Q3D excitation energy setting centered at 430 keV.

The differential cross-sections $\frac{d\sigma}{d\Omega}$ were measured up to an excitation energy $\mathrm{E}_{\mathrm{x}} =$ 1112 keV for ^{57}Ni and $\mathrm{E}_{\mathrm{x}} = 3956$ keV for ^{56}Ni. Each Q3D magnet setting covers an energy range of about 1400 keV, so that for the $(\vec{\mathrm{p}},\mathrm{d})$ reaction one Q3D magnetic set-

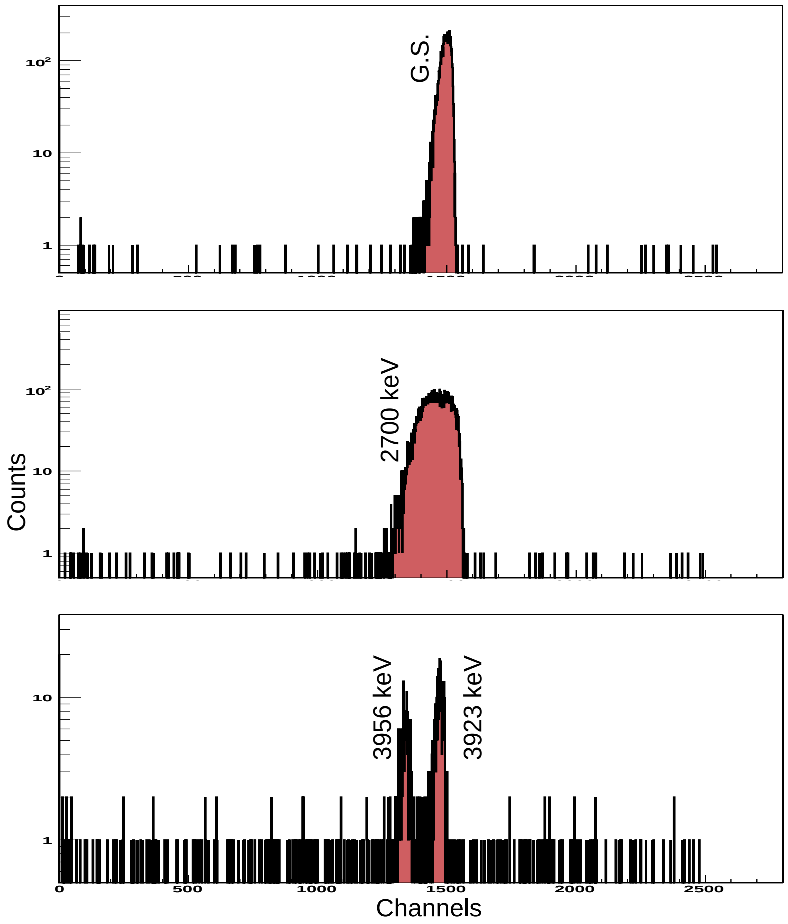

Figure 4.2.: Focal plane spectra of tritons from the reaction $^{58}\mathrm{Ni}(\vec{\mathrm{p}},\mathrm{t})^{56}\mathrm{Ni}$, $\mathrm{E}_{\mathrm{p}}^{\mathrm{lab}} = 24.6$ MeV, observed at 20° with spin up polarized proton beam. Q3D excitation energy setting centered at 0.0 keV (top), 2700 keV (middle) and 3900 keV (bottom). The 2700 keV level has a broad peak because a thicker target (400 $\mu\mathrm{g/cm}^2$) was used because it is weakly populated.

ting centered at $\mathrm{E}_{\mathrm{x}} = 430$ keV was enough to detect the first three important levels in ^{57}Ni as shown in the spectrum of Figure 4.1.

For the $(\vec{\mathrm{p}},\mathrm{t})$ reaction the Q3D was adjusted to three different magnetic settings centered at 0, 2700 & 3900 keV, Figure 4.2.

The experimental reaction cross-sections $\sigma_{\mathrm{Exp.}}$ for ^{57}Ni and ^{56}Ni levels were measured using a spin-up and spin-down polarized proton beam separately. The measurements covered an angular range from 5° to 90° in 5° steps and in some parts in 2.5° steps in order to determine detailed features of the angular distribution. For the last Q3D magnet setting at 3900 keV the measurements covered an angular range from 20° to 70° in 10° steps.

The angular distributions and analyzing powers for ^{57}Ni and ^{56}Ni levels were deduced by measuring the reaction cross-sections at different angles. Spectroscopic factors for the one-neutron transfer and the ratio between simultaneous and sequential transfers for two-neutron transfer were calculated by comparing the experimental cross-sections

$\sigma_{\mathrm{Exp.}}$ to those obtained theoretically from DWBA calculations σ_{DWBA}.

4.2.2. Analysis.

The experimental reaction cross-section $\sigma_{\mathrm{Exp.}}$ was determined as in the forward kinematics reaction in Section 3.1 using the Relation 3.1. The analyzing power $\mathrm{A_y}$ was also measured using the Relation 3.4, where the degree of polarization p of the beam was 0.6.

The 2500 channel focal plane spectra for the deuterons and tritons were fitted using the program GASPAN [38]. The expected Ni peaks were selected and fitted by giving the program a list with their positions.

For the deuteron spectra, the peak width was fixed to 10 channels, with a ±10% variation range. The peak tails were included in the fit and were set as a left type with about 0.0926% amplitude and decay constant set to 12.35. The background was inserted in the fit and set to a polynomial degree 1. The background tail was also included in the fit. In general the peaks had FWHM of 2.3 keV. The χ^2/N for the fit was around 1.1. An example for the fit is illustrated in Figure 4.3.

The same procedures were performed for the triton spectra, where we had three different Q3D magnetic settings. The peak tail amplitude was about 10% and the decay constant set to 17. The peak width was about 25 channels with ±10% variation range. In general peaks had FWHM of around 6 keV. For the 2700 keV peak it was around 31 keV because a thicker target (400 μg/cm^2) was used. The χ^2/N for the fit was mostly about 1. An example for the triton spectra fit is illustrated in Figure 4.4.

Because maxmum of three levels were observed in each Q3D setting, no energy calibration was performed and known energy values from the nuclear data tables were used.

4.2.3. Optical Potentials.

The optical-model OM parameters used in the DWBA calculations are listed in Table 4.1. The proton, deuteron and neutron potentials are taken from Polane *et al.* [33]. The triton potentials are taken from Polane *et al.* [34].

The proton potential was extracted in ref: [13] from a global fit to elastic scattering data of polarized protons on several iron and nickel isotopes at energies ranging from 15 to 25 MeV. This potential is rather close to the Becchetti-Greenlees [2] potential except for the diffuseness of the spin-orbit part.

The deuteron potential was constructed from the Becchetti-Greenlees potentials [2] according to the prescription of Satchler [39], where the real well-depth potential has been decreased by 7.5%, while the imaginary potential has been increased by 50%.

For the triton, since there is no potential for ^{56}Ni, Polane *et al.* [33] [34] have extrapolated the potential of ^{54}Fe to ^{56}Ni and also applied an energy extrapolation to the potential according to the energy and symmetry dependence of the global triton potential of Becchetti-Greenlees.

In the DWBA calculations with the CHUCK3 code the neutron transfer amplitudes have to be normalized with empirical constants (zero-range normalization constant),

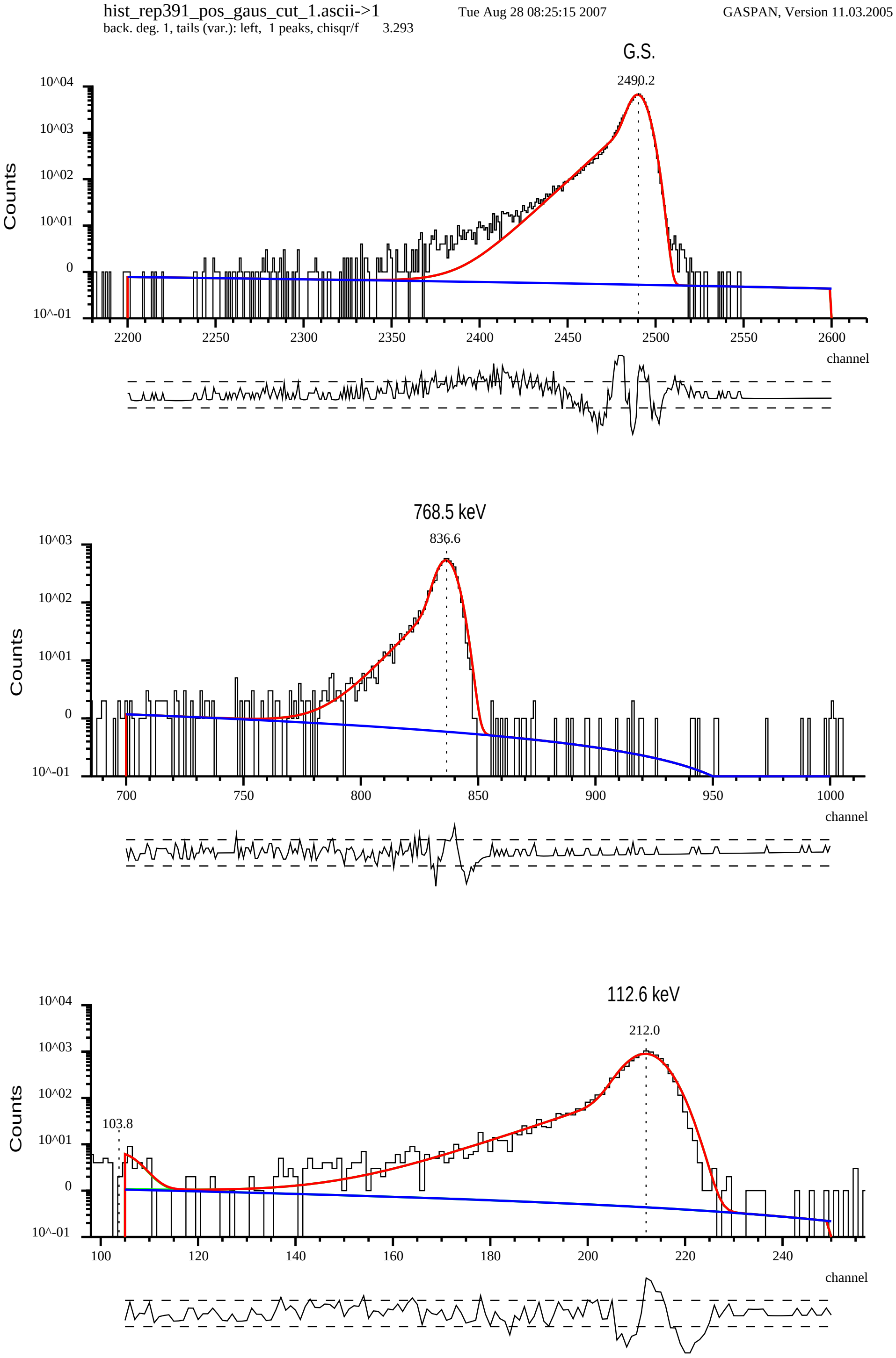

Figure 4.3.: An example for GASPAN fit for the Q3D focal plane spectrum for ^{57}Ni levels. The background was included in the fit with polynomial degree = 1. χ^2/N for the fit was around 1.1.

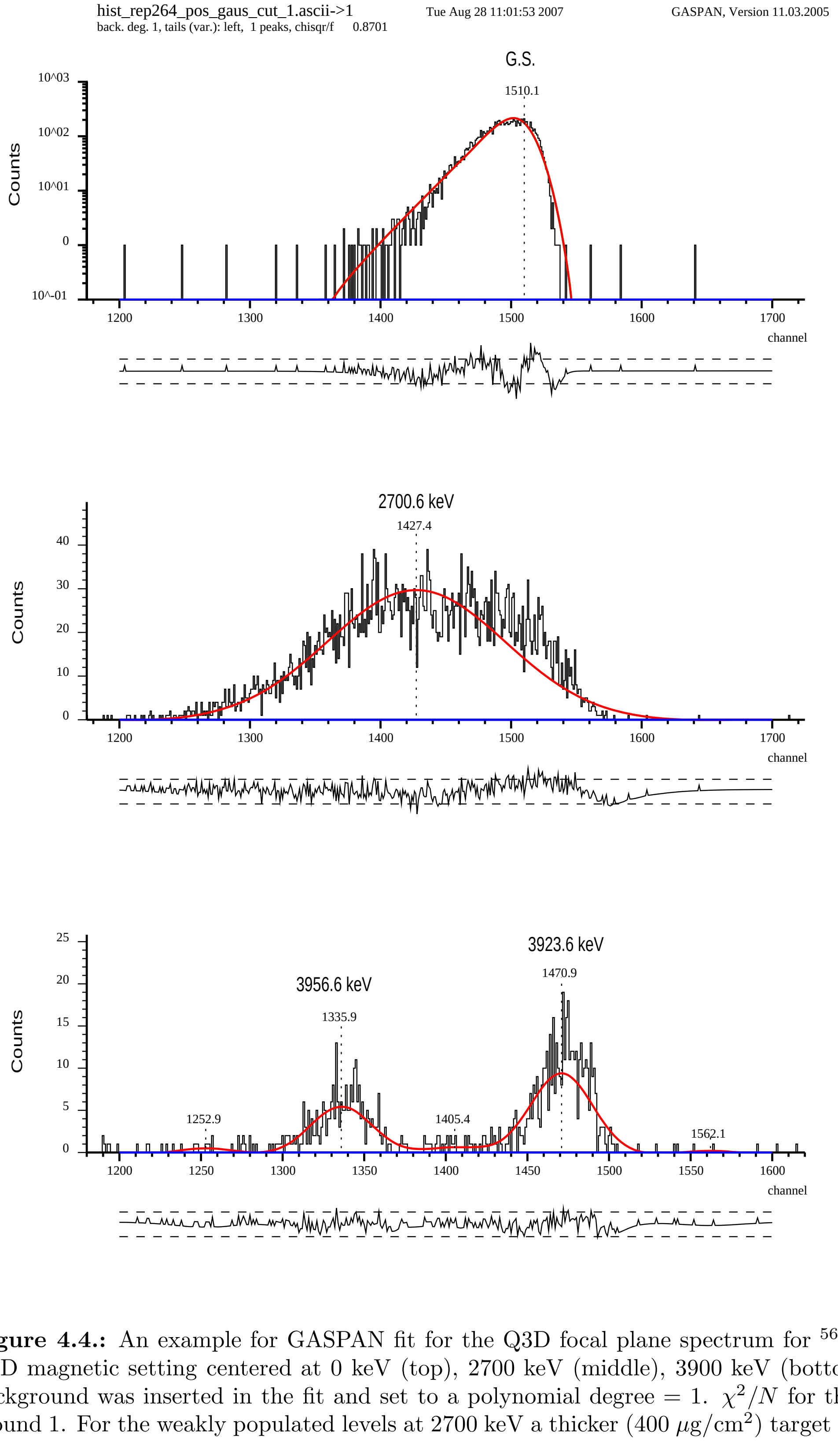

Figure 4.4.: An example for GASPAN fit for the Q3D focal plane spectrum for ^{56}Ni levels. Q3D magnetic setting centered at 0 keV (top), 2700 keV (middle), 3900 keV (bottom). The background was inserted in the fit and set to a polynomial degree = 1. χ^2/N for the fit was around 1. For the weakly populated levels at 2700 keV a thicker (400 μg/cm^2) target was used.

Potential		Real			Imaginary		
		V (MeV)	r_o (fm)	a_o (fm)	W (MeV)	r_I (fm)	a_I (fm)
Proton	Volume	-52.0	1.15	0.76	-2.45	1.35	0.47
	surface				6.7	1.35	0.47
	L.S	-5.6	1.04	0.54			
Deuteron	Volume	-98.4	1.17	0.78			
	surface				15.2	1.26	0.61
	L.S	-11.8	1.04	0.56			
Triton	Volume	-144.2	1.24	0.69	-34.1	1.43	0.87
	surface						
Neutron	Volume	1.00	1.25	0.65			

Table 4.1.: Optical-Model parameters used in DWBA calculations for (p,d) and (p,t) reaction, with beam energy of E_p^{lab} = 24.6 MeV, r_C = 1.25 fm for proton and triton, r_C = 1.30 fm for the deuteron.
Proton and Deuteron parameters from Polane *et al.* [33].
Triton parameters from Polane *et al.* [34].

	Non-locality parameter (β)					Finite-range parameter (R)	
	p	d	t	n		(p,d)	(p,t)
β	0.85	0.54	0.25	0.85	R	0.69	0.69

Table 4.2.: DWBA parameters for $^{58}\mathrm{Ni}(\vec{\mathrm{p}},\mathrm{t})^{56}\mathrm{Ni}$ reaction used in this work, from Polane *et al.* [34].

which are N_0(pd) = - 122.5 MeV fm$^{3/2}$ for the single neutron transfer, N_0(pt) = - 1560 MeV fm$^{3/2}$ for the two-neutron simultaneous transfer, N_0(pd) = - 122.5 MeV fm$^{3/2}$ and N_0(dt) = - 225.0 MeV fm$^{3/2}$ for the two-neutron sequential transfer.

4.2.4. $(\vec{\mathrm{p}},\mathrm{d})$ Reaction Model.

The data for the ^{57}Ni levels were analyzed using the same reaction model used in Polane *et al.* [33], Figure 4.5. The model consists of the one step (direct) transition (pd) from the ^{56}Ni ground state to ^{57}Ni levels (J^{π}) and the two-step transition (pp′d), where the inelastic one-way proton scattering to the first 2^+ state (1.454 MeV) in ^{58}Ni was included. Transitions were considered to happen by the pick-up of a $2p_{3/2}$, $2p_{1/2}$, $1f_{5/2}$ or $1f_{7/2}$ neutron.

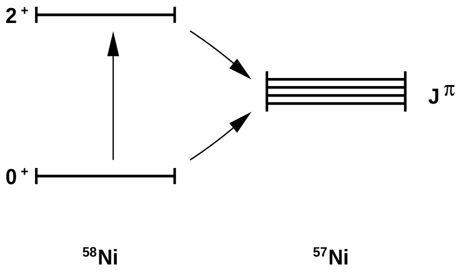

Figure 4.5.: Coupling scheme for the single neutron transfer reaction for the coupled-channels calculations. $J^{\pi} = 1/2^-, 3/2^-, 5/2^-$. From Polane *et al.* [33]

The same spectroscopic amplitudes used in Polane *et al.* [33] are used here and listed in Table 4.3. The situation in the (one- plus two-step) model is more complicated than the (direct) one-step model, since in the (one- plus two-step) model up to four spectroscopic amplitudes are needed for each level (J) compared to only one for the (direct) model. This is why Polane *et al.* used shell-model calculations done by Koops - Glaudemans [16] and Van Hees et al [17]. The first calculations (SD0) were restricted to $2p_{3/2}$, $2p_{1/2}$ and $1f_{5/2}$ nucleons (i.e. an inert ^{56}Ni core), where a second calculation (SD1) allows for one $1f_{7/2}$ nucleon hole in the ^{56}Ni core with particles occupying $2p_{3/2}$, $2p_{1/2}$ and $1f_{5/2}$ shells, Table 4.3. The same value for the deformation parameter β_2= - 0.22 is used here for the inelastic transition, where the sign of β_2 was found by trial and error.

Process	$J(j)$	SD0	SD1
$0^+ \rightarrow J$	5/2(5/2)	-0.78	-0.94
	3/2(3/2)	1.11	0.89
	1/2(1/2)	0.40	0.41
$2^+ \rightarrow 5/2^-$	5/2(1/2)	0.35	0.44
	5/2(3/2)	0.32	0.35
	5/2(5/2)	-0.42	-0.57
	5/2(7/2)	0.00	0.10
$2^+ \rightarrow 3/2^-$	3/2(1/2)	-0.42	-0.39
	3/2(3/2)	1.01	0.72
	3/2(5/2)	0.32	0.36
	3/2(7/2)	0.00	0.22
$2^+ \rightarrow 1/2^-$	1/2(3/2)	0.42	0.37
	1/2(5/2)	-0.35	-0.44

Table 4.3.: Spectroscopic amplitudes for the one-neutron transfer ^{58}Ni($\vec{\mathrm{p}}$, d)^{57}Ni reaction, where J is the angular momentum of the final state, j is the transferred angular momentum. From Polane *et al.* [33]

4.2.5. ($\vec{p}$, d) Results and Discussion.

The DWBA calculations were performed using the one step (direct) model and the coupled channel (one- plus two-step) model with (SD0) and (SD1) separately. The calculations were compared to the experiment and presented in Figure 4.6. No significant difference between (SD0) and (SD1) for the lower ^{57}Ni levels $J^{\pi} = 1/2^{-}, 3/2^{-}, 5/2^{-}$ was observed, which means no significant effect for the $1f_{7/2}$ shell in ^{57}Ni lower levels.

Also no significant difference between the (direct) and the coupled channel calculations is observed from Figure 4.6 which shows the levels angular distribution and analyzing power curves for the direct and the coupled channel calculations using (SD0) and (SD1) compared to the experiment. Therefore, we can deduce that the lower ^{57}Ni levels G.S., 0.768 and 1.112 MeV are mainly reached by the one-step (direct) transition. The two-step transition through ^{58}Ni 2^{+} state at 1.454 MeV, may dominate higher levels. This conclusion is similar to what is obtained by Polane *et al.* [33].

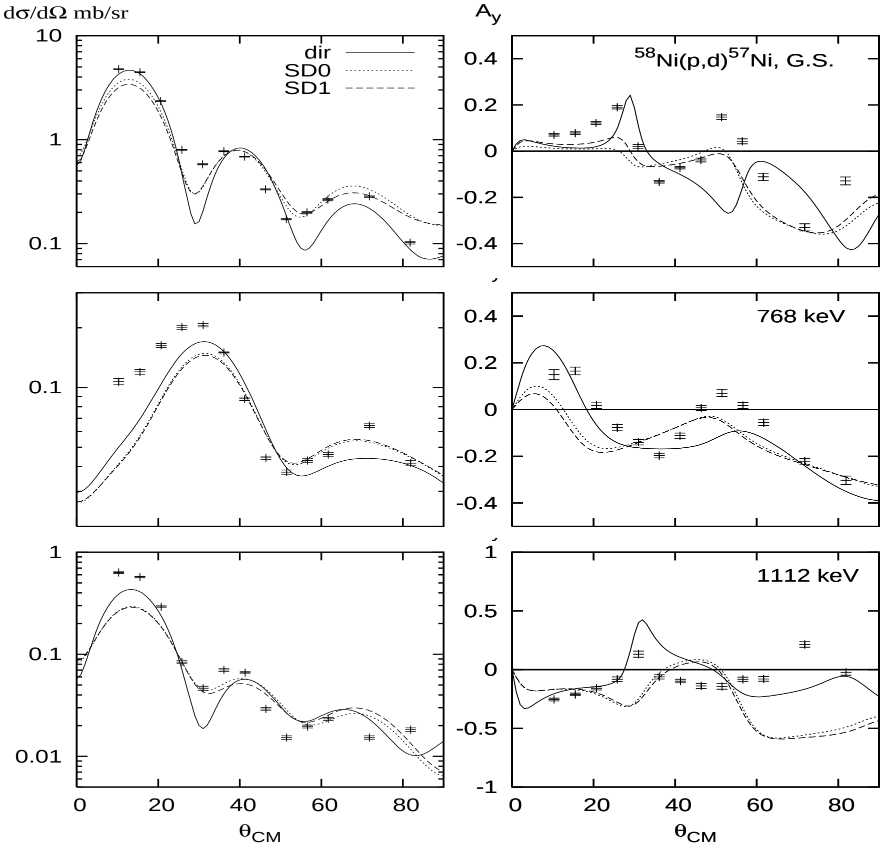

Figure 4.6.: Cross-sections and analyzing powers for the transitions to the first three levels of ^{57}Ni G.S., 0.768 and 1.112 MeV, populated by the (p,d) single-neutron pick-up reaction. E_p= 24.6 MeV. The full curves represent DWBA calculations using the one step (direct) model, dotted curve represent calculations using (one- plus two-step) model with the spectroscopic amplitudes (SD0), broken curve represent calculations using (one- plus two-step) model with the spectroscopic amplitudes (SD1).

4.2.6. $(\vec{\mathrm{p}},\mathrm{t})$ Reaction Model.

To obtain a suitable model for the $(\vec{\mathrm{p}},\mathrm{t})$ reaction we started with the model represented by Polane *et al.* [34], where they studied the ^{56}Ni G.S. only and assumed the ^{58}Ni nucleus to be consisting of an inert core of ^{56}Ni with closed $1f_{7/2}$ shell for proton and neutron plus two neutrons. So that the two transferred neutrons are removed from the $2p_{3/2}$, $2p_{1/2}$ and $1f_{5/2}$ shells only. We tried first to reproduce their results using the reaction model they used, then achieved some improvement by including the $1f_{7/2}$ shell in the calculations and deduced a reasonable reaction model.

The first model we tested is illustrated in Figure 4.7. It is just what Polane *et al.* considered for the ^{56}Ni ground state, but we extended it for the rest of the levels. In this model the one-way inelastic scattering to the 2^+ state at 1.454 MeV in ^{58}Ni is assumed to contribute in the reactions leading to all ^{56}Ni levels. Besides that the two-way inelastic scattering between the ^{56}Ni G.S. 2_1^+ level is included.

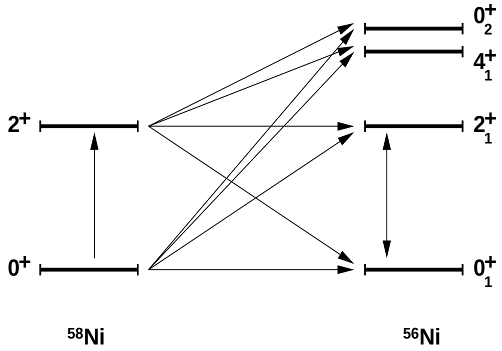

Figure 4.7.: Coupling scheme for the reaction $^{58}\mathrm{Ni}(\vec{\mathrm{p}},\mathrm{t})^{56}\mathrm{Ni}$ for the G.S., from J. H. Polane *et al* [34], where the inelastic proton excitation at 1.454 MeV is considered to contribute in transitions leading to all ^{56}Ni levels.

Because of the CHUCK3 limitation for the number of channels and couplings, the model above was first tested for simultaneous transfer only. The results are illustrated in Figure 4.8. This model gave acceptable results for the 0_2^+ level at 3.956 MeV, but it is clear (with the spectroscopic amplitudes we used) it fails for the rest of the levels. From this model we learned that the pathway through the 2^+ excitation in ^{58}Ni doesn't contribute to all ^{56}Ni levels, but maybe important for higher levels like the 0_2^+ level at 3.956 MeV.

After few attempts and because of the CHUCK3 limitation we considered the model illustrated in Figure 4.9, containing both simultaneous and sequential transfers. For the transitions leading to the ^{56}Ni G.S. 0_1^+ we considered scheme (A), which consists of the simultaneous one (direct) and two-step transitions (pt) and (pp′t), respectively, besides the sequential two and three-step transitions (pdt) and (pp′dt), respectively. For the transitions leading to the ^{56}Ni 2_1^+ level, we used scheme (B), where the inelastic proton excitation at 1.454 MeV seems to have a negligible contribution. Scheme (B) consists of the simultaneous one and two-step (pt′) and (ptt′) transitions, besides the sequential two and three-step transitions (pdt′) and (pdtt′), respectively. For the 4_1^+ level, scheme (B) is also used, but the 4_1^+ state seems to be reached mainly

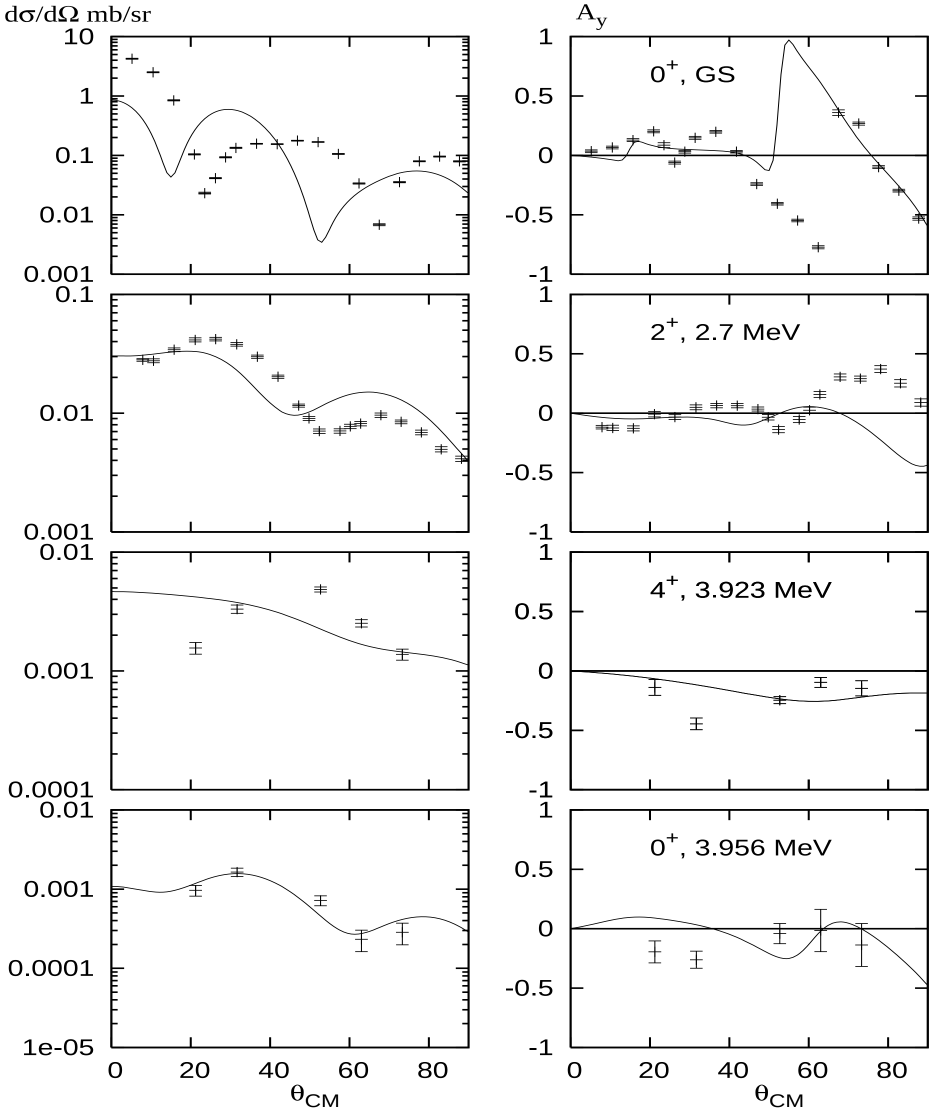

Figure 4.8.: DWBA calculations for ^{56}Ni levels applying Polane coupling scheme for the G.S., indicated in Figure 4.7, where the transitions through ^{58}Ni 2^+ state at 1.454 MeV is assumed to contribute in all ^{56}Ni levels (same scheme for all the states) and involving only the two-neutron simultaneous transfer to satisfy CHUCK3 limitation.

via the one-step (pt′) simultaneous transfer and the two-step (pdt′) sequential transfer without any effect from the ^{56}Ni ground state.
Transitions leading to the last observed level 0_2^+ are described by scheme (C), which is similar to scheme (A). In this scheme contributions from the lower ^{56}Ni levels are weak enough to be ignored.

Couplings and spectroscopic amplitudes ($S^{1/2}$) for the previous models are listed in Table 4.4 for the simultaneous transfer and Table 4.5 for the sequential transfer.

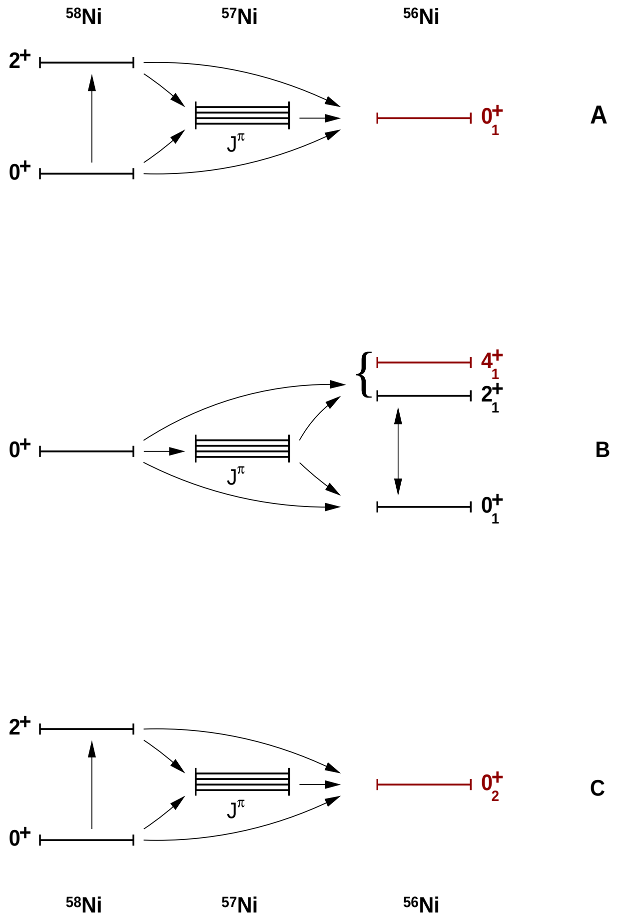

Figure 4.9.: Suggested coupling schemes in this work for the simultaneous and sequential two-neutrons transfer reaction for the DWBA calculations. Transition through ^{58}Ni 2^+ state at 1.454 MeV is assumed to contribute in ^{56}Ni ground state and 3.956 MeV state only. J^π are the ^{57}Ni levels $3/2^-, 5/2^-, 1/2^-, 7/2^-$ at 0.0, 0.768, 1.112, 2.577 MeV, respectively.

We used the same ($S^{1/2}$) values as Polane [34], but with estimating new values for couplings which include the $1f_{7/2}$ shell by trial and error. Here one would like to use input from modern large scale shell model calculations. However, such calculations are not available yet. Therefore, the ($S^{1/2}$) values for couplings to the ^{56}Ni levels 2_1^+, 4_1^+ and 0_2^+ at 2.7, 3.923 and 3.956 MeV, respectively, were set to 1 since there is also no experimental information available. This is indeed one of the most serious limitations for our study. The ($S^{1/2}$) signs were obtained by trial and comparison to the experimental data.

The deformation parameter $\beta_2(2^+; 1.454\text{MeV})$ = - 0.22 for the inelastic scattering in ^{58}Ni and the non-locality (β) and the finite-range (R) parameters, mentioned in Table 4.2 were taken from Polane *et al.* [34]. The $\beta_2(2_1^+; 2.7\text{MeV})$ = + 0.133 for the inelastic scattering in ^{56}Ni is taken from the primary value + 0.173 from S. Raman *et al.* [36], then adjusted by tray and comparison to the experimental data.

Process (pt) & (p′t)	L	(j_1, j_2)	$S^{1/2}$	Process (pt′)	L	(j_1, j_2)	$S^{1/2}$	Process (pt′)	L	(j_1, j_2)	$S^{1/2}$	Process (pt′) & (p′t′)	L	(j_1, j_2)	$S^{1/2}$
$0^+ \rightarrow 0_1^+$	0	(7/2,7/2)	-0.55	$0^+ \rightarrow 2_1^+$	2	(7/2,7/2)	1.0	$0^+ \rightarrow 4_1^+$	4	(7/2,7/2)	1.0	$0^+ \rightarrow 0_2^+$	0	(7/2,7/2)	1.0
		(5/2,5/2)	-0.55*			(7/2,5/2)	1.0			(7/2,5/2)	1.0			(5/2,5/2)	1.0
		(3/2,3/2)	-0.78*			(7/2,3/2)	1.0			(7/2,3/2)	1.0			(3/2,3/2)	1.0
		(1/2,1/2)	-0.28*			(7/2,1/2)	1.0			(7/2,1/2)	1.0			(1/2,1/2)	1.0
						(5/2,5/2)	1.0			(5/2,5/2)	1.0				
$2^+ \rightarrow 0_1^+$	2	(7/2,7/2)	0.15			(5/2,3/2)	1.0			(5/2,3/2)	1.0	$2^+ \rightarrow 0_2^+$	2	(7/2,7/2)	1.0
		(7/2,5/2)	0.75			(5/2,1/2)	1.0							(7/2,5/2)	1.0
		(7/2,3/2)	0.01			(3/2,3/2)	1.0							(7/2,3/2)	1.0
		(7/2,1/2)	0.50			(3/2,1/2)	1.0							(7/2,1/2)	1.0
		(5/2,5/2)	-0.30*											(5/2,5/2)	1.0
		(5/2,3/2)	-0.32*											(5/2,3/2)	1.0
		(5/2,1/2)	0.36*											(5/2,1/2)	1.0
		(3/2,3/2)	-0.71*											(3/2,3/2)	1.0
		(3/2,1/2)	-0.42*											(3/2,1/2)	1.0

Table 4.4.: Spectroscopic amplitudes for simultaneous two-neutron transfer used for the ^{58}Ni($\vec{p}$, t)^{56}Ni reaction.
* from Polane *et.al* [34].
$0^+, 2^+$ are the ^{58}Ni G.S. and 1.454 MeV levels, respectively.
$0_1^+, 2_1^+, 4_1^+$ and 0_2^+ are the ^{56}Ni G.S., 2.7, 3.923 and 3.956 MeV levels, respectively.
(j_1, j_2) are the transferred angular momenta by the first and second neutron.

Process (pd) & (p′d)	$J(j)$	$S^{1/2}$	Process (dt)	$J(j)$	$S^{1/2}$	Process (dt′)	$J(j)$	$S^{1/2}$	Process (dt′)	$J(j)$	$S^{1/2}$	Process (dt′)	$J(j)$	$S^{1/2}$
$0^+ \rightarrow J$	7/2(7/2)	0.98	$J \rightarrow 0_1^+$	7/2(7/2)	-1.0	$J \rightarrow 2_1^+$	7/2(7/2)	1.0	$J \rightarrow 4_1^+$	7/2(7/2)	1.0	$J \rightarrow 0_2^+$	7/2(7/2)	1.0
	5/2(5/2)	-0.73*		5/2(5/2)	1.0*		7/2(5/2)	1.0		7/2(5/2)	1.0		5/2(5/2)	1.0
	3/2(3/2)	0.95*		3/2(3/2)	-1.0*		7/2(3/2)	1.0		7/2(3/2)	1.0		3/2(3/2)	1.0
	1/2(1/2)	0.35*		1/2(1/2)	-1.0*		5/2(7/2)	1.0		7/2(1/2)	1.0		1/2(1/2)	1.0
							5/2(5/2)	1.0		5/2(7/2)	1.0			
$2^+ \rightarrow J$	7/2(7/2)	0.41					5/2(3/2)	1.0		5/2(5/2)	1.0			
	5/2(5/2)	-0.39*					5/2(1/2)	1.0		5/2(3/2)	1.0			
	5/2(3/2)	0.30*					3/2(7/2)	1.0		3/2(7/2)	1.0			
	5/2(1/2)	0.31*					3/2(5/2)	1.0		3/2(5/2)	1.0			
	3/2(5/2)	0.28*					3/2(3/2)	1.0		1/2(7/2)	1.0			
	3/2(3/2)	0.87*					3/2(1/2)	1.0						
	3/2(1/2)	-0.36*					1/2(5/2)	1.0						
	1/2(5/2)	-0.31*					1/2(3/2)	1.0						
	1/2(3/2)	0.37*												

Table 4.5.: Spectroscopic amplitudes for sequential two-neutron transfer used in $^{58}\mathrm{Ni}(\vec{\mathrm{p}},\mathrm{t})^{56}\mathrm{Ni}$ reaction.
* from Polane *et.al* [34].
J is the angular momentum of the intermediate state; j is the transferred angular momentum.

4.2.7. ($\vec{\mathrm{p}}$, t) Results and Discussion.

DWBA calculations were performed first assuming ^{56}Ni as a good doubly magic nucleus with well closed $1f_{7/2}$ shell for protons and neutrons as in J. H. Polane *et al.* [34], second assuming ^{56}Ni not a good doubly magic nucleus and treating the $1f_{7/2}$ as broken shell by involving couplings to and from it in the calculations. The DWBA results from those assumptions for the G.S. are plotted in Figure 4.10. The top one shows the result from the simultaneous transfers only, while the lower one shows the result from sequential transfers only. From both figures we notice some improvement by involving the $1f_{7/2}$ shell in the calculation. The shape of the analyzing power is improved by involving transitions via the $1f_{7/2}$ shell. A well separated double peak structure at 20° & 36° appears with including $1f_{7/2}$, which fits better with the experimental data, while ignoring the $1f_{7/2}$ shell produced a broad peak for both simultaneous and sequential cases.

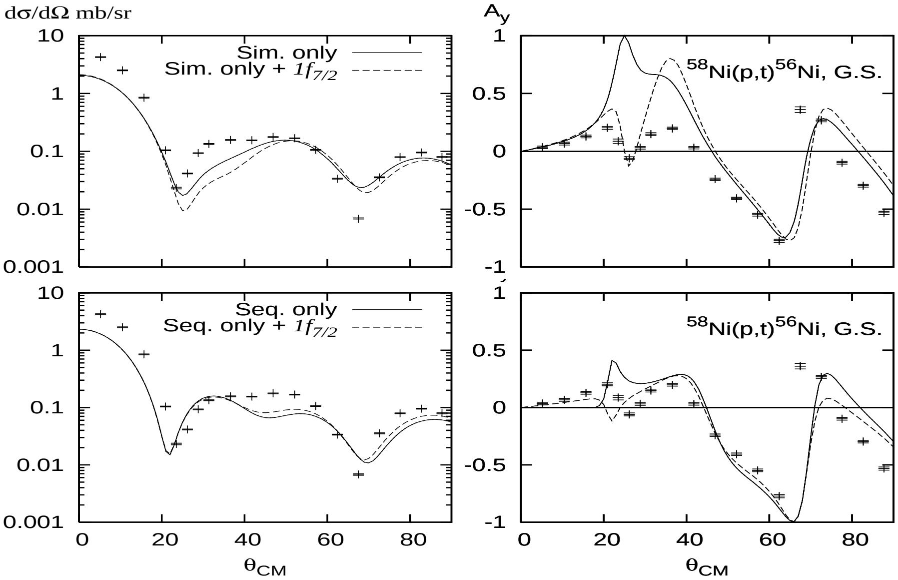

Figure 4.10.: DWBA calculations using the two-neutron simultaneous transfer only ($\lambda = 1,\ \mu = 0$) (top) and sequential transfer only ($\lambda = 0,\ \mu = 1$) (bottom) for ^{56}Ni G.S. E$_{\mathrm{p}}$= 24.6 MeV. Calculations ignoring $1f_{7/2}$ shell are presented with a full curve and including the $1f_{7/2}$ shell with a broken curve. The calculations are performed considering the coupling scheme indicated in Figure 4.9 (A).

Our results show it is indeed necessary to include the $1f_{7/2}$ in the calculation for both simultaneous and sequential two-neutron transfer.

Since the two-neutron transfer is more likely to occur by both types of transitions, an input file was inserted to the code CHUCK3 including both of the transitions. The result is presented in Figure 4.11. Such simple collection of the couplings, with one to one ratio between simultaneous and sequential transfers, reproduced the experimental cross-section curve pretty well, but not the analyzing power. So that we tried to use a combination of simultaneous and sequential with different ratios. Such a combination of simultaneous and sequential transfer, can also provide information about the purity

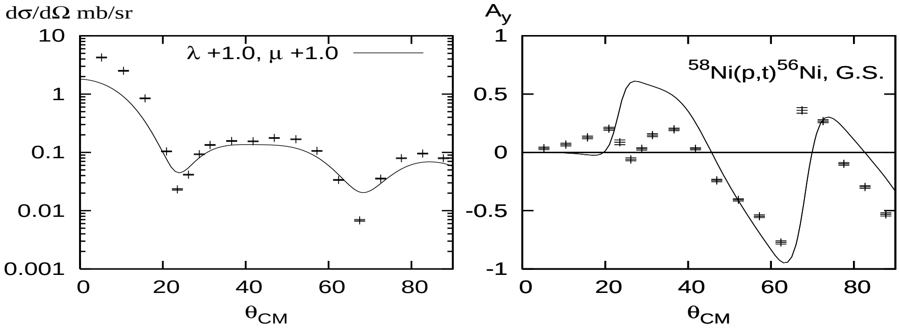

Figure 4.11.: DWBA calculations for ^{56}Ni 0^+ GS compared to the experiment including simultaneous and sequential transfers with the same ratio.

of the ^{56}Ni ground state wave function with respect to a closed $1f_{7/2}$ shell. If it has a well closed shell, the dominance of one type should be observed (sequential), but if it is a mixture of closed and particle hole excitation, a combination of both transitions should describe the angular distributions for the ^{56}Ni levels better.

Calculations by the CHUCK3 code were performed considering the coupled channels schemes indicated in Figure 4.9 and including both types of transitions in the same input file. The simultaneous transition amplitudes were normalized with the factor λ and sequential transition amplitudes with the factor μ. Decreasing the ratio of λ against μ will make the sequential transfer stronger and vice versa.

One now can determine the ratio of λ to μ from fitting the resulting angular distribution of the cross-section to that obtained experimentally. Since we were interested in the relative sign of the simultaneous- and sequential-transfer amplitudes, we also looked into negative values of λ/μ. Using the chi-squared χ^2/N test between the DWBA results and the experimental cross-section angular distribution curves to indicate the quality of the fits. In ref: [34] they preferred to do the χ^2/N fit for the analyzing power (A_y) curves where they studied the ground state only. But because we are studying few higher levels too, whose theoretical A_y does not agree too much with the experiment, we prefer to use the χ^2/N fit for the cross-section angular distribution curves. The χ^2/N value gives some guidance, but to select the best combination of λ/μ we also took the A_y curves into account.

Figure 4.12 shows the calculations for the ^{56}Ni 0^+ ground state using the coupled channels scheme A indicated in Figure 4.9, first considering $\lambda > \mu$, second considering $\lambda < \mu$. The $\lambda > \mu$ (Sim. > Seq.) assumption can not reproduce the broad peak for the angular distribution between 20° & 40° nor the double peak structure with the similar heights for the analyzing power at 20° & 36°, which is better reproduced for the case with $\lambda < \mu$ (Sim. < Seq.). Also the $\lambda < \mu$ (Sim. < Seq.) assumption shows a better χ^2/N value for the fit with the experimental data, Table 4.6.

From Figure 4.12 one can see that the G.S. angular distribution is fitted better using the $\lambda =$ -0.1 and $\mu =$ -0.5 combination, where the experimental cross-section curve and especialy the analyzing power curve are better presented. Some other combinations performed for the ^{56}Ni 0^+ ground state are presented in Figure 4.13 (top). The resulting χ^2/N values for such combinations are given in Table 4.6.

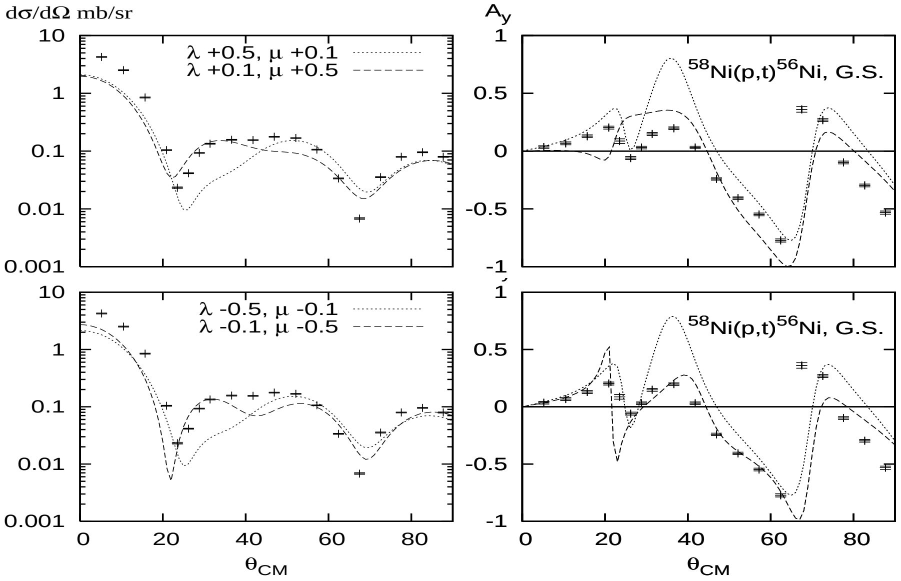

Figure 4.12.: Calculations for ^{56}Ni 0^+ GS, with $\lambda > \mu$ (dotted curve) and with $\lambda < \mu$ (broken curve). Regardless the coupling signs, the λ = - 0.1 and μ = - 0.5 combination show better agreement with the experiment for both cross-section and analyzing power curves.

The previous steps were applied to the rest of ^{56}Ni levels, 2_1^+, 4_1^+ and 0_2^+ at 2.7, 3.923 and 3.956 MeV, respectively, Figure 4.13, where a valuable number of λ : μ combinations were tested for each level, but only the important results are presented here.

From the χ^2/N values listed in Table 4.6, $\lambda < \mu$ was found to be the common case for most of the levels. This means the two-neutron sequential transfer is the dominant beside a necessity of a contribution from the simultaneous transfer.

Finally we should indicate that the calculations strongly depend on the used spectroscopic amplitudes. Maybe if we have better and well calculated values for couplings involving the $1f_{7/2}$ shell we could confirm this result more or rather deny it. Also we should indicate that this combinations for λ & μ could not be unique.

The same discussion about λ to μ *(sim. to seq. ratio)* was presented before by J. H. Polane *et al.* [34] but only for the ground state. The best ratios they had were λ = 0.53, μ = 0.78 with χ^2/N =25 and λ = - 0.22, μ = 0.97 with χ^2/N =154 for the ground state, which agree with our conclusion of the sequential transfer dominance. From the previous results we deduced that the inclusion of the $1f_{7/2}$ shell in the calculations is important, which is consistent with a partially broken $1f_{7/2}$ shell in the ground state wave function of ^{56}Ni.

^{56}Ni level	λ	μ	χ^2/N
0_1^+, G.S.	Dir.		1170
	+1.0	+1.0	456
	-0.5	-0.1	807
	-0.1	-0.5	534
	+0.5	-0.1	804
	+0.53	-0.78	458
	-0.3	-0.9	536
	-0.3	-0.85	534
2_1^+, 2.7 MeV	Dir.		141
	+1.0	+1.0	157
	+0.3	-0.9	157
	-0.3	-0.9	126
	-0.3	-1.0	121
4_1^+, 3.923 MeV	Dir.		57
	+1.0	+1.0	66
	+0.5	+0.3	58
	+1.0	+0.3	58
0_2^+, 3.956 MeV	+1.0	+1.0	6.4
	+0.1	+0.85	12.0
	+0.3	-0.85	7.7
	+0.3	-0.5	6.1

Table 4.6.: χ^2/N values for the fit between the he DWBA results and the experimental cross-section angular distribution curves for some λ:μ combinations we tested for the observed ^{56}Ni levels.

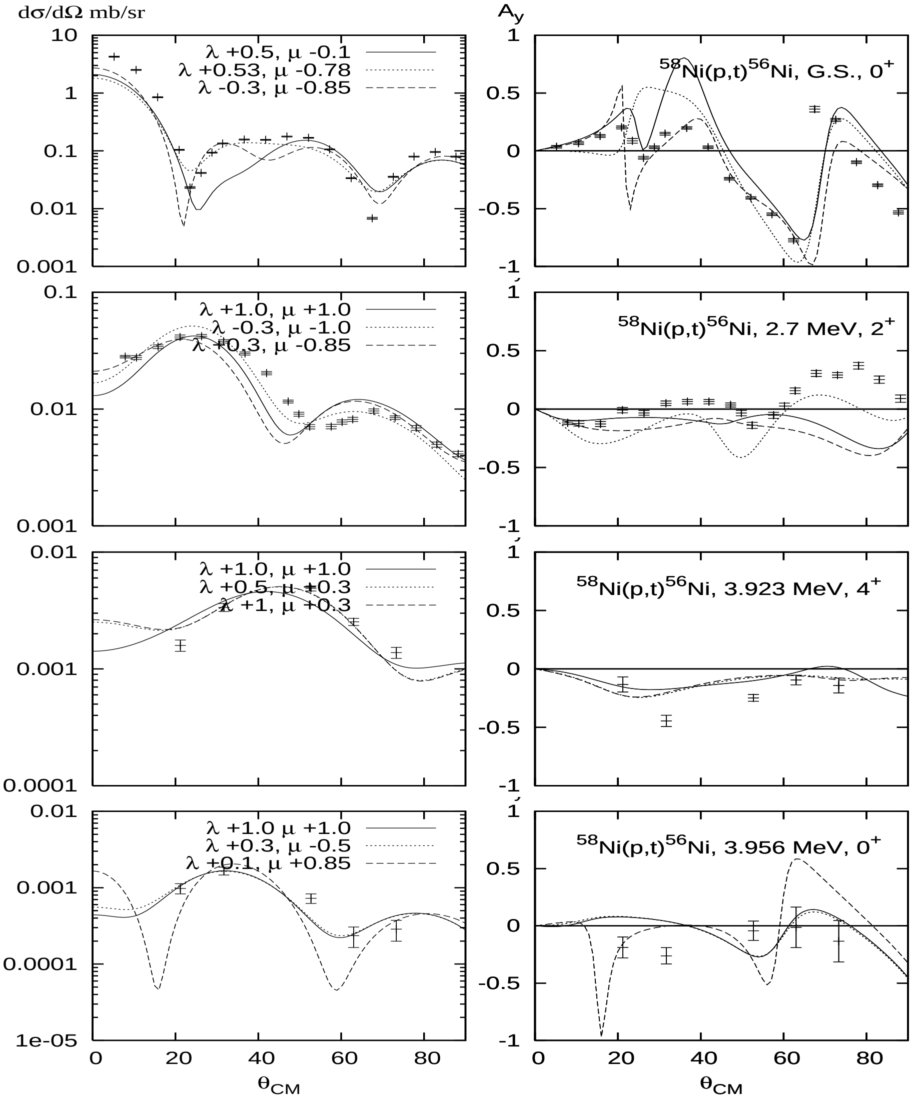

Figure 4.13.: Some of $\lambda/\ \mu$ combinations for ^{56}Ni, 0_1^+, 2_1^+, 4_1^+ and 0_2^+ levels. Most of the time $\lambda < \mu$ shows better agreement with the experiment, Table 4.6. Calculations performed using the coupling schemes indicated in Figure 4.9. Scheme (A) for ^{56}Ni ground state, scheme (B) for 2.7, 3.923 MeV states and scheme (C) for 3.956 MeV state.

4.3. Inverse Kinematics Reaction $\mathrm{t}(^{40}\mathrm{Ar},\mathrm{p})^{42}\mathrm{Ar}$

After studying the two-neutrons transfer in normal kinematic in the previous Section 4.2, it is time to investigate the two-neutron transfer in inverse kinematics to satisfy the second goal of this thesis, which is testing the reliability of inverse kinematics reactions to study exotic nuclei. In the past, when triton beams were readily available at several accelerator facilities, (t,p) reaction were a very useful tool to reach more neutron-rich nuclei. Also for nuclei far off stability the (t,p) reaction may be a very useful tool to populate even more neutron-rich nuclei and to study pairing correlations and shape coexistence. However, this requires the use of a triton target and reactions in inverse kinematics. In order to test the capability of using (t,p) reactions with radioactive beams, we performed a test experiment at the Hahn-Meitner Institute Berlin, where a handling permit exists for tritium targets. For convenience of accelerator operations and the fact that the reaction was previously studied, we used the $\mathrm{t}(^{40}\mathrm{Ar},\mathrm{p})^{42}\mathrm{Ar}$ reaction. In this way we could test the capability of the inverse kinematics reaction and compare the results to the known results paving the way to extend our future studies to nuclei far off stability.

4.3.1. Experimental Procedures for the (t,p) Reaction.

Because of the high activity of the triton target (26.6 GBq) the $\mathrm{t}(^{40}\mathrm{Ar},\mathrm{p})^{42}\mathrm{Ar}$ reaction was performed at the HMI Berlin. A beam of ^{40}Ar was accelerated by the HMI Cyclotron to a lab energy $\mathrm{E}^{\mathrm{lab}}_{^{40}\mathrm{Ar}} = 2.16$ A MeV, which corresponds to a lab energy for a triton beam of $\mathrm{E}^{\mathrm{lab}}_{\mathrm{t}} = 6.499$ MeV in normal kinematic. The target consisted of a 440 μg/cm^2 thick tritium loaded titanium foil with the ratio Ti:t = 1:1.76, containing 48 μg/cm^2 tritons.

In an experiment using the method of elastic recoil detection (ERD) at the MLL Garching and using a deuterated Ti foil, we were able to show that such targets show no sign of hydrogen evaporation up to beam current of 1 particle nA. Therefore, we limited the beam current of ^{40}Ar to 0.6 nA.

A 500 μm thick Double Sided Silicon Strip Detector (DSSSD) was used to detect the outgoing protons from the (t,p) reaction, Section 2.3.2. The DSSSD was positioned 30 mm upstream of the target, Figure 4.14. In this way it covered an angular range from 129.6° → 158.4° in the lab-system, which corresponds roughly to the angular range ∼ 10° → 30° in the CM-system. In this way we are able to compare our results with the results by E. R. Flynn *et al.* [8], since they preformed the same reaction in normal kinematics using a higher beam energy of $\mathrm{E}^{\mathrm{lab}}_{\mathrm{t}} = 20$ MeV and covered the angular range ∼ 10° → 70° in the CM-system.

With our angular range we were able to distinguish between $l = 0$, 1 & 2 transitions but not $l = 3$, 4, 5 & 6 since their angular distributions are too similar in the angular range covered by the DSSSD.

To protect the DSSSD, a 1 mg/cm^2 thick Mylar shielding foil was placed in front of the DSSSD, which is sufficient to stop all back scattered ^{40}Ar particles with a maximum energy of 0.05 A MeV. Due to the shielding the proton energy is reduced by 6%.

To select only the events from the (t,p) reaction and since the HMI cyclotron produces beam pulses with a repetition rate of 10 MHz, the events were collected within a time

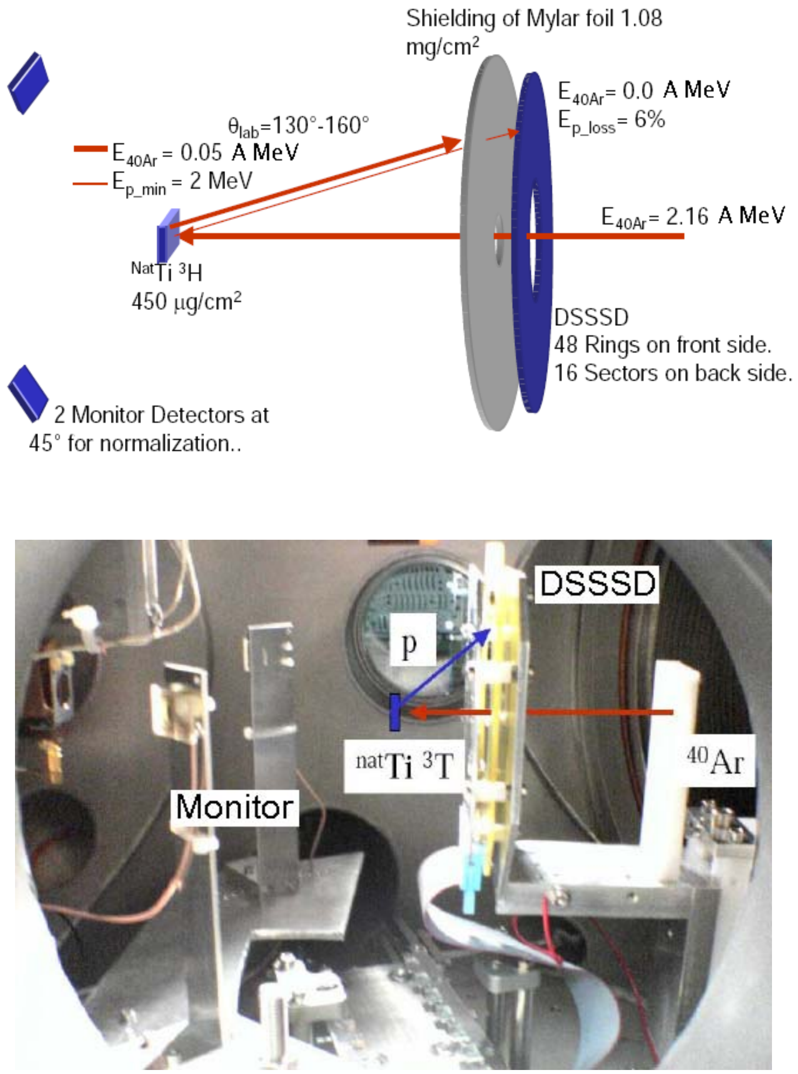

Figure 4.14.: The DSSSD set up in the target chamber for the $t(^{40}Ar, p)^{42}Ar$ reaction. $E^{lab}_{^{40}Ar}$ = 2.16 A MeV.

window of 90 ns, with delay time of about 56 ns, in regard to the beam time of flight.

Two monitor detectors were placed in the reaction chamber to monitor the reaction during the beamtime and to detect elastically scattered tritons for the determination of the luminosity, needed to deduce absolute differential cross-sections as explained previously in Section 3.2.3. The monitor detectors were 126 mm away from the target and positioned at $\theta_{\text{Mon.}} = (45°)_{\text{lab}} = (90°)_{\text{CM}}$ each. At this angle elastically scattered particles can be observed and well separated as shown by a kinematics calculation previously performed using the program Kine [16]. Figure 4.15 shows the monitor spectrum where the elastically scattered triton peak is identified.

Data were collected during 5 runs amounting to a time of 11:38 hours. The reaction cross-section was measured for each ring of the DSSSD, from which the angular dis-

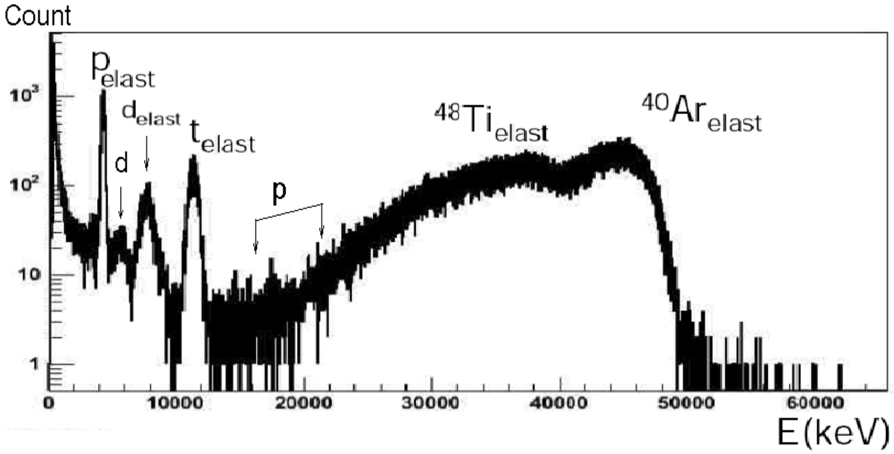

Figure 4.15.: The Monitor spectrum from the $t(^{40}Ar,p)^{42}Ar$ reaction at $E^{lab}_{^{40}Ar} = 2.16$ A MeV.

tributions were extracted and the transferred angular momentum was estimated. No parity information could be obtained because no polarized beam or polarized target was used. The $d(^{40}Ar,p)^{41}Ar$ reaction was also studied using a deuterium target under the same condition.

4.3.2. Analysis

The analysis followed the same procedures as for the single neutron transfer (d,p) reaction, Section 3.2.3. The program Gaspan [38] was used to fit the sum spectrum of the runs, Figure 4.16. In Gaspan the peak tail was set as a left type with amplitude and decay constant around 1% and 25, respectively. Tails were included in the peak fit. The background had a fixed value of 1 count/channel. The peaks width was set to 25.52 ± 0.25 channels $\simeq$ 200 keV. The χ^2/N for the fit was around 1.5. The energy calibration was done by giving Gaspan a calibration file, where some well known peaks are listed with their channel numbers and their energy values from the nuclear data sheets, besides a degree for the fit polynomial. An example for the Gaspan fit and the energy calibration is shown in Figure 4.16.

The experimental angular distributions were compared to the DWBA calculations utilizing the coupled channel code CHUCK3 [23] using the C. M. Perey & F. G. Perey [32] OM-potentials. The set of OM potential parameters by C. M. Perey & F. G. Perey [32] was determined by fitting elastic-scattering angular distributions for various incident particles and energies.

Applying the OM parameters from Perey & Perey for the OM-potential in the DWBA calculations did not produce results that agree with the experiment. This discrepancy is likely due to the low energy of the reaction for which an extrapolation of the parameters is not reliable. Therefore, an adjusted set of OMP was used beside the original one to compare the experimental results. In the adjusted set the triton (input channel) volume imaginary potential (W) was decreased 15%, while the proton (output channel) volume real potential V_r was increased 29%. Tables 4.7 and 4.8 shows the original and

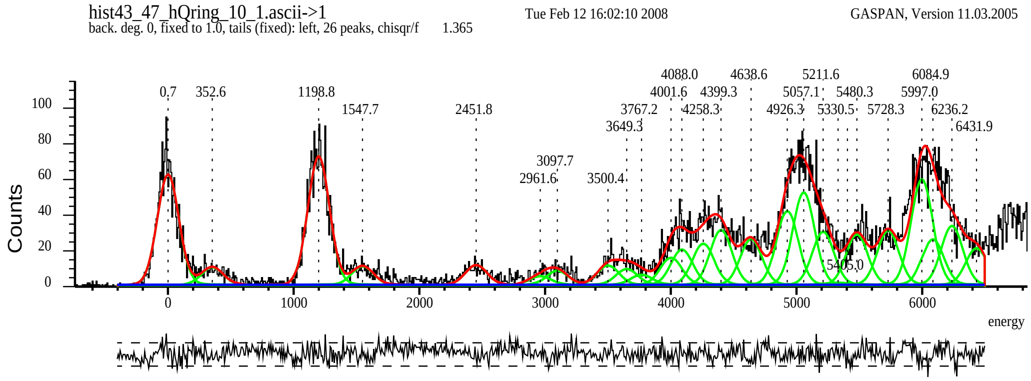

Figure 4.16.: A spectrum of a single ring of the DSSSD, ring 10, from the reaction $t(^{40}Ar, p)^{42}Ar$ at $E^{lab}_{^{40}Ar} = 2.16$ A MeV. The lower part of the figure shows the difference between the fit and the data, normalized with the error of the data.

the adjusted OMP sets respectively. The Coulomb radius was taken as $r_C = 1.25$ fm for proton and neutron and $r_C = 1.30$ fm for the triton.

The same values for the non-locality (β) and r_c used in the $^{58}Ni(\vec{p}, t)^{56}Ni$ reaction were used here, except for the finite-range (R) parameter it was set to zero, Table 4.9. The same steps in analyzing the experimental data as in Section 3.2 were followed here.

4.3.3. (t, p) Reaction Model.

The low-lying transitions for the $t(^{40}Ar, p)^{42}Ar$ reaction were considered basically as $(f_{7/2})^2$ transfers as argued in E. R. Flynn *et al.* [8], where they considered the transitions as a direct one step two-neutron transfer. Following the same assumption here with the DWBA calculations didn't provide us with acceptable results especially for the 0^+ ground state and the 2^+ state at 1198.8 (1208.2) keV. For that the one way inelastic scattering to the first 2^+ state in ^{40}Ar at 1.46 MeV were included in the DWBA calculations, Figure 4.17. Considering the previous scheme significantly improved the agreement between DWBA and experiment, see Figures 4.18 and 4.19.

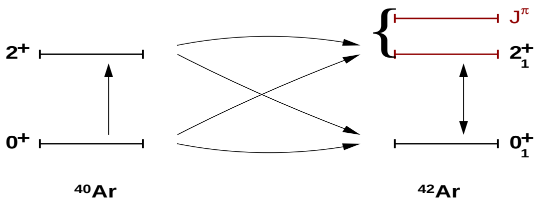

Figure 4.17.: The suggested coupling schemes in this work for the two-neutrons transfer reaction for the DWBA calculations, transition through ^{40}Ar 2^+ state at 1.46 MeV is assumed to contribute in all ^{42}Ar states.

Potential		Real			Imaginary		
		V (MeV)	r_o (fm)	a_o (fm)	W (MeV)	r_I (fm)	a_I (fm)
Triton	Volume	-163.26	1.2	0.72	-32.86	1.4	0.84
	surface						
	L.S	-2.5	1.2	0.72			
Proton	Volume	-54.53	1.25	0.65			
	surface				13.5	1.25	0.47
	L.S	-7.5	1.25	0.47			
Neutron	Volume	-1.	1.3	0.66			
	surface				9.17	1.25	0.48

Table 4.7.: OMP from Perey & Perey for $t(^{40}\mathrm{Ar},p)^{42}\mathrm{Ar}$ at $E^{\mathrm{lab}}_{^{40}\mathrm{Ar}} = 2.16$ A MeV, which corresponds to a lab energy for a triton beam of $E^{\mathrm{lab}}_{\mathrm{t}} = 6.499$ MeV in normal kinematic.

Potential		Real			Imaginary		
		V (MeV)	r_o (fm)	a_o (fm)	W (MeV)	r_I (fm)	a_I (fm)
Triton	Volume	-163.26	1.2	0.72	-27.86	1.4	0.84
	surface						
	L.S	-2.5	1.2	0.72			
Proton	Volume	-70.53	1.25	0.65			
	surface				13.5	1.25	0.47
	L.S	-7.5	1.25	0.47			
Neutron	Volume	-1.	1.3	0.66			
	surface				9.17	1.25	0.48

Table 4.8.: Adjusted OMP from Perey & Perey for $t(^{40}\mathrm{Ar},p)^{42}\mathrm{Ar}$ at $E^{\mathrm{lab}}_{^{40}\mathrm{Ar}} = 2.16$ A MeV, which corresponds to a lab energy for a triton beam of $E^{\mathrm{lab}}_{\mathrm{t}} = 6.499$ MeV in normal kinematic.

The deformation parameter for the inelastic scattering in ^{40}Ar $\beta_2(2^+; 1.46\mathrm{MeV}) = +\,0.251$ and for the inelastic scattering in ^{42}Ar $\beta_2(2^+_1; 1.208\mathrm{MeV}) = +\,0.205$ are taken from the primary value $\beta_2(2^+; 1.46\mathrm{MeV}) = +0.251$ and $\beta_2(2^+_1; 1.208\mathrm{MeV}) = +\,0.275$ from S. Raman *et al.* [36], then adjusted by trial and comparison to the experimental data.

Spectroscopic amplitudes in CHUCK3 were set to 1 for all couplings since no theoretical calculations discussing sequential or simultaneous two-neutron transfer reaction were performed for the reaction $t(^{40}\mathrm{Ar},p)^{42}\mathrm{Ar}$. This explains the $S > 1$ values for some

	Non-locality parameter (β)				Finite-range parameter (R)
	t	p	n		(p,t)
β	0.25	0.85	0.85	R	0.00
r_c	1.3	1.25	1.25		

Table 4.9.: DWBA parameters for $t(^{40}\mathrm{Ar},p)^{42}\mathrm{Ar}$ reaction used in this work, from Polane *et al.* [34].

of the levels in Tables 4.10 and 4.11.

4.3.4. Results

Same procedures were followed here as in the one-neutron transfer reaction in inverse kinematics, Section 3.2.4. Differential cross-section $\frac{d\sigma}{d\Omega}$ were calculated for each ring of the DSSSD separately, from which the angular distributions for ^{42}Ar levels were determined and compared to the DWBA calculations using the two OM-parameter sets presented in Tables 4.7 & 4.8. For all low-lying transitions into ^{42}Ar the transfer of a $(f_{7/2})^2$ pair was assumed. It was possible to identify levels with $l_{\mathrm{trans.}} \leq 2$, but it is hard to distinguish between $l_{\mathrm{trans.}} = 3, 4, 5$ & 6, since the characteristic dips of the angular distributions lay out of the DSSSD range. In total 21 levels of ^{42}Ar were observed in the energy range from 0.0 to 6236 keV. Good agreement between the experimental cross-section and DWBA calculation angular distribution curves was obtained in general, especially after considering the coupling scheme illustrated in Figure 4.17 in the DWBA calculations.

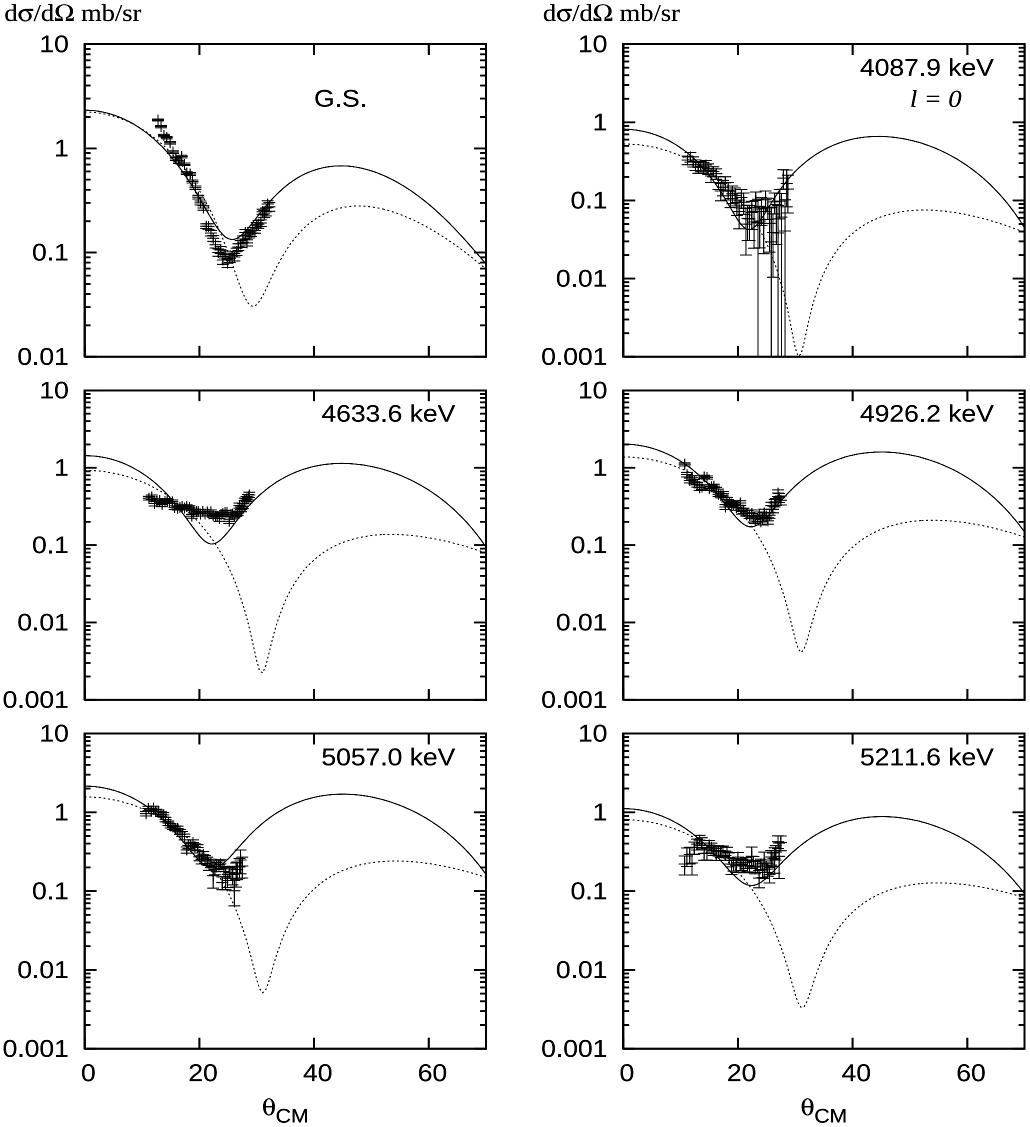

Figure 4.18.: The angular distributions for ^{42}Ar levels from the reaction t(^{40}Ar, p)^{42}Ar, $E^{\mathrm{lab}}_{^{40}\mathrm{Ar}}$= 2.16 A MeV, for $l = 0$ transfer. Curves indicate the DWBA calculations by CHUCK3 using the original OM parameters from C. M. Perey and F. G. Perey [32] presented in Table 4.7 (dotted line) and using the adjusted OM parameters of C. M. Perey and F. G. Perey presented in Table 4.8 with the reaction scheme presented in Figure 4.17 the (solid line).

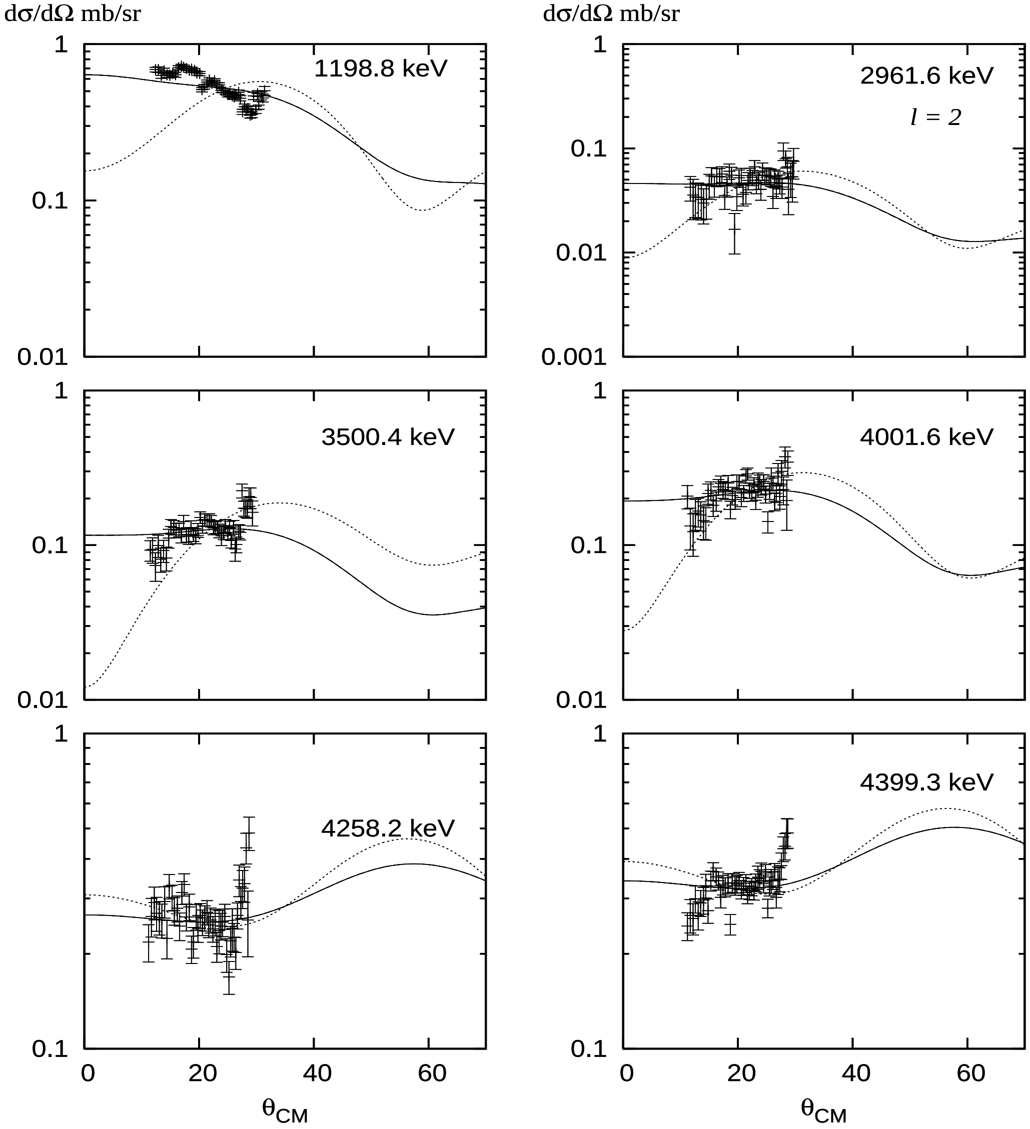

Figure 4.19.: The angular distributions for ^{42}Ar levels from the reaction $t(^{40}Ar, p)^{42}Ar$, $E^{lab}_{^{40}Ar}$= 2.16 A MeV, for $l = 2$ transfer. Curves indicate the DWBA calculations by CHUCK3 using the original OM parameters from C. M. Perey and F. G. Perey [32] presented in Table 4.7 (dotted line) and using the adjusted OM parameters of C. M. Perey and F. G. Perey presented in Table 4.8 with the reaction scheme presented in Figure 4.17 the (solid line).

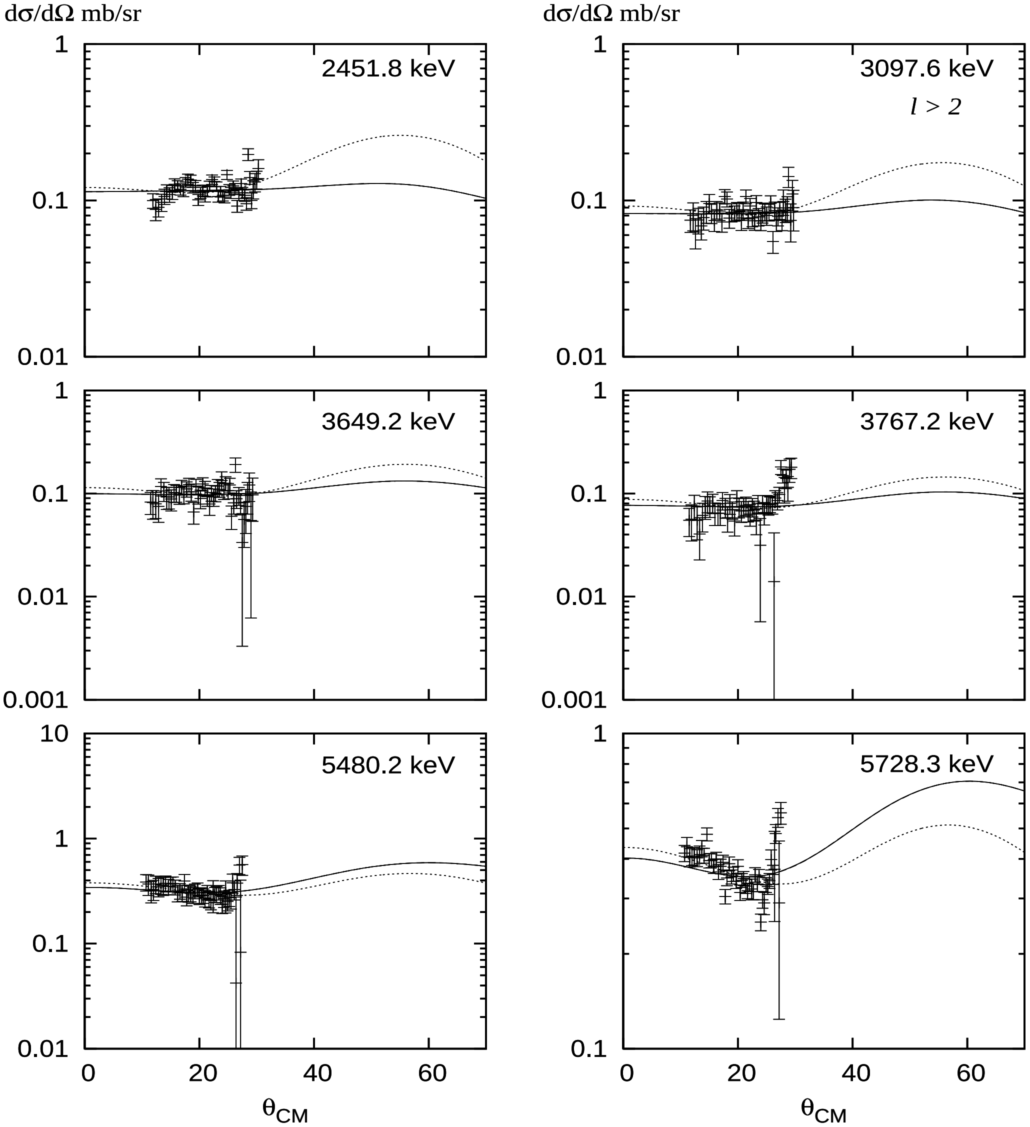

Figure 4.20.: The angular distributions for ^{42}Ar levels from the reaction t(^{40}Ar, p)^{42}Ar, $E^{\mathrm{lab}}_{^{40}\mathrm{Ar}}$= 2.16 A MeV, for $l > 2$ transfer. Curves indicate the DWBA calculations by CHUCK3 using the original OM parameters from C. M. Perey and F. G. Perey [32] presented in Table 4.7 (dotted line) and using the adjusted OM parameters of C. M. Perey and F. G. Perey presented in Table 4.8 with the reaction scheme presented in Figure 4.17 the (solid line).

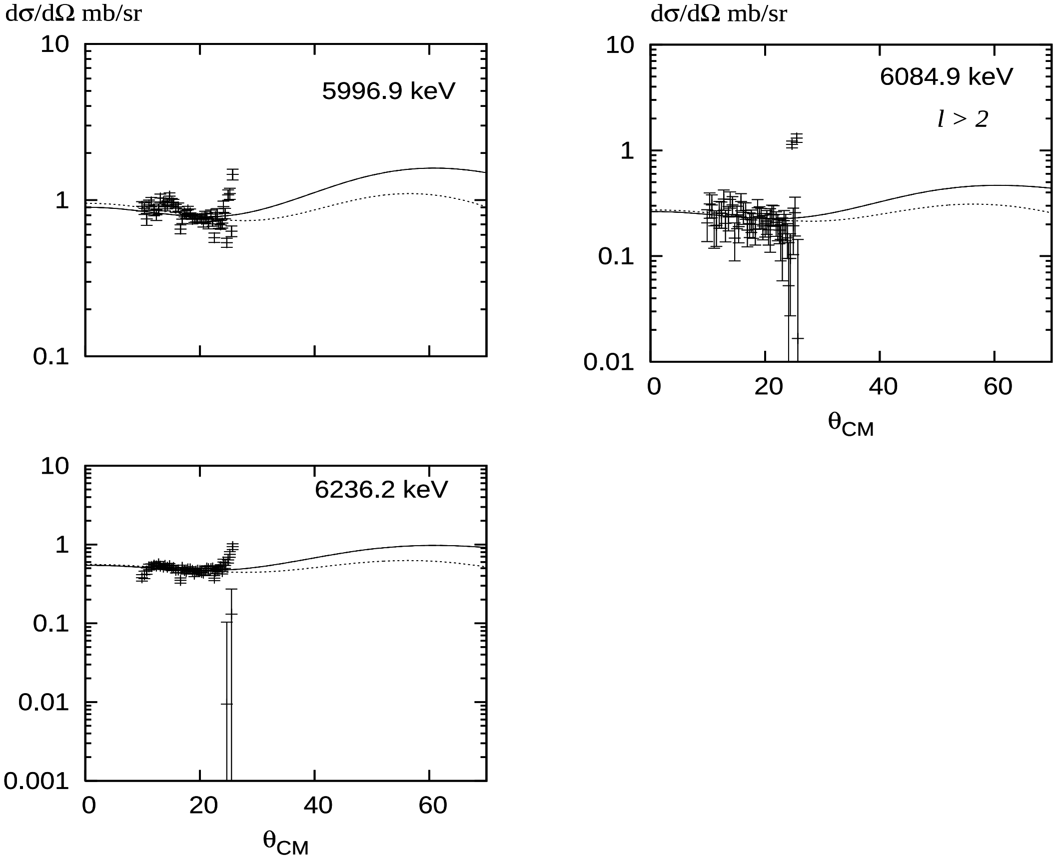

Figure 4.21.: The angular distributions for ^{42}Ar levels from the reaction $t(^{40}Ar,p)^{42}Ar$, $E^{lab}_{^{40}Ar}$= 2.16 A MeV, for $l > 2$ transfer. Curves indicate the DWBA calculations by CHUCK3 using the original OM parameters from C. M. Perey and F. G. Perey [32] presented in Table 4.7 (dotted line) and using the adjusted OM parameters of C. M. Perey and F. G. Perey presented in Table 4.8 with the reaction scheme presented in Figure 4.17 the (solid line).

E_x (keV)	Δl	$E_\mathrm{x}, J^{\pi}_{\mathrm{Ref}[19]}$	$(\frac{d\sigma}{d\Omega})^{\mathrm{max}}_{\mathrm{mb/sr}}$ θ_{max}	A_{Perey}	$A_{\mathrm{Perey_{adj.}}}$	$A^{\mathrm{rel.}}_{\mathrm{Perey_{adj.}}}$	$\varepsilon^{\mathrm{rel.}}_{\mathrm{Flynn.}}$
0.00	0	0.0,0^+	1.44(4) 13.8	3.79	3.66	1.000	1
1198.8(0.7)	2	1208.24(13),2^+	0.70(2) 17.3	3.57	1.83	0.499	0.25
2451.8(0.6)	> 2	2414.0(6),$(3^-, 4^+)$	0.14(1) 29.1	–	–	–	0.025
2961.6(0.8)	2	3013.7(3),$(1, 2^+)$	0.07(2) 28.6	0.26	0.137	0.035	
3097.6(0.9)	4	3096.2(7),4^+	0.10(2) 29.2	1.51	0.59	0.162	0.125
3500.4(1.1)	2	3557.9(3),2^+	0.19(2) 28.1	0.059	0.31	0.085	0.175
3649.2(1.2)	> 2	3705(10), –	0.12(2) 24.6	–	–	–	0.1
3767.2(1.3)	> 2	3820(20), –	0.14(3) 28.7	–	–	–	-
4001.6(1.6)	2	4005.6(6),2^+	0.29(6) 28.2	1.00	0.51	0.139	0.2
4087.9(1.7)	0	4127.5(5),$(0^+, 1, 2)$	0.31(5) 12.2	0.45	1.26	0.344	0.075

Table 4.10.: ^{42}Ar Excitation levels from the reaction t(^{40}Ar,p)^{42}Ar in inverse kinematics at beam energy of $E_{^{40}\mathrm{Ar}}$= 2.16 A MeV.
A_{Perey} is the scaling factor between $(\frac{d\sigma}{d\Omega})_{\mathrm{exp.}}$ and $(\frac{d\sigma}{d\Omega})_{\mathrm{DWBA}}$ obtained with the OM-parameters from Perey & Perey [32], Table 4.7,
$A_{\mathrm{Perey_{adj.}}}$ is the scaling factor obtained with the adjusted set of the OM-parameters, Table 4.8 and considering the coupled channels scheme illustrated in Figure 4.17, with estimated error in A value from 10 to 20%.
$A^{\mathrm{rel.}}$: The normalized to the ground state scaling Factor.
$\varepsilon^{\mathrm{rel.}}_{\mathrm{Flynn.}}$: The normalized to the ground state enhancement factor from E. R. Flynn *et al.* [8] with absolute error of ±15%.

E_x (keV)	Δl	$E_x, J^{\pi}_{\text{Ref}[19]}$	$(\frac{d\sigma}{d\Omega})^{\text{max}}_{\text{mb/sr}}$ θ_{max}	A_{Perey}	$A_{\text{Perey}_{\text{adj.}}}$	$A^{\text{rel.}}_{\text{Perey}_{\text{adj.}}}$	$\varepsilon^{\text{rel.}}_{\text{Flynn.}}$
4258.2(1.9)	2	4287.2(10),(1,2,3)	0.37(5) 28.2	3.08	1.71	0.467	0.25
4399.3(2.2)	2	4405(5),3^-, 4^+	0.44(4) 28.2	3.74	2.17	0.592	0.25
4633.6(2.7)	0	4633.9(6),-	0.39(3) 28.2	0.73	2.08	0.567	0.25
4926.2(3.5)	0	4896(10),-	0.80(5) 11.6	1.05	2.83	0.773	0.2
5057.0(4.0)	0	5000(15),-	1.06(7) 12.0	1.17	2.97	0.812	0.2
5211.6(4.5)	0	5230(15),-	0.38(7) 13.3	0.59	1.50	0.410	
5480.2(5.7)	> 2	-,-	0.37(6) 14.6	–	–	–	–
5728.3(7.0)	> 2	5763(15),-	0.45(4) 27.0	–	–	–	0.25
5996.9(8.6)	> 2	5945(20),-	0.98(5) 13.9	–	–	–	0.5
6084.9(9.2)	> 2	6090(20),-	0.60(9) 24.9	–	–	–	0.2
6236.2(10.3)	> 2	-,-	0.54(4) 12.4	–	–	–	

Table 4.11.: ^{42}Ar Excitation levels from the reaction $t(^{40}Ar,p)^{42}Ar$ in inverse kinematics at beam energy of $E_{^{40}Ar} = 2.16$ A MeV.

A_{Perey} is the scaling factor between $(\frac{d\sigma}{d\Omega})_{\text{exp.}}$ and $(\frac{d\sigma}{d\Omega})_{\text{DWBA}}$ obtained with the OM-parameters from Perey & Perey [32], Table 4.7,

$A_{\text{Perey}_{\text{adj.}}}$ is the scaling factor obtained with the adjusted set of the OM-parameters, Table 4.8 and considering the coupled channels scheme illustrated in Figure 4.17, with estimated error in A value from 10 to 20%.

$A^{\text{rel.}}$: The normalized to the ground state scaling Factor.

$\varepsilon^{\text{rel.}}_{\text{Flynn.}}$: The normalized to the ground state enhancement factor from E. R. Flynn *et al.* [8] with absolute error of ±15%.

4.3.5. Discussion

The low resolution of the proton spectrum does not allow us to be totally sure about states above 3 MeV. Despite of that, some strongly populated states (G.S. 4087.9, 4633.6, 4926.2, 5057 and 5211.6 keV) show angular distributions consistent with $l = 0$. Some other states (1198.8, 2961.6, 3500.4, 4001.6, 4258.2 and 4399.3 keV) show angular distributions consistent with $l = 2$. The rest of the observed states show rather flat and featureless shape for the angular distributions so they were compared arbitrarily to $l = 4$ transfer.

Generally a good agreement between the experimental cross-section and the DWBA calculations was observed only after performing two procedures. First, adjusting the OM parameters for the DWBA calculations. Second, including the inelastic scattering in ^{40}Ar beside the direct two-neutron transfer in the reaction scheme, as illustrated in Figure 4.17, and setting the finite range parameter R = 0 in CHUCK3.

Regarding the first point, Figure 4.22 presents the V_r values used in the DWBA calculations in some previous papers ($*$), compared to the values from Perey & Perey formulas for $\mathrm{E_{beam}} < 20$ MeV (solid line) and $\mathrm{E_{beam}}$ from 30 to 60 MeV (dashed line) which were extracted on the basis of the data points shown. In addition the V_r value used in the current work is shown ($\odot$) for the equivalent beam energy of 6.499 MeV in normal kinematics. From this figure one can observe that we are not the only group who adjusted the OM parameter values to fit the experimental results at low beam energy. For example, in the references: [30] and [10], they increased the V_r value too to fit their results at the low beam energy $\mathrm{E_{beam}} = 9.7$ MeV.

The same discussion is also valid for the volume imaginary potential W for the triton, since it is predicted by the Perey & Perey formula to be 32.86 MeV but reducing it to 27.86 MeV fits better with our lower beam energy data.

Regarding the second point, considering the simple direct one step two-neutron transfer as in E. R. Flynn *et al.* [8] did not produce good results especially for the 0^+ ground state and the 2_1^+ state at 1198.8 (1208.2) keV. Even using different neutron pair configurations instead of the $(1f_{7/2})^2$ configuration did not help. For example, for the 2_1^+ state at 1198.8 (1208.24±13) keV two published papers discussed the configuration of this level within the shell-model, J. Retamosa *et al.* [37] and E. K. Warburton *et al.* [44]. In the first paper a model with valence space of full (sd) region for 4 proton and full (fp) region for 20 neutron is used. In the second paper, a configuration of four nucleons in the (fp) region was considered, which in both cases exceed the code CHUCK3 limitations. In a primary try, we ran DWBA calculations considering a configuration of $(f_{5/2})^2$, $(d_{3/2})^2$, $(p_{3/2})^2$, $(f_{7/2} \otimes f_{5/2})$, $(f_{7/2} \otimes p_{3/2})$, $(f_{7/2} \otimes p_{1/2})$, $(f_{5/2} \otimes p_{3/2})$, $(f_{5/2} \otimes p_{1/2})$, separately, instead of $(f_{7/2})^2$ but this did not improve the angular distribution shape as presented in Figure 4.23. But considering the coupled channels scheme that considers the contribution of two-neutron transfer via 2_1^+ in ^{42}Ar beside the direct transition, illustrated in Figure 4.17 and setting the finite range parameter R = 0 produced a reasonable agreement with the experiment for most of the ^{42}Ar levels, Figures from 4.18 to 4.21.

This result is suprising, since in the normal kinematics experiment at 20 MeV triton beam energy by E. R. Flynn *et al.* [8], good agreement with DWBA calculations was observed for the 2_1^+. One possible explanation may be that two-step processes play a

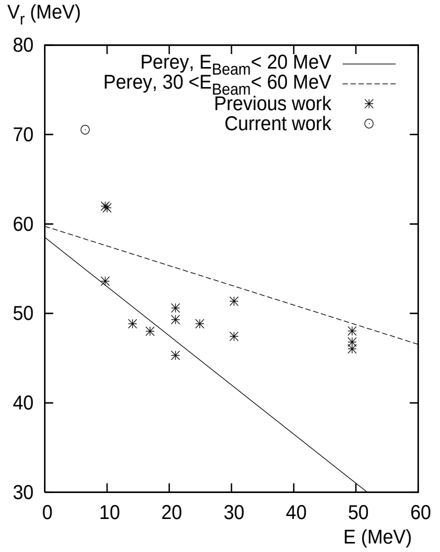

Figure 4.22.: The proton real potential V_r value used in the current work ($\odot$) and in some previous papers with different ^{40}Ar beam energies ($*$) compared to the expected values from Perey & Perey [32] formula for $E_\mathrm{beam} < 20$ MeV (solid line) and $E_\mathrm{beam} <$ from 30 to 60 MeV (dashed line).

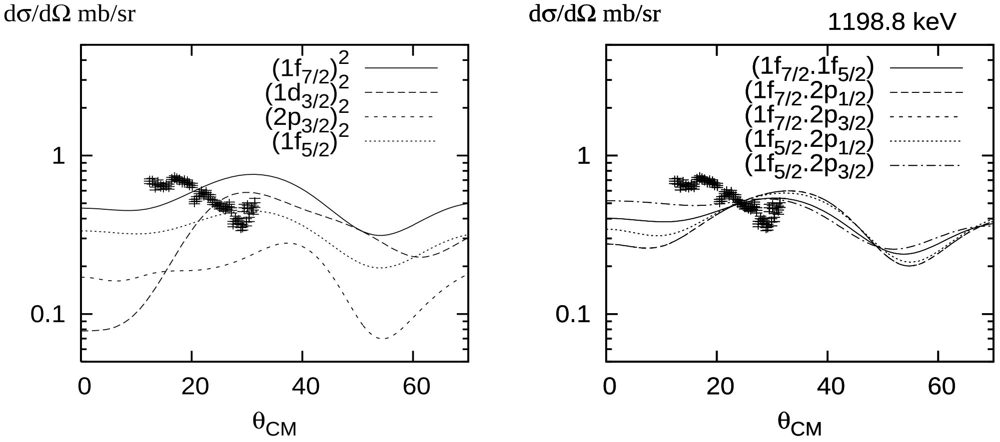

Figure 4.23.: The experimental cross-section angular distribution for 1198.8 keV (1208.24 13 keV) level in ^{42}Ar compared to DWBA, considering $(f_{7/2})^2$, $(f_{5/2})^2$, $(d_{3/2})^2$, $(p_{3/2})^2$ configurations (left), and $(f_{7/2} \otimes f_{5/2})$, $(f_{7/2} \otimes p_{3/2})$, $(f_{7/2} \otimes p_{1/2})$, $(f_{5/2} \otimes p_{3/2})$, $(f_{5/2} \otimes p_{1/2})$ configurations (right), using the adjusted Perey & Perey OM-parameters in Table 4.8.

more important role at lower reaction energy.

In an attempt to compare our results with E. R. Flynn *et al.* [8], since they didn't calculate the spectroscopic factors S explicitly, as we did not too, rather an enhancement factor ε from the equation:

$$(d\sigma/d\Omega)_{\text{exp}} = \varepsilon \; 218 \; \sigma_{\text{DWUCK}} \tag{4.1}$$

Where σ^{DWUCK} is the cross-section calculated by the code DWUCK, with absolute error of ±15%, 218 is the empirical normalization factor for the used code. In the same way a similar quantity is calculated, the scaling factor A, where

$$(d\sigma/d\Omega)_{\text{exp}} = A \; \sigma_{\text{CHUCK3}} \tag{4.2}$$

Both of E. R. Flynn *et al.* enhancement factors ε and our scaling factors A were normalized to their ground state values to produce $\varepsilon^{\text{rel.}}_{\text{Flynn.}}$ and $A^{\text{rel.}}$, respectively. Many of the ^{42}Ar levels observed within this work produced $A^{\text{rel.}}$ similar or in the same order of magnitude to $\varepsilon^{\text{rel.}}_{\text{Flynn.}}$, except for the level 4087.9 keV (4127 keV in ref: [19]), since it is assigned in the current work as $l = 0$ while it is assigned as $l = 0, 1, 2$ in the Nuc. Data. Tab. ref: [19]. Taking into account a wrong assignment for l can dramatically change the calculated σ_{CHUCK3} value.

Chapter 5

Summary and Discussion

The two aims of this thesis were performed successfully. First aim, testing the strength of the N = 28 shell closure in the *fp*-shell region was performed by studying the $^{54}\mathrm{Fe}(\vec{\mathrm{d}},\mathrm{p})^{55}\mathrm{Fe}$ reaction in normal kinematics. The discussion presented in Section 3.1.6 and Figure 3.17 gave us a strong evidence about the cross shell excitation in the $^{54}_{26}\mathrm{Fe}_{28}$ ground state wave function and the existence of particle-hole configuration for a part of it, where 8 levels with $J^{\pi} = \frac{7}{2}^{-}$ were observed experimentally, three of them are the well known levels 1316, 1408, 2938 keV. In particular the lowest $\frac{7}{2}^{-}$ level should not be populated if the ^{54}Fe ground state wave function has a well closed $1f_{7/2}$ shell for the neutrons. Also the weakness of N = 28 in Fe was deduced by comparing the experimental results with a large scale shell model calculation by A. Lisetskiy using the ANTOINE code [5] and the GXPF1 effective interaction from T. Otsuka *et al.* [17]. In these calculations the full *fp*-shell region, including the $1f_{7/2}$ shell, was included and up to 6 particle-hole excitations across the N = 28 gap were allowed. The results of these calculations show very good agreement with the experiment up to about 2.5 MeV excitation energy. The instability of the $1f_{7/2}$ shell deduced in this work is consistent with the theoretical calculations performed by M. Honma, T. Otsuka *et al.* [17].

Beside that, care was taken to identify levels belonging to ^{57}Fe and falsely identified as ^{55}Fe in previous work caused by the companion reactions $^{56}\mathrm{Fe}(\vec{\mathrm{d}},\mathrm{p})^{57}\mathrm{Fe}$ or $^{58}\mathrm{Fe}(\vec{\mathrm{d}},\mathrm{t})^{57}\mathrm{Fe}$ due to target contamination. The levels at 2015, 3285, 3860(10), 4123(10) and 4372(10) keV that were determined previously as ^{55}Fe levels, are rather the ^{57}Fe levels 367, 1627, 2220, 2456 and 2758 keV, respectively, Figures 3.2 & 3.3. All the published work observing those levels have considerable target contaminations and no work has been done with γ-spectroscopy.

Performing the two-neutron transfer reactions $^{58}\mathrm{Ni}(\vec{\mathrm{p}},\mathrm{t})^{56}\mathrm{Ni}$ provided us with two evidences about the limited strength of the N = 28 shell closure. First, considering $1f_{7/2}$ in Ni as a broken shell by including it in the DWBA calculations improved the agreement between measured and calculated angular distributions and asymmetries significantly, Figure 4.10. Second, using a combination of simultaneous and sequential two-neutron transfer with different ratios described the experimental results better than using one type separately, which indicates the presence of paring correlations due to the limited purity of the closed $1f_{7/2}$ shell in the ground state wave function.

Our experimental results for the $^{54}\mathrm{Fe}(\vec{\mathrm{d}},\mathrm{p})^{55}\mathrm{Fe}$ reaction are in a good agreement with those from T. Taylor and J. A. Cameron [41] and D. C. Kocher [19], and the results from J. H. Polane *et al.* [34] for the reaction $^{58}\mathrm{Ni}(\vec{\mathrm{p}},\mathrm{t})^{56}\mathrm{Ni}$ who studied the reaction in the same conditions but only for the ^{56}Ni ground state.

The second aim of this thesis, which is testing the potential of inverse kinematics reactions, was performed in Section 3.2 by studying the single-neutron transfer reaction $\mathrm{d}(^{54}\mathrm{Fe},\mathrm{p})^{55}\mathrm{Fe}$ in inverse kinematics and comparing the results with those obtained in normal kinematics.

In spite of the low resolution and the low reaction cross-section, three levels with $J^{\pi} = \frac{7}{2}^{-}$ were observed at 1314, 1408 and 2938.8 keV. The observation of those levels beside the general agreement in the $S^{\mathrm{rel.}}_{\mathrm{Aver.}}$ obtained in normal and inverse kinematics, satisfy the second aim of this thesis paving the way to extend our study to nuclei far off stability. Table: 5.1 and Figure 5.1 show a comparison between the results obtained from normal and inverse kinematic for some of the observed ^{55}Fe levels.

E_{x} (keV)	Δl	J^{π}	$E_{\mathrm{x}}, J^{\pi}_{\mathrm{Ref}[19]}$	$S^{\mathrm{rel.(Inverse)}}_{\mathrm{Aver.}}$	$S^{\mathrm{rel.(Normal)}}_{\mathrm{Aver.}}$
0.0	1	$\frac{3}{2}^{-}$	0.0,$\frac{3}{2}^{-}$	1.000	1.000
411.05(0.13)	1	$\frac{1}{2}^{-}$	411.42(21),$\frac{1}{2}^{-}$	0.68(1)	0.72(1)
931.41(0.12)	3	$\frac{5}{2}^{-}$	931.29(13),$\frac{5}{2}^{-}$	0.9(3)	0.87(2)
1316.54(0.12)	3	$\frac{7}{2}^{-}$	1316.54(13),$\frac{7}{2}^{-}$	0.25(2)	0.057(1)
1408.21(0.13)	3	$\frac{7}{2}^{-}$	1408.45(14),$\frac{7}{2}^{-}$	0.21(1)	0.025(1)

Table 5.1.: Table showing ^{55}Fe levels excitation energies, transferred angular momentum Δl, total angular momentum J^{π} from the $^{54}\mathrm{Fe}(\vec{\mathrm{d}},\mathrm{p})^{55}\mathrm{Fe}$ reaction studied in this work, E_{x} excitation energies and J^{π} from nuclear data sheets, maximum cross-section and its position, normalized spectroscopic factors $S^{\mathrm{rel.(Inverse)}}_{\mathrm{Aver.}}$ and $S^{\mathrm{rel.(Normal)}}_{\mathrm{Aver.}}$ obtained from inverse and normal kinematics, respectively.

The difference between $S^{\mathrm{rel.(Inverse)}}_{\mathrm{Aver.}}$ and $S^{\mathrm{rel.(Normal)}}_{\mathrm{Aver.}}$ for some of the ^{55}Fe levels is mainly resulting from the overlap between the levels due to the low resolution (FWHM $\simeq$ 150 keV) in the $\mathrm{d}(^{54}\mathrm{Fe},\mathrm{p})^{55}\mathrm{Fe}$ reaction, as discussed previously in Section 3.2.5. The general little difference in $S^{\mathrm{rel}}_{\mathrm{Aver.}}$ obtained from the two kinematics, or more clearly between $S^{\mathrm{rel.(Inverse)}}_{\mathrm{Aver.}}$ obtained with low beam energy $\mathrm{E}_{\mathrm{Beam}} \simeq$ 2.5 AMeV and $S^{\mathrm{rel.(Normal)}}_{\mathrm{Aver.}}$ obtained with intermediate beam energy $\mathrm{E}_{\mathrm{Beam}} \simeq$ 7 AMeV raise a question about the reliability of the used OM parameters at low beam energy. This question arises again after performing the $\mathrm{t}(^{40}\mathrm{Ar},\mathrm{p})^{42}\mathrm{Ar}$ reaction at a similar low beam energy.

The capability of inverse kinematic reactions was confirmed by performing the two-neutron transfer reaction $\mathrm{t}(^{40}\mathrm{Ar},\mathrm{p})^{42}\mathrm{Ar}$ using a beam of ^{40}Ar at $\mathrm{E}^{\mathrm{lab}} = 2.16$ AMeV and comparing the results with those obtained in normal kinematics by E. R. Flynn *et al.* [8], where they performed the reaction at a higher triton beam energy, $\mathrm{E}^{\mathrm{lab}}$ = 20 MeV. Table: 5.2 shows a comparison between their enhancement factors $\varepsilon^{\mathrm{rel.}}_{\mathrm{Flynn.}}$

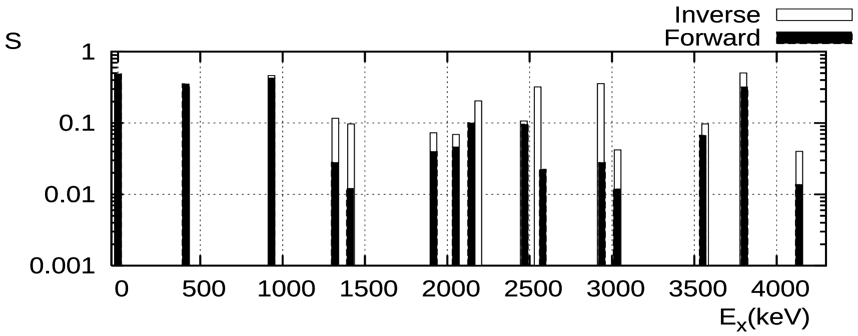

Figure 5.1.: Comparison between the spectroscopic factors $S_{\mathrm{Aver.}}$ for ^{55}Fe levels deduced from the forward and the inverse kinematics. Spectroscopic factors for strong transitions agree reasonably well (for example: ground state, 411, 391 keV). Some weakly populated states show large deviations in the spec. fact. (for example: 1316, 1408 keV) due to the limited energy resolution in the inverse kinematics reaction, weakly populated states are not always resolved.

normalized to the ground state and our normalized scaling factor $A^{\mathrm{rel.}}_{\mathrm{Perey_{adj.}}}$ obtained from the adjusted set of OM parameters from Perey and Perey [32] for some of the observed ^{42}Ar levels. We can see some agreement between $A^{\mathrm{rel.}}_{\mathrm{Perey_{adj.}}}$ and $\varepsilon^{\mathrm{rel.}}_{\mathrm{Flynn.}}$ for the strong levels.

E_{x} (keV)	Δl	E_{x}, $J^{\pi}_{\mathrm{Nuc.Dat.}}$ (keV)	$A^{\mathrm{rel.}}_{\mathrm{Perey_{adj.}}}$	$\varepsilon^{\mathrm{rel.}}_{\mathrm{Flynn.}}$
0.00	0	0.0,0^+	1.000(7)	1
1198.8(0.7)	2	1208.24(13),2^+	0.499(3)	0.25
3097.6(0.9)	4	3096.2(7),4^+	0.162(3)	0.125
3500.4(1.1)	2	3557.9(3),2^+	0.085(1)	0.175
4001.6(1.6)	2	4005.6(6),2^+	0.139(3)	0.2
4258.2(1.9)	2	4287.2(10),(1,2,3)	0.467(7)	0.25

Table 5.2.: A comparison for the t(^{40}Ar, p)^{42}Ar experiment between our scaling factor $A^{\mathrm{rel.}}_{\mathrm{Perey_{adj.}}}$ normalized to the ground state obtained from the adjusted set of OM parameters from Perey and Perey [32] and E. R. Flynn *et al.* [8] normalized enhancement factors $\varepsilon^{\mathrm{rel.}}_{\mathrm{Flynn.}}$ for some of the observed ^{42}Ar levels.

Unfortunately, in this reaction we were forced to consider a simple scheme for the two-neutron transition, since no data were published presenting spectroscopic amplitudes for multi-step processes. However, one can observe reasonable agreement between our results and those from E. R. Flynn *et al.*, keeping in mind the 15% uncertainities in their results and our low resolution (FWHM $\simeq$ 200 keV.), the limited availability of theoretical calculations and spectroscopic amplitudes for the multi-step process.

Anyhow the sufficient reliability of inverse kinematics was shown once by performing the single-neutron transfer reaction d(^{54}Fe, p)^{55}Fe, where the deduced transferred angular momentum and spectroscopic factors for strong levels with $E_{\mathrm{Beam}} \sim 2$ AMeV agree well with those from normal kinematics, Table 5.1. The possibility to search for 0^+ states with (t,p) reactions in inverse kinematics was proven also by performing the two-nucleon transfer reaction $\mathrm{t}(^{40}\mathrm{Ar},\mathrm{p})^{42}\mathrm{Ar}$, Table 5.2, where it has been established as a tool to deduce the transferred angular momentum values and for future studies of pair transfer and the search for 0^+ states in exotic nuclei.

One of the problems we had in this work is the limitation of the code CHUCK3 with respect to the number of channels and couplings. For the $^{58}\mathrm{Ni}(\vec{\mathrm{p}},\mathrm{t})^{56}\mathrm{Ni}$ reaction we were forced to ignore some couplings and use the models presented in Figure 4.9. Also we suffer from a lack of theoretical spectroscopic amplitudes for sequential and simultaneous two-neutron transfer, especially for excited levels.
Another problem we had is the lack of systematic studies of OM- parameters at low beam energies. Such parameters could be deduced by fitting elastic-scattering angular distributions for various incident particles as in C. M. Perey and F. G. Perey [32].
Also to perform the inverse kinematic reactions at higher beam energy we need to suppress the fusion on the target holding material (Ti and C), which are taken into account in the plans for a heavy ion spectrometer at HIE-ISOLDE.

Finally, for inverse kinematics transfer reactions the combination of particle detection with high resolution γ-ray spectroscopy is needed beside a wide range coverage for the angular distribution. These requirements will be available at the REX-ISOLDE MiniBall setup at CERN using a newly developed 4π particle detector system [4]. As a results of the study performed within this thesis a first (t,p) experiment $\mathrm{t}(^{30}\mathrm{Mg},\mathrm{p})^{32}\mathrm{Mg}$ has been accepted by the CERN INTC and will possibly be performed late in 2008.

Appendix: Optical-Model Parameters

The '*standard form*' given by C. M. Perey and F. G. Perey [32] (see Section 1.3) defined as

$$\begin{aligned} U(r) &= V_{\text{coul}} - Vf(x_r) + \left(\frac{h}{m_\pi c}\right)^2 V_{so}(\sigma \cdot l)\frac{1}{r}\frac{d}{dr}f(x_{so}) \\ &- i[Wf(x_W) - 4W_D\frac{d}{dx_D}f(x_D)] \end{aligned}$$

Neutrons parameters

Neutrons potential is based on Beccetti and Greenlees analysis [2] and applicable to A > 40 and E up to 24 MeV. Their best average neutron parameters sets are, where potentials in MeV, r and a in fermis:

$V = 56.3 - 0.32E - 24(N - Z)/A$
$r_o = 1.17,\ a_o = 0.75$
$W = 0.22E - 1.56$, or zero, whichever is greater
$W_D = 13 - 0.25E - 12(N - Z)/A$, or zero whichever is greater
$r_W =\ r_D = 1.26,\ a_W =\ a_D = 0.58$
$V_{so} = 6.2,\ r_{so} = 1.01,\ a_{so} = 0.75$

At lower energy, where Becchetti-Greenlees potential may not be satisfactory, the Wilmore and Hodgson potential was used

$V = 47.01 - 0.267E - 0.0018E^2$
$r_o = 1.322 - 7.6A \times 10^{-4} + 4A^2 \times 10^{-6} - 8A^3 \times 10^{-9}$
$a_o = 0.66$

$W_D = 9.52 - 0.053E$
$r_D = 1.266 - 3.7A \times 10^{-4} + 2A^2 \times 10^{-6} - 4A^3 \times 10^{-9}$
$a_D = 0.48$

Protons parameters

The systematic analysis of Becchetti and Greenlees [2] fitted well a large number of elastic differential cross sections and polarization data for A > 40 and E < 50 MeV.

$V = 54.0 - 0.32E + 24(N - Z)/A + 0.4(Z/A^{1/3})$
$r_o = 1.17.a_o = 0.75$
$W = 0.22E - 2.7$, or zero, whichever is greater
$W_D = 11.8 - 0.25E + 12(N - Z)/A$, or zero, whichever is greater
$r_W = r_D = 1.32,\ a_W = \ a_o = 0.51 + 0.7(N - Z)/A$
$V_{so} = 6.2,\ r_{so} = 1.01,\ a_{so} = 0.75$

from 30 to 60 MeV

$V = 49.9 - 0.22E + 26.4(N - Z)/A + 0.4(Z/A^{1/3})$
$r_o = 1.16, a_o = 0.75$
$W = 1.2 + 0.09E$
$W_D = 4.2 - 0.05E + 15.5(N - Z)/A$
$r_W = \ r_D = 1.37,\ a_W = \ a_D = 0.74 - 0.008E + 1.0(N - Z)/A$
$V_{so} = 6.04,\ r_{so} = 1.064,\ a_{so} = 0.78$
$r_c = 1.25$

at lower energies below 20 MeV

$V = 53.3 - 0.55E + 27(N - Z)/A + 0.4(Z/A^{1/3})$
$r_o = 1.25,\ a_o = 0.65$
$W_D = 13.5 \pm 2.0$
$r_D = 1.25,\ a_D = 0.47$
$V_{so} = 7.5,\ r_{so} = 1.25,\ a_{so} = 0.47$
$r_c = 1.25$

Deuterons parameters

The deduced parameters for A > 40 are:

$V = 91.13 + 2.2(Z/A^{1/3})$
$r_o = 1.05,\ a_o = 0.86$
$W_D = 218/A^{2/3}$
$r_W = 1.43,\ a_W = 0.50 + 0.013A^{2/3}$
$V_{so} = 7.0,\ r_{so} = 0.75,\ a_{so} = 0.5$
$r_c = 1.3$

below 12 MeV

$V = 81.0 - 0.22E + 2.0(Z/A^{1/3})$
$r_o = 1.15,\ a, = 0.81$
$W_D = 14.4 + 0.24E$
$r_D = 1.34,\ a, = 0.68$
$r_c = 1.15$

Tritons parameters

$V = 165.0 - 0.17E - 6.4(N - Z)/A$
$r_o = 1.20,\ a_o = 0.72$
$W = 46.0 - 0.33E - 110(N - Z)/A$
$r_W = 1.40,\ a_W = 0.84$
$V_{so} = 2.5,\ r_{so} = 1.20,\ a_{so} = 0.72$
$r_c = 1.30$

Bibliography

[1] W. Awssmann *et al.*, Nuc. Inst. Meth. 122 (1974) 191.

[2] Jr. F. D. Becchetti and G. W. Greenlees, Phys. Rev. 182(1969) 1190

[3] C. A. Bertulani and P. Danielewicz, Introduction to Nuclear Reactions (Institute of Physics Publishing 2003)

[4] Vinzenz Bildstein, Ongoing Ph.D. dissertation, TU-München.

[5] E. Caurier and F. Nowacki, Acta Phys. Pol. B 30, 705 (1999).

[6] Herman Feshbach, Theoretical Nuclear Physics (Wiley, New York u.a. 1992).

[7] H. J. Feschbeck *et al.*, Phys. Rev. 150 (1966) 941.

[8] E. R. Flynn *et al.*, Nuc. Phy. A 246 (1975) 117.

[9] H. A. Enge and S. B. Kowalski, Proc. Intern. Conf. Magnet technology, (Hamburg, 1970) p. 727.

[10] A. E. Glassgold *et al.*, Phys. Rev. 106, 1207 (1957)

[11] N. K. Glendenning, Ann. Rev. Nucl. Sci. (palo Alto) 13(1963) 191.

[12] N. K. Glendenning, Direct Nuclear Reaction (World Scientific, 1983)

[13] P. J. Van Hall *et al.*, Nucl. Phys. A291 (1977) 63.

[14] R. Hertenberger *et al.*, Rev. Scie. Inst. **69,2**, (1998) 750.

[15] R. Hertenberger *et al.*, Nuc. Instr. and Meth. A536 (2005) 266.

[16] J. Homolke, Kine program, E12 Physics Department, TU-München.

[17] M. Honma, T. Otsuka *et al.*, Phys. Rev. C69 (2004) 034335

[18] Huo Junde, Nuclear Data Sheets 64 (1991) 723.

[19] D. C. Kocher, Nucl. Data Sheets 18 (1976) 463

[20] J. Kopecky, K. Abrahams and F. Stecher-Rasmuss, Nuc. Phys. A188, Issue 3 (1972) 535.

[21] Kenneth S. Krane, Introductory Nuclear Physics (John Wiley & Sons, New York u.a. 1988).

[22] G. Kraus *et al.*, Phys. Scr. T56 (1995) 114.

[23] P. D. Kunz, CHUCK- A Coupled-Channel Code, The Niels Bohr Institute Computer Program Library. Copenhagen (1977).

[24] P. D. Kunz, DWUCK- A Coupled-Channel Code, The Niels Bohr Institute Computer Program Library. Copenhagen.

[25] W. R. Leo, Techniques for Nuclear and Particle Physics Experiments (Springer-Verlag, Berlin 1994).

[26] R. Lutter *et al.*, MARaBOU MBS and Root Based Online Ofline Utility, Maier-Leibnitz-Laboratorium Munich.

[27] M. Löffler *et al.*, Nuc. Inst. Meth, III (1972) 1-12.

[28] Macfarlane *et al.*, Phys. Rev. 127, (1962) 204.

[29] M. H. Macfarlane and J. B. French Rev. Mod. Phys. 32 (1960) 567.

[30] J. S. Nodvik and D.S. Saxon, Phys. Rev.117, 1539 (1960)

[31] E. B. Paul, Nuclear and Particle Physics (North-Holland publishing company 1969).

[32] C. M. Perey and F. G. Perey, Atom. Data and Nuc. Data. Tables 17 (1976) 1.

[33] J. H. Polane *et al.*, J. Phys. G: Nucl. Part. Phys 15 (1989) 1715-1733.

[34] J. H. Polane *et al.*, J. Phys. G: Nucl. Part. Phys 15 (1989) 1749-1768.

[35] J. H. Polane *et al.*, J. Phys. G: Nucl. Part. Phys.15 (1989) 1735

[36] S. Raman *et al.*, Atom. Data and Nuc. Data. Tables 78 (2001) 1.

[37] J. Retamosa *et al.*, Phys. Rev. C55, 1266 (1997)

[38] F. Riess, Gaspan program, Sektion Physik, Ludwig-Maximilians-Universität München.

[39] G. R. Satchler, Phys. Rev. C 4 (1971) 1485

[40] A. Sperduto and W. W. Buechner, Phys. Rev. 134 (1964) B142.

[41] T. Taylor and J. A. Cameron, Nuc. Phy. A337 (1980) 389

[42] I. J. Thompson, FRESCO- A Coupled-Channel program, Comp. Phy. Rep. 7, (1988) 167 .

[43] R. J. Van de Graaff, Nuc. Inst. Meth 8 (1960) 195.

[44] E. K. Warburton *et al.*, Phys. Rev. C44, 268 (1991)

[45] C. A. Wiedner *et al.*, Nuc. Inst. Meth, 105, 205(1972).

[46] H. F. Wirth, Ph.D. thesis, TU München, 2001.

List of Figures

List of Tables

Acknowledgment

It is easy to say thank you, but it's harder
to convey the deep and heartfelt gratitude I feel.

By the end of this thesis
I would like to thank the teacher
who I couldn't do this work without his help.
Prof. Dr. Reiner Krücken
for his excellent friendly guiding, care and support during this study
and
Dr. Thomas Faestermann
for his valuable help and his answers for all questions about the Q3D.

Also I would like to thank Dr. Roman Gernhäuser, Dr. Josef Homolka, Dr. Jürgen Friese and Dr. Thorsten Kröll for the useful discussions.

I can't forget my family, my friends for their support and love, my group E12, and the best colleagues I ever had Ralf Lang, Sigrid Weichs and her family, Petra Zweckinger, Michael Klöckner, Maria-Katharina Nacke, Wolfgang Heimkes and Michael Böhmer who gave me the hope and the strength.

Finally, I would like to thank the TU-München and DFG
for supporting this work.


Noha
Paul
Sagdah
Wafa
Hind
Magdy
Rabab
Thomas
Amany
Nagoah
Norah
Nagla
Abdeen
Asma
Mamdoh
Magdalena
Fayz
Sohaad
Amer
Kamel
Rasha
Mohamed Ali
Tarik
Christoph
Fatima
Reiner
Waleed
El−helly
Hamadah
Martin
Mohamed
Hany
ElSaida
ElAgab
Anja
Mahassen
Nada
Jon Billowes
Yomna
David
Mahgoub
Khaled
Jehan
Hanan
Hafiz
Alaa
Okasha
Mohamed Mahgoub
Ken
Martina
Ismail
Tawfeq
Ashaa
Amro
Ayad
Petra
Roman
Faysal
Esam
Gavin
Haitham
sigrid
Husham
Josef
Amal
Liene
Yahya
Ahmed
Felix
Abo Yasser
Hasaan
Frdos
Nazih
Olga
Rudii
Kathi
Khaldah
Ralf
Omar
Elmoaz
Magdy
Andy
Hassan
Alyaa
Porhan
Amira
Abdo
Abdelaziz
Osama
Michael
Abo Sareaa
OmSlmah
Jürgen
Osman
Sven
Mahmoud
Inas
Abdalah
Flo
Kawarth
Mustaffah
Elsadig
Lobna
Richard
Ayman
Iman
Amna
Aaron
Moataz
Sawah
Ehab
Mubarak
Awad
Babiker
Talal
Adel
Ali
abaker
Elamien
Abeer
Morsy

Thanks ...